UNIVERSITY OF SOUTHAMPTON

FACULTY OF PHYSICAL SCIENCES AND ENGINEERING

Physics and Astronomy

Fabrication and characterization of hybrid liquid crystal devices

by

Matthew Proctor

Thesis for the degree of Doctor of Philosophy

November 2015

UNIVERSITY OF SOUTHAMPTON

ABSTRACT

FACULTY OF PHYSICAL SCIENCES AND ENGINEERING

Physics and Astronomy

Doctor of Philosophy

FABRICATION AND CHARACTERIZATION OF HYBRID LIQUID CRYSTAL DEVICES

by Matthew Proctor

This thesis describes new characterization techniques that can be used to investigate nematic liquid crystal (LC) materials and systems, and experimental studies of new hybrid LC devices.

The characterization techniques include an all-optical method for determining nematic viscosities, a multi-spectrum analysis (VTF) of the electro-optic response of an LC device subject to an AC field, and a measurement of two-beam coupling (TBC) in photorefractive LC systems subject to an AC field. The time response measurement is the first experimental study of fast director oscillations seen when a modulated field is applied to a cell, and it has been shown that Erickson-Leslie theory can be used to determine the rotational viscosity by fitting to these oscillations. The VTF has been used to show that the conductivity of the LC E7 is 2 $\times$ that of TL205, and can explain the origin of higher beam coupling in E7 photorefractive devices. The AC driven TBC and its analysis has proved that a non-ohmic photoconductor will lead to two distinct beam coupling regimes in frequency space, and has shown that optimum beam coupling efficiency can be obtained by tuning the AC frequency.

The range of new hybrid LC devices investigated here include cells using an LC doped with multiferroic nanoparticles, and photorefractive cells that use a new electrode material (PEDOT) to reduce injection barriers in standard photorefractive devices, a photorefractive polymer (JTDA16) as an aligning layer, and a photoaligning layer (PAAD) to enhance the modulation depth of induced photorefractive gratings. The multiferroic nanoparticle study showed that a magneto-optic response could be observed at low fields (< 500 Gauss), and that the sol-gel process for growing nanoparticles is not appropriate for creating ferroelectric layers with thicknesses below ~ 15 nm. The new materials for photorefractive cells have shown promising results, with observed diffraction efficiencies up to 13 $\times$ higher than a benchmark cell using polyvinyl carbazole as a photoconductor.

Contents

List of Figures

List of Tables

Declaration of Authorship

I, Matthew Proctor, declare that the thesis entitled *Fabrication and characterization of hybrid liquid crystal devices* and the work presented in the thesis are both my own, and have been generated by me as the result of my own original research. I confirm that:

- this work was done wholly or mainly while in candidature for a research degree at this University;
- where any part of this thesis has previously been submitted for a degree or any other qualification at this University or any other institution, this has been clearly stated;
- where I have consulted the published work of others, this is always clearly attributed;
- where I have quoted from the work of others, the source is always given. With the exception of such quotations, this thesis is entirely my own work;
- I have acknowledged all main sources of help;
- where the thesis is based on work done by myself jointly with others, I have made clear exactly what was done by others and what I have contributed myself;
- parts of this work have been published as: [1] and [2]

Signed:.....

Date:.....

Acknowledgements

This work would not have been possible without the support from a number of people: too many to include in full here. I would like to thank my two supervisors, Malgosia Kaczmarek and Giampaolo D'Alessandro for their encouragement, teaching, and patience throughout my PhD. The other giants on whose shoulders I have been standing include Olexander Buchnev, Nina Podoliak, Keith Daly, James Bateman, and Mark Herrington. I have particularly enjoyed working with and learning from my colleagues and friends Elena Mavrona, Tom Bennett, Thomas Regrettier, and particularly Andrew Acreman, who has always made himself available to interesting discussions regarding my work.

There is no way I could have completed this work without the love and encouragement from my wonderful friends and family, especially my Mum and Dad and my sister. They have been there through every step that has led up to this PhD, and I count myself blessed for having them with me on that journey.

Finally, thank you to my wife Becky and my baby daughter Amelie. All of this was done for you.

Chapter 1

Introduction

> "Wisdom comes from experience. Experience is often a result of lack of wisdom."
>
> Terry Pratchett

All matter tends to be categorised into three distinct phases: solids, liquids and gases, but this is only true up to a point. The existence of exotic states that do not fit in to these convenient boxes, such as high temperature plasmas found in hydrogen fusion experiments, and low temperature Bose-Einstein condensates that seem to obey a totally new set of physical laws, show that the three-phase picture is incomplete.

The liquid crystal (LC) state is a phase of matter that shares characteristics with both liquids and crystalline solids. LCs are used extensively as optical switches in displays, although organic light emitting diode (OLED) technology is starting to take the place of LC displays [3]. Fortunately, LCs find application well beyond the eponymous displays; applications such as: variable focus lenses [4, 5], tunable photonic crystals [6], protective eye-wear [7], spatial light modulators [8] and soliton generation [9] to name but a few.

This thesis describes investigations into hybrid LC devices, wherein one or more components of a planar LC cell (see section 1.3) are modified in order to increase efficiency or to add another level of functionality. More specifically, LC materials have been doped

with multiferroic nanoparticles in order to decrease the magnitude of addressing magnetic and electric fields, as described in chapter 5, and photorefractive devices that use a photoconductive polymer in contact with the LC layer have been fabricated, and the strength of the photorefractive response characterized, as described in chapters 4 and 6. Furthermore, novel characterization techniques have been developed that can be used to measure useful variables: the LC time constant as described in chapter 3, or the relative voltage drop across the constituent layers in a cell as described in chapter 4.

This introductory chapter describes nematic LCs with particular reference to how they respond to applied electrical, magnetic and optical fields. Typical aligned geometries are discussed with emphasis on so-called planar cells, along with the aligning force applied by treated polymer films. The process of fabricating LC devices is then explained, followed by the response of these devices to applied electric or magnetic fields. Finally, the optical properties of these devices is examined, all of which explains the useful electro-optic properties of LC based technologies.

1.1 Categorizing thermotropic liquid crystals

Broadly speaking, all LC materials can be placed into one of two categories: those that can be realized by controlling temperature, and those that can be realized by dissolving material in a solvent; these categories are known as thermotropics and lyotropics respectively. Lyotropic LCs will not feature in this thesis, but relevant information can be found in the last chapter from reference [10].

The very first identification of an LC phase (although not the first use - see [11]) was due to Reinitzer in 1888 [12]. He observed that one can achieve two liquid states when heating up a sample of a cholesterol derivative, one cloudy and one clear. We now know that the cloudy state is a liquid crystalline mesophase, lying in the temperature range between a crystalline solid and an isotropic liquid, the molecular organization of which is depicted in figure 1.1.

The rod shaped molecules depicted in figure 1.1 are mobile, meaning that the bulk material retains many of the properties of an isotropic liquid. Nevertheless there is some

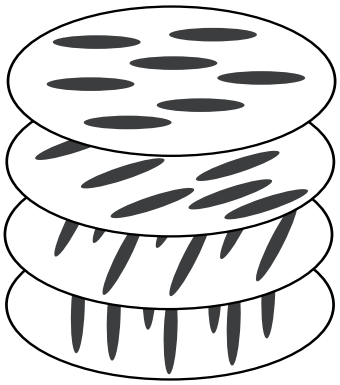

Figure 1.1: Cholesteric liquid crystal

intrinsic ordering, a crystalline property that has earned these materials the moniker "liquid crystal". Since Reinitzer's discovery, there has been considerable work identifying, categorizing and investigating the response of these materials to applied fields, work that has yielded the familiar display technologies widely used to this day.

The cholesteric phase is only one of a number of mesophases that exist in a liquid crystalline state. These mesophases all share liquid and crystalline properties, and are categorised according to the ordering. Some common examples are shown in figure 1.2.

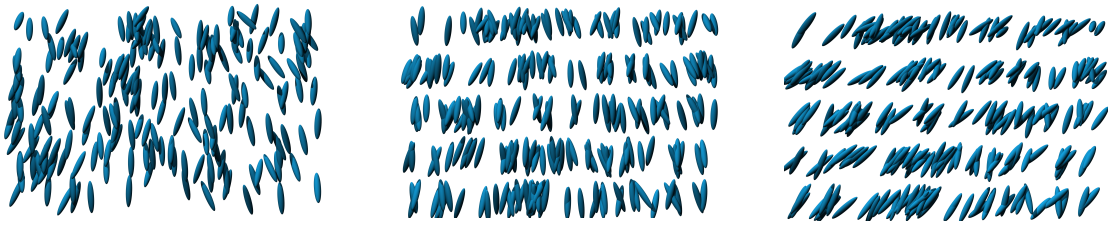

Figure 1.2: Common thermotropic mesophases. From left to right: nematic, smectic A, and smectic C. In the nematic phase, the molecular position is random, but the average alignment of the molecules is non-zero. The molecules in smectic phases also have a non-zero average alignment, and are in addition positioned in layers, with the average director parallel and tilted with respect to the normal of the layer for the smectic A and C phase respectively.

This thesis is mainly concerned with nematic materials the ordering of which can be seen in the left-hand panel of figure 1.2. Nematics tend to consist of "rod-shaped" molecules, which preferentially align parallel to the neighbouring molecules due to intermolecular forces, and have a random position within the bulk. The result is a liquid material, with some non-zero average molecular orientation.

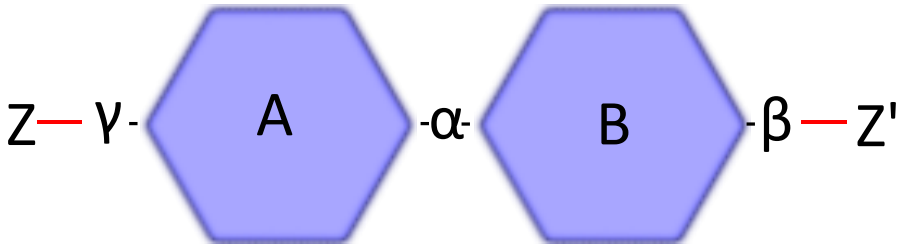

Figure 1.3: Generalised structure of nematics - the groups denoted by Greek letters are not necessary for calamitic LCs.

1.1.1 Chemical properties of calamitic nematics

The molecular structure of nematic LC molecules is responsible for the parameters that make the materials useful in electro-optic devices, namely long-range ordering, birefringence, dielectric anisotropy, and low optical absorption. This section outlines a general molecular structure for an LC material, and then goes on to discuss why this structure results in molecular alignment and anisotropic polarizability.

The common term "mesogenic" - resulting in a mesophase - is used to describe the compounds that exhibit LC phases. These mesogenic compounds can also exhibit smectic phases, examples of which are shown in figure 1.2, either in addition to or instead of the nematic phase. Furthermore, mesogens are not restricted to the rod-like "calamitics" mentioned earlier, and can include disk-shaped "discotic" mesogens [13]. The discussion will not extend to smectic LCs as they have not had the same technological impact nematics have, but the same chemical template from figure 1.3 can be used in either case.

The following discussion will reference the labels in figure 1.3. A and B constitute the core of the molecule. They tend to be aromatic ring systems that are linked directly, but can also be alicyclic [14] and can include a linking group α, but α would need to maintain the anisotropy in the core's electronic polarizability. Z and Z' are flexible substituents which are necessary both to lower the melting point of the bulk material and to help to stabilize the nematic phase [15]. They tend to be alkyl or alkoxy [16] chains and can branch, but often one is replaced by a much smaller polar substituent such as CN [17]. The β and γ linking groups can be present, but again the link tends to be direct.

It is impossible to predict with absolute certainty which mesophases (if any) will be present when heating a sample with a given molecular structure. Certain trends do exist, such as the correlation between shorter Z and Z' chains and the formation of a nematic rather than a smectic phase. A full and useful description of many common permutations of the template in figure 1.3 can be found in chapter 3 of [15].

Intermolecular forces such as pi-bonding between the aromatic rings that make up the core of some nematics cause them to preferentially align parallel to each other. An asymettircal core is also required for these intremolecular forces to generate a nematic phase, hence the abundance of two-unit cores in nematic mesogens [15].

The electrical polarizability of the molecule will be anisotropic due to the shape of the molecule, where charge distributions will be easier to induce along one axis more than another. The two molecular axes perpendicular to the long axis of the molecule have the same polarizability, and there are therefore two distinct molecular polarizabilities. This anisotropy in the polarizability leads directly to a dielectric anisotropy, diamagnetic anisotropy, and birefringence, which can be seen in aligned samples. The following sections show how the alignment between mesogens and the anisotropic polarizability can be exploited for use in electro-optic devices.

1.2 Characterizing and modelling nematic order

The fact that nematic molecules tend to have a non-zero average alignment is important for device applications. The anisotropic properties of LCs, in particular the birefringence and dielectric anisotropy, are not exhibited by isotropic liquids consisting of the same molecules. This section describes firstly how to parameterize the average orientation of a nematic sample in section 1.2.1, and then the scientific theory that accounts for the ordering in section 1.2.2.

1.2.1 The nematic order parameter

This average orientation of nematic mesogens can be parameterized by averaging the orientation of every molecule. For an angle ψ denoting the difference in angle between

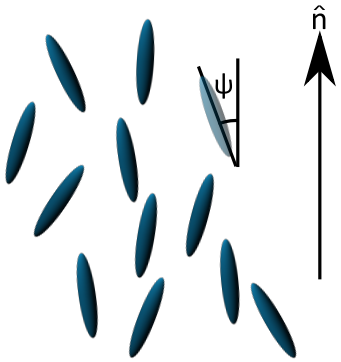

Figure 1.4: A diagram of typical ordering of nematic molecules, including definitions of $\hat{\boldsymbol{n}}$ and ψ

a unit vector $\hat{\boldsymbol{n}}$ pointing along the average orientation of the molecules (known as the director: see figure 1.4), this order parameter is often given using the second Legendre polynomial [18]:

$$S = \langle P_2(\cos\theta)\rangle = \left\langle \frac{3}{2}\cos^2\psi - \frac{1}{2} \right\rangle, \tag{1.1}$$

wherein the brackets indicate to take the average over all molecules in a sample. An important feature of LC molecules is that there is no polarity along the long axis, and hence reversing this axis has no effect on the physical behaviour. In other words, ψ and $-\psi$ are equivalent, hence the use of the Legendre polynomial as opposed to simply averaging ψ. The azimuth is absent from the equation as directions perpendicular to $\hat{\boldsymbol{n}}$ are equivalent in a nematic system.

The order parameter is sensitive to temperature, as thermal energy will cause molecules to deviate, on average, from lying parallel with $\hat{\boldsymbol{n}}$. The temperature dependence of S has been approximated by Haller [19]:

$$S = (1 - \frac{T}{T_c})^{\beta} \tag{1.2}$$

where T is the temperature of the nematic, and T_c and β are fitting parameters. This approximation is valid for temperatures well below the nematic to isotropic melting temperature, also known as the clearing temperature; T_c is within 2 °C of the clearing temperature in most nematics. The temperature dependence of physical LC properties

such as the birefringence, dielectric anisotropy and rotational viscosity can be approximated using this form of the order parameter [20].

1.2.2 Modelling nematic order

This section describes the physical laws that can be used to describe a bulk nematic sample, focusing on the static case i.e. ignoring fluid flow. The first validated theory used to describe the ordering of LCs was a static model proposed by the Swedish theoretician Carl Oseen, and extended by Charles Frank in 1958 [21]. The model is presented here, as it predicts important behaviours of an aligned LC sample, as well as the response to an electromagnetic field, described in more detail in section 1.4. Erickson and Leslie extended the theory to include the dynamic behaviour of LCs, and hence to describe the viscosities and time response of LCs; this model will be described in chapter 3. Furthermore, DeGennes introduced an order tensor given by $Q = \hat{\boldsymbol{n}} \otimes \hat{\boldsymbol{n}}$ which is invariant when transforming between $\hat{\boldsymbol{n}}$ and $-\hat{\boldsymbol{n}}$, and incorporated this parameter into the static model. More information on this Q-tensor and how it is used to model ordered LC samples can be found in [22].

1.2.3 Frank-Ossen free energy

The unit vector $\hat{\boldsymbol{n}}$ is a macroscopic parameter found by calculating the average orientation of the molecules in an LC sample. It is given in polar coordinates by:

$$\hat{\boldsymbol{n}} = \begin{pmatrix} \sin\theta\cos\phi \\ \sin\theta\sin\phi \\ \cos\theta \end{pmatrix} \tag{1.3}$$

where θ and ϕ are the standard spherical coordinates.

The next step is to define the free energy per unit volume of the system, which in this model is given as the sum $\tilde{\mathcal{F}}(\hat{\boldsymbol{n}}) = \tilde{\mathcal{F}}_d(\hat{\boldsymbol{n}}) + \tilde{\mathcal{F}}_e(\hat{\boldsymbol{n}})$, where $\tilde{\mathcal{F}}_d$ is the free energy associated with elastic forces between the molecules, and $\tilde{\mathcal{F}}_e$ is the energy associated with interactions between the molecules and an applied electrostatic field. $\tilde{\mathcal{F}}$ can be

thought of in the same way as the energy associated with distorting a spring from an equilibrium position. The energy associated with this distortion in the case of a spring is some constant multiplied by the square of the deviation from the equilibrium, but in the case of an LC there are several possible distortions, each with an associated spring constant.

There are restrictions on the terms that can be included in an expression for $\mathcal{F}_d$, such as the aforementioned invariance of $\hat{\boldsymbol{n}}$. Also, terms that involve a divergence integrated over the whole sample can be re-written as surface integrals [23], and therefore do not contribute to the internal energy of the system. The method by which all terms that satisfy these restrictions are found will not be reproduced here (see [24] for more details), but the resultant expression for $\mathcal{F}_d$ is given by:

$$\tilde{\mathcal{F}}_d = \frac{1}{2}K_1[\nabla \cdot \hat{\boldsymbol{n}}]^2 + \frac{1}{2}K_2[\hat{\boldsymbol{n}} \cdot (\nabla \times \hat{\boldsymbol{n}})]^2 + \frac{1}{2}K_3|\hat{\boldsymbol{n}} \times (\nabla \times \hat{\boldsymbol{n}})|^2. \tag{1.4}$$

Therefore there are three possible distortions from the equilibrium state of perfectly well aligned nematic mesogens, each scaled by $K_{1,2,3}$: elastic constants which work in the same way as the spring constant. These are material parameters with units of Newtons, and typical values range around the magnitude of 10^{-11} N, with K_3 often being ~ 2 times larger than $K_{1,2}$ [15].

The three possible distortions described by the terms $[\nabla \cdot \hat{\boldsymbol{n}}]^2$, $[\hat{\boldsymbol{n}} \cdot (\nabla \times \hat{\boldsymbol{n}})]^2$ and $|\hat{\boldsymbol{n}} \times (\nabla \times \hat{\boldsymbol{n}})|^2$ are known as the splay, twist and bend distortions, and are depicted in figure 1.5. $K_{1,2,3}$ will henceforth be labelled as the splay, twist or bend elastic constants.

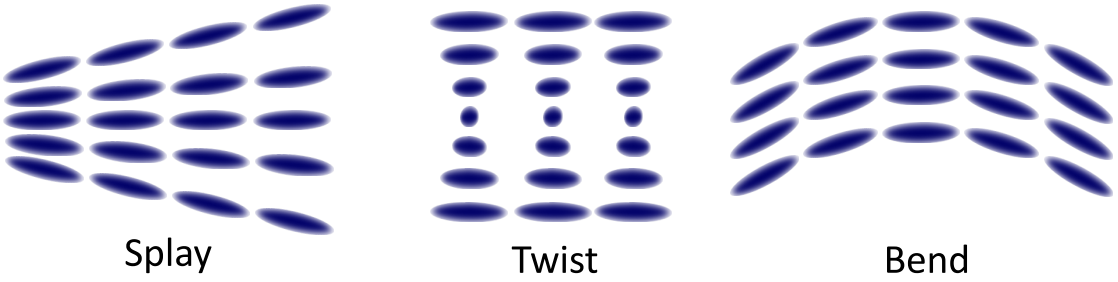

Figure 1.5: Geometry of the possible distortions present in calamitic LCs.

The most energetically favourable form of $\hat{\boldsymbol{n}}$ is that which minimizes $\mathcal{F}$ in equation (1.4). This mathematical form of $\hat{\boldsymbol{n}}$ will vary depending on the geometry boundary conditions, and the pertinent case for this report will be discussed later in section 1.4.

This section has described the fact that distortions from a perfectly aligned nematic sample can be described in terms of the three distortions shown in figure 1.5. The resistance to these distortions depends on the corresponding contribution to the free energy, where the distortions are quantified using the terms in equation (1.4) and scaled by three intrinsic elastic constants analogous to the spring constant.

1.3 Creating a uniaxial LC slab using a liquid crystal cell

The previous section has introduced a model that can be used to describe ordered samples of LC, and this section describes how such samples can be fabricated. It is important to control the alignment of an LC sample, so as to manipulate it for electro-optic applications. In particular, the resting state of the sample should be well aligned with a known director orientation and high order parameter. This section describes how LC alignment can be controlled using polymers, and how this can be used to create thin slabs of well-aligned nematic LCs.

1.3.1 Inducing order

There are several methods that can be used to fabricate surfaces that will align in-contact LC samples. Some noteworthy examples are photoaligning surfaces, where films undergo a photoisomerization process that results in aligning films [25] (this is discussed in greater detail in chapter 6); etching microgroove structures on e.g. glass substrates [26]; oblique evaporation of inorganic substances forming films with columnar structures [27]; and membranes formed on a water surface, and then transferred to a solid substrate [28]. However, the most reliable and common technique for creating aligning surfaces is to use a rotating cloth or brush to rub a thin polymer film, a method that is widely used in the display industry.

The origin of LC orientation due to contact with rubbed polymer layers was a matter of some dispute throughout the 20th century. Eventually, near-edge X-ray absorption fine structure (NEXAFS, [29]) was used by Stöhr and Samant [30] to precisely analyse the chemical structure at the surface of rubbed polyimide (PI). PI has been used as an alignment layer in most of the cells presented here, and therefore this example will be extremely useful.

The structure of the PI investigated by Stöhr and Samant is shown in figure 1.6.

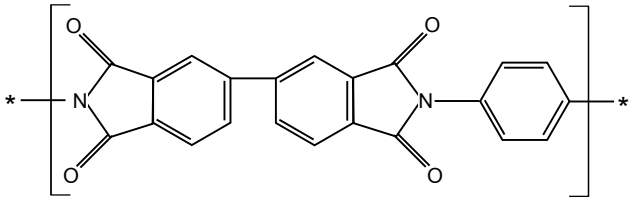

Figure 1.6: Chemical structure of BPDA-PDA polyimide from [30].

A rubbing cloth forces a greater percentage of the chains at the surface of the PI to point in the direction of the rubbing, and furthermore, chain segments that initially are orientated out-of-plane are preferentially forced to lie further in plane with a uniform azimuthal orientation, which results in a uniform azimuthal angle. The before and after rubbing orientations are shown in figure 1.7.

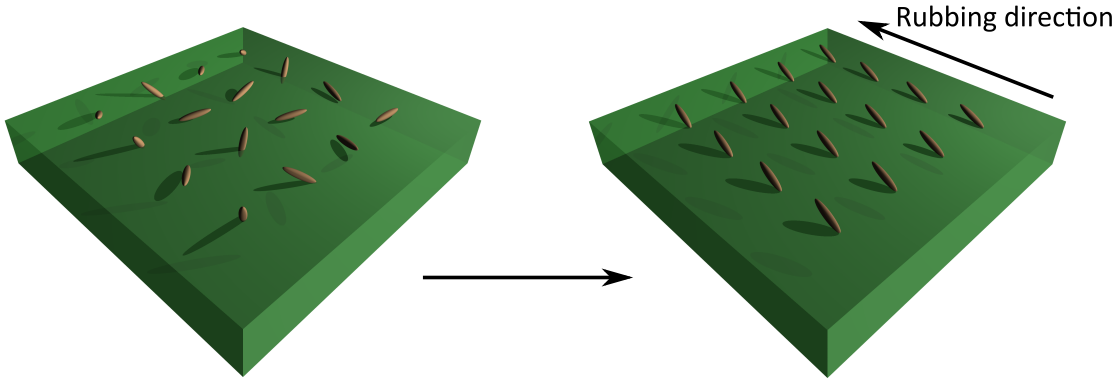

Figure 1.7: Phenyl-chains representing PI molecules are shown in red, orientated before and after PI rubbing. Fibres from the rotating cloth will interact with the surface chains, forcing them into this alignment.

Th π orbitals present in the core of a nematic mesogen are, unsurprisingly, orientated in the same way as those in the phenyl groups in the PI, causing the molecules to align parallel with the rubbed PI chains. The surface chains make some angle with the surface (as shown in figure 1.7), which causes the mesogens to lie slightly out of plane by an angle

known as the pre-tilt. The uniformity in the pre-tilt is very important for technological applications, as an asymmetry in the pre-tilt angle will lead to disclinations, particularly in twisted geometries. These disclinations will reduce the optical quality of a cell, as well as introduce unwanted switching effects [15].

It should be noted that this is a quasi-epitaxial effect [31], and as such it is a layer one molecule thick that is affected directly by being in contact with the polymer surface. However, such an orientation is able to propagate due to the affinity in the ordering between neighbouring mesogens, which can be used to create thin samples with a uniform alignment, as described in section 1.3.3.

1.3.2 Anchoring energy

The chemical interactions between LC mesogens and the treated surfaces described in the preceding section are known collectively as anchoring, and there is an associated energy: the anchoring energy. This is the energy required to break the bonds between an LC molecule and the surface, and has two values, one for rotation out of the plane known as polar anchoring energy, and one for in-plane rotations known as azimuthal anchoring energy [32].

Polar anchoring energy is considered to be strong if it takes a value of around 10^{-4} J/m^2, and weak for a value of around 10^{-6} J/m^2, and the azimuthal anchoring energy is generally two orders of magnitude lower than the polar anchoring energy for a given substrate [33]. It is possible to construct a free energy term for the anchoring energy, but generally it is assumed to be infinite, giving rise to the boundary conditions that fix a value for θ at the two surfaces.

1.3.3 Liquid crystal cells

A typical LC cell consists of two boundary surfaces where the LC director is fixed using one of the methods discussed in the previous section 1.3.1, as shown in figure 1.8. For the cells described in this thesis, polymer layers are spin-coated onto ITO coated glass substrates, and the resulting slides are fixed together using UV cured adhesive mixed

with spacer beads. The result is a gap with a thickness equal to the diameter of the spacer beads that can be filled with LC using capillary action. The geometry shown in figure 1.8 where the director at each boundary is identical is known as a planar geometry, although it can also be referred to as splay geometry, as a field applied perpendicular to the plane of the two boundaries will induce a splay distortion as shown in figure 1.5.

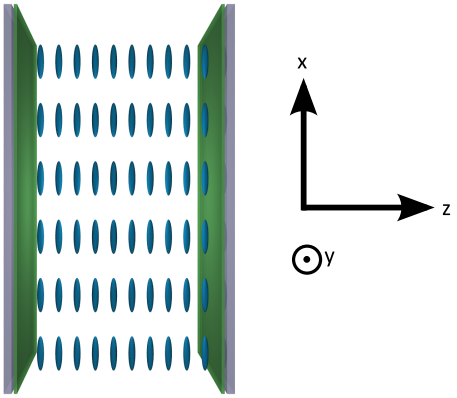

Figure 1.8: Two rubbed polymer layers can constitute a planar cell, where the LC molecules are all aligned in the same direction. Also shown are coordinates defining a plane in which the mesogens will align - these coordinates are used in the text.

This aligned slab of LC material is optically uniaxial due to the birefringence of LC molecules, with an optical axis lying parallel to the director of the cell, making an angle θ with x. Born and Wolf e.g. write in detail regarding non-LC uniaxial crystals [34], and the optical properties of such a cell are discussed in section 1.5. Briefly, the slab will act as a wave plate, where the phase difference between the two components of incident light (and hence the output polarization state) is dependent on the effective birefringence seen by the light, the thickness of the slab, and the wavelength of the incident light.

Two other common cell geometries are omitted here: the twist and homeotropic cells, both of which have a more significant role to play in the display industry than the planar geometry, but neither have been used to any great degree in the work described in this thesis. Diagrams of the two geometries are shown in figure 1.9 for reference.

The creation of thin, highly birefringent uniaxial crystal structures using LCs would potentially have useful applications, but it is the field control of the orientation of nematic mesogens that leads to their use in many optical technologies. How the LC responds to external fields is described in the following section, 1.4.

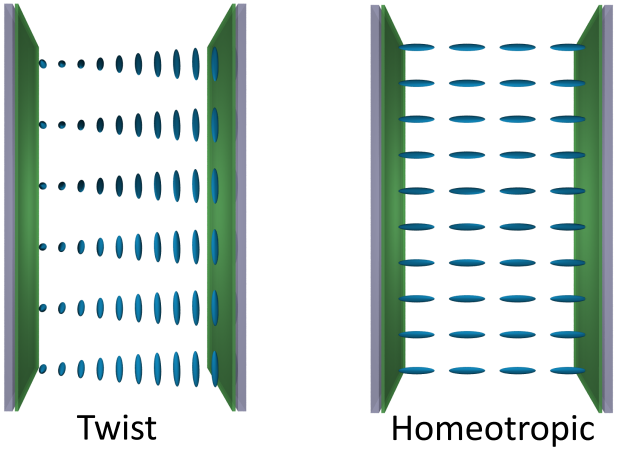

Figure 1.9: Twisted and homeotropic cell geometries.

1.4 Liquid crystals in external fields

This section will discuss the response of an aligned LC sample to an applied electric or magnetic field. It shall be shown that the application of an electric or magnetic field introduces a free energy term into the Frank-Oseen equation, which leads to reorientation above a threshold field. The electric field component of an optical field can also induce this kind of switching [35], but the light sources used in this thesis are not of a sufficiently high intensity to allow this kind of switching. The formulism here is adapted from [15].

1.4.1 The effect of applying an electric or magnetic field

The physics behind the response of an LC sample to an electric field is very similar to that of an applied magnetic field, where an additional term is added to the free energy expression defined in equation (1.4). Therefore, the electric field case will be treated first, and in far more detail than the magnetic field case. Chapter 5 describes the use of a magnetic field to characterize hybrid nematic cells, but the treatment is slightly different in this case due to an additional bias field applied orthogonal to the switching field.

A pure LC can be treated as a dielectric. In this case, an applied electric field will induce a polarization given by:

$$\mathbf{P} = \epsilon_0 \epsilon \mathbf{E}, \tag{1.5}$$

where $\boldsymbol{E}$ is the applied field. We have to consider the form that ϵ takes given the fact that the LC is anisotropic, as the polarization will not necessarily be parallel to the field inducing it. There are two values for the dielectric constant one along the long axis and one along the two short axes, so ϵ is given by a rank two tensor diagonalized to give:

$$\mathbf{P} = \epsilon_0 \begin{pmatrix} \epsilon_{\parallel} & 0 & 0 \\ 0 & \epsilon_{\perp} & 0 \\ 0 & 0 & \epsilon_{\perp} \end{pmatrix} \mathbf{E} \tag{1.6}$$

The polarization across each axis can be found as:

$$\begin{aligned} P_{\parallel} &= \epsilon_0 \epsilon_{\parallel} \cos(\theta) |\boldsymbol{E}| \\ P_{\perp} &= \epsilon_0 \epsilon_{\perp} \sin(\theta) |\boldsymbol{E}|, \end{aligned} \tag{1.7}$$

for a mesogen with any generic alignment as shown in figure 1.10 along with the angle θ that $\hat{\boldsymbol{n}}$ makes with the x axis.

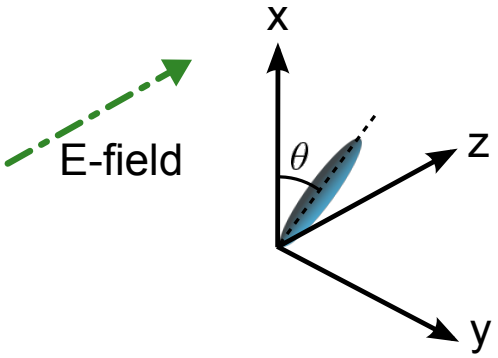

Figure 1.10: A generalized depiction of an LC mesogen aligned parallel to $\hat{\boldsymbol{n}}$ in an electric field, showing the coordinate geometry used in the text.

In order to work out the stable director profile under the application of an electric field, we need to consider how this polarization and its interaction with the applied field contributes to the free energy of the system. After that, it is simply a case of finding the director field which minimizes the resulting free energy function.

The contribution of the polarization to the internal energy of the system is given by:

$$U = \frac{\boldsymbol{E} \cdot \boldsymbol{P}}{2} \tag{1.8}$$

This can be expanded using the expression for $\boldsymbol{P}$ from equation (1.5), and excluding terms with no angular dependence, this gives:

$$f_E = -\frac{\epsilon_0 \Delta\epsilon}{2}|\boldsymbol{E}|^2 \cos^2(\theta), \tag{1.9}$$

or, in terms of the director:

$$f_E = -\frac{\epsilon_0 \Delta\epsilon}{2}(\boldsymbol{E}\cdot\hat{\boldsymbol{n}})^2. \tag{1.10}$$

For a positive value of $\Delta\epsilon$, the lowest energy state corresponds to the field and the director lying parallel to each other. This is the reason for f_E being scaled - the energy is at the lowest value when $\boldsymbol{E}\cdot\hat{\boldsymbol{n}}$ is at the highest value.

The free energy of such a system is given by adding this term to equation (1.4):

$$\tilde{\mathcal{F}}_d = \frac{1}{2}K_1[\nabla\cdot\hat{\boldsymbol{n}}]^2 + \frac{1}{2}K_2[\hat{\boldsymbol{n}}\cdot(\nabla\times\hat{\boldsymbol{n}})]^2 + \frac{1}{2}K_3|\hat{\boldsymbol{n}}\times(\nabla\times\hat{\boldsymbol{n}})|^2 - \frac{\epsilon_0\Delta\epsilon}{2}(\boldsymbol{E}\cdot\hat{\boldsymbol{n}})^2. \tag{1.11}$$

This expression can be minimized for specific LC geometries, so let us consider a planar cell, where it is assumed that the rotation due to the electric field is in a single plane, and there are consequently no twist deformations. The case is depicted in figure 1.8 with the coordinate system from figure 1.10.

Assuming 0 pre-tilt, the director is constrained to be 0 at the boundaries due to anchoring (see section 1.3.1) to two rubbed polymer surfaces, and will vary with z ($\theta = \theta(z)$). It has x and z components, where:

$$n_x = \cos(\theta), \quad n_z = \sin(\theta). \tag{1.12}$$

The elastic energy derivatives in equation (1.11) are given by:

$$\begin{aligned} \nabla\cdot\hat{\boldsymbol{n}} &= \left(\frac{dn_z}{dz}\right)_{x,y} \\ \hat{\boldsymbol{n}}\cdot(\nabla\times\hat{\boldsymbol{n}}) &= 0 \\ |\hat{\boldsymbol{n}}\times(\nabla\times\hat{\boldsymbol{n}})| &= \left|\left(\frac{dn_x}{dz}\right)_{x,y}\right|. \end{aligned} \tag{1.13}$$

Substituting these expressions into equation (1.11) gives the expression for the free energy per unit volume:

$$\tilde{\mathcal{F}}_d = \frac{1}{2}(K_1 \cos^2\theta + K_3 \sin^2\theta)\left(\frac{d\theta}{dz}\right)^2 - \frac{1}{2}\epsilon_0 \Delta\epsilon E^2 \sin^2\theta. \tag{1.14}$$

We need to find the director configuration that minimizes the total free energy, i.e. the integral of $\tilde{\mathcal{F}}_d$ from $z = 0$ to $z = d$. Therefore, the problem is to find a function for θ that gives the smallest value of:

$$F_A = \int_0^d \left[\frac{1}{2}(K_1 \cos^2\theta + K_3 \sin^2\theta)\left(\frac{d\theta}{dz}\right)^2 - \frac{1}{2}\epsilon_0 \Delta\epsilon E^2 \sin^2\theta\right] dz. \tag{1.15}$$

The minimization problem is solved using calculus of variations as shown in the textbook of Collings and Hird [15]. This method involves forming an expression for $\theta(z)$ that uses the fact that small variations from the function that minimizes F_A cannot change F_A to first order in the variable causing that change. The linear change in F_A with respect to this variable must therefore equal 0, and thus an equation can be devised which leads to an Euler-Lagrange equation:

$$(K_1 \cos^2\theta + K_3 \sin^2\theta)\left(\frac{d^2\theta}{dz^2}\right) + \left[(K_3 - K_1)\left(\frac{d\theta}{dz}\right)^2 + \epsilon_0 \Delta\epsilon E^2\right] \sin\theta\cos\theta = 0. \tag{1.16}$$

This differential equation is solved using the boundary conditions $\theta = 0$ at $z = 0, d$ The solution $\theta = 0$ at all values of z is stable below a certain value for E, which is known as the Frederiks threshold or Fredericks transition. For values of E higher than this threshold, small perturbations in E cause the solution $\theta = 0$ to be unstable, and a non-uniform solution for θ can be found that is stable - this stable solution for $\theta(z)$ is what is observed in physical systems.

To find the Frederiks threshold, (1.16) is simplified for the case of a field very near to the Frederiks threshold where θ is very small at all points in the cell. The resulting simplified equation is:

$$K_1\left(\frac{d^2\theta}{dz^2}\right) + \epsilon_0 \Delta\epsilon E^2 \sin\theta\cos\theta = 0, \tag{1.17}$$

which has a stable solution for $\theta = 0$ below a field value, given by:

$$E_c = \frac{\pi}{d}\sqrt{\frac{K_1}{\epsilon_0 \Delta\epsilon}}. \tag{1.18}$$

This Frederiks threshold is of huge importance when designing devices, as high field requirements are hard to obtain safely in most applications.

The Frederiks threshold can also be written in terms of the voltage applied to an LC layer. Using the relationshop $E = V/d$, the threshold becomes:

$$V_c = \pi\sqrt{\frac{K_1}{\epsilon_0 \Delta\epsilon}}, \tag{1.19}$$

which has no dependence on the thickness of the cell, and the voltage transition becomes a constant material property of the LC under investigation; a relatively simple conclusion that is nonetheless extremely important in much of the work that follows. The term Frederiks transition can refer to either the electric field of the voltage threshold, and is used in this thesis to refer to the voltage transition unless otherwise stated.

One can treat the magnetic field case in a very similar way, wherein the term defined in equation (1.10) is replaced by the equivalent term $\mu_0 \Delta\chi(\boldsymbol{H} \cdot \hat{\boldsymbol{n}})^2/2$ for diamagnetic interactions, giving a similar form for the Frederiks transition:

$$H_c = \frac{\pi}{d}\sqrt{\frac{K_1}{\mu_0 \Delta\chi}}, \tag{1.20}$$

where $\boldsymbol{H}$ is the internal magnetic field, μ_0 is the permeability of free space and $\Delta\chi$ is the diamagnetic anisotropy of an LC [36]. Very large magnetic fields of ~ 1000 Am^{-1} are generally required to switch even very thick cells [37] thanks to typically low values of diamagnetic anisotropy, which necessitates the use of large electromagnetic coils. It is for this reason that electric fields are generally used in modern LC devices, despite the added engineering challenge of depositing transparent electrodes onto the cell surfaces.

1.5 Optical properties of LC cells

The properties of LCs in a planar alignment - namely the birefringence and the reorientation due to an applied field - have been discussed, and can now be drawn together to show why LC cells are such useful and powerful electro-optic devices. Similar considerations can be applied to twisted cells that were originally used in display technology, although the mechanism behind the control of the polarization of light is somewhat different than for planar cells [38].

Linearly polarised light passing through a birefringent medium can be resolved into two orthogonal polarization components, each lying parallel to one of the two refractive index axes, which in turn means that the two components will travel at two different speeds in the medium. The resultant phase difference between the two components of the light is dependent on the distance travelled through the medium, the wavelength of the incident light and the value for birefringence itself (d, λ and Δn respectively), and is given by [34]:

$$\delta = \frac{2\pi d}{\lambda}\Delta n. \tag{1.21}$$

The polarization state of the light will depend on the value of δ, and will generally be elliptical. The state itself can be determined by passing the light through a linear polarizer and measuring the resultant intensity, which can vary between 0 and a maximum value equal to the initial light intensity, depending on the relative alignment of the initial polarization, initial director and the angle of the transmission angle of the polarizer.

For light polarized at 45° to the initial LC director of a planar cell, the phase shift δ between the two orthogonal components of the light will be at a maximum value and can take values of several factors of π. This is due to the birefringence of the slab being as high as possible in this configuration. As the LC starts to re-orientate above transition, the refractive index of the optical axis begins to decrease, as the projection of the long axis of the directior with a vector lying in the plane of the cell wall will decrease as shown in figure 1.11.

We can define an effective refractive index that changes with the angle θ that $\hat{\boldsymbol{n}}$ makes with the x axis using the expression for the phase velocity of light passing through a

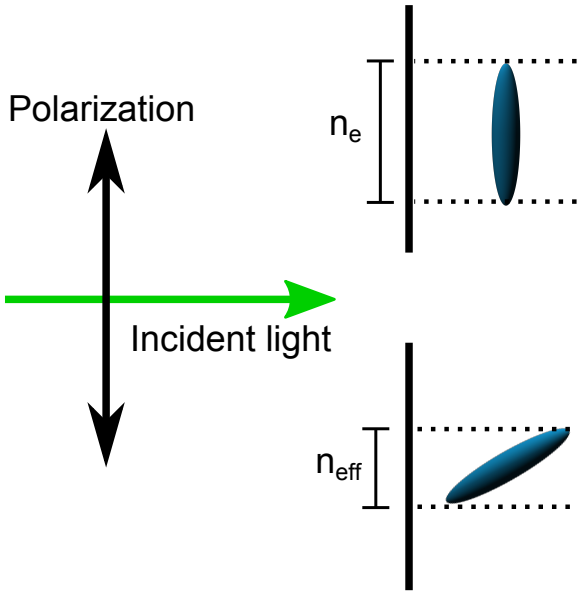

Figure 1.11: A light wave entering an orientated LC sample will see a smaller projection of the long-axis index of refraction, n_e. The molecule pictured here is aligned parallel to the director. This so-called effective refractive index is given by equation (1.22)

uniaxial crystal [34]:

$$n_{\text{eff}}(\theta) = \frac{n_e n_o}{\sqrt{n_e^2 \cos^2\theta + n_o^2 \sin^2\theta}}, \tag{1.22}$$

and the phase shift induced between the two polarization components of the incident light can instead be written as:

$$\delta = \frac{2\pi d}{\lambda}[n_o - n_{\text{eff}}(\theta)], \tag{1.23}$$

where d is the LC layer thickness, and λ is the wavelength of the incident light. Note that in the extreme cases of $\theta = 0, \pi/2$, the effective refractive index becomes n_e, n_o respectively. Therefore, one would expect to see that as the voltage applied to a planar cell increases, the phase shift decreases until the LC is effectively forced to align homeotropically, at which point the phase shift will be 0.

This change in the phase shift, along with the introduction of polarizers mentioned above, can be used to change the intensity of light transmitted from a device according to the electric field applied to it. These kinds of devices are inexpensive, thin, efficient and miniatuarizable, which is what has made liquid crystals such an attractive technology for

the display industry. However, hybrid cells described in chapters 5, 4 and 6 offer far more functionality than simply manipulating the intensity of light using a glass/polymer/LC structure, and the aim of this thesis is to show this through experimentation and theory. The experiments used to characterize different kinds of cells are described in the following chapter.

Chapter 2

Electro- and magneto-optic characterization of liquid crystal cells

There are many different experimental techniques available to characterize LC materials and devices. This chapter will describe a selection of these techniques in some detail, with particular emphasis on those used throughout the rest of this thesis. The techniques discussed are summarized in table 2.1.

Experimental technique	Device/material to be tested	Property under investigation
Interference spectrometry	Empty cell	Thickness
Clearing point measurement	Standard nematic materials	Clearing point
Capacitance measurements	Standard nematic cells	$\Delta\epsilon$
Crossed polarised intensity	Standard nematic cells	Δn, Frederiks transition, elastic constant, time response, voltage transfer function (VTF).
Two-beam coupling (TBC)	Photorefractive systems	Beam coupling efficiency
Diffraction efficiency measurement	Photorefractive systems	Diffraction efficiency

Table 2.1: Table outlining the experimental techniques discussed in this chapter, as well as the systems they are used to characterize, and the parameters measured. Use of the crossed polarised intensity to measure the time response and the voltage transfer function are the subjects of chapters 3 and 4

Knowledge of the values these properties take is essential in order to predict device/-material behaviour, and to compare between different systems. The thickness of the cell determines the maximum phase shift of light passing through the LC layer, as well as having an effect on the magnetic Frederiks transition (section 1.4.1) and it is used when calculating the birefringence of an LC material from a crossed polariser intensity measurement (section 2.4). The clearing point described in section 1.2.1 is important to consider as the nematic phase should be maintained for the experiments, and in addition it is a parameter investigated in chapter 5, where the addition of nanoparticle colloids to nematic solvents can affect the clearing temperature. The dielectric anisotropy, Frederiks transition, elastic constants and birefringence are all described in chapter 1, and describe exactly how an LC cell will manipulate light when subject to an electric field.

The voltage transfer function (VTF) is a novel multi-spectrum technique, based on crossed polarised intensity (CPI) measurements, that gives information regarding the relative conductivities of the constituent layers in a cell as well as the time response of an LC, although the time response can be more accurately measured using a technique described in chapter 3. The final two parameters, beam coupling and diffraction efficiency, are used to measure the strength of the photorefractive response exhibited by liquid crystal light valves (LCLVs) - hybrid devices which include a photoconductive aligning layer. The higher these parameters are, the greater the light-induced modulation of the refractive index of the systems.

Descriptions of each of these techniques, and how they can be used to measure the appropriate properties are given in this chapter. The analysis of the errors associated with each technique can be found in appendix A.

2.1 Thickness measurement

The thickness of an empty cell is measured using an interferometric technique that relies on the fact that the two glass slides act as a Fabry-Perot etalon where the thickness of the cell is equal to the length of the etalon. The theory of such etalons is described by Born and Wolf in [34]. At the most basic level, light at normal incidence propogating

across an etalon will pick up a phase shift, $\delta_1 = 2\pi nd/\lambda$ where n is the refractive index (1 in this case), d the thickness of the etalon, and λ the wavelength of the incident light, which is varied using a spectrometer for this method.

At the glass boundary, most of the light will be transmitted, but some will be reflected back and be re-transmitted after two passes. Therefore, the phase shift between two subsequent transmission events will be given by $\delta_t = 2\delta_1$. The two components will interfere constructively if the phase shift is equal to an integer number of wavelengths, and from this one can show that peaks in the intensity will occur at frequencies which are separated by:

$$\Delta\omega = \frac{c}{2d} \tag{2.1}$$

where c is the speed of light, and a conversion from the wavelength to the frequency is necessary. $\Delta\omega$ in equation (2.1) is also known as the free spectral range of the cavity. This equation is valid for an empty cell, where the refractive index of the medium (air) can be assumed to be 1.

In order to measure $\Delta\omega$, white light is transmitted through an empty cell and the resulting intensity is measured as a function of wavelength by an Ocean Optics USB2000 series spectrometer, which uses a tiltable diffraction grating to measure the wavelength. The resulting thickness is calculated by measuring the frequency separation 10 peaks in the resulting spectrum and inserting the measured value of $\Delta\omega$ into equation (2.1). 10 peaks are used to increase reliability, and the result is accurate to the nearest 0.1 μm.

The light used in this experiment is generally incident towards the centre of the cell. However, it is not correct to assume that the thickness of the cell is uniform at all points. While every effort is made to ensure the experiments take place in the same area measured in this way, it is always important to keep this variation in mind as a source of possible error.

2.2 Clearing point

The clearing point is another name for the temperature at which the LC phase transitions into the isotropic liquid phase, and is integral for defining the temperature dependence of

the order parameter as discussed in section 1.2.1. Clearing temperatures well above room temperature tend to be required in most practical applications, as constant cooling or heating of devices is energy intensive. Therefore, accurate measurements of the clearing point of LC materials are important when choosing materials for applications. This section outlines two techniques used to measure clearing temperature, although they are often used concurrently.

2.2.1 Differential scanning calorimetry

Differential scanning calorimetry (DSC) is the most accurate way to measure phase transitions of materials. It consists of a reference sample of material with a well known specific heat capacity which is heated to match the temperature of the material under investigation. If the material undergoes a first-order phase transition (i.e. a transition that involves latent heat [39]), then the specific heat capacity of the material will change, which will be indicated by changes in the heat flow required to keep the samples in thermal equilibrium. The energy imbalance between the two samples allows one to record the enthalpy of transition for the investigated sample - in this case a liquid crystal. DSC is used in a wide range of industrial and research areas, and more details can be found in [40].

2.2.2 Polarizing microscopy

The enthalpy required to affect a phase transition is often insufficient to identify a phase transition, as multiple LC mesophases can be achieved by heating or cooling any one single LC material. Therefore, it is common to combine a DSC trace with polarizing microscopy in order to determine exactly which phase transition has been identified by the DSC trace.

The sample is loaded onto a heating stage, and then observed between crossed polarizers using a microscope. An isotropic liquid would appear black in such a setup, but an anisotropic material such as an LC will present some form of “texture”. As mentioned in chapter 1, LC defects can form in samples with no forced director profile. Mathematical

treatment of these defects is somewhat complex [41], but it can be shown that the defect formation in nematics can result in so-called schlieren brushes: dark areas where the director is aligned parallel or perpendicular to the input light polarization. Point and line defects and the equivalent schlieren brushes are shown in figure 2.2, and a photograph of a typical observed pattern is shown in the photograph 2.1.

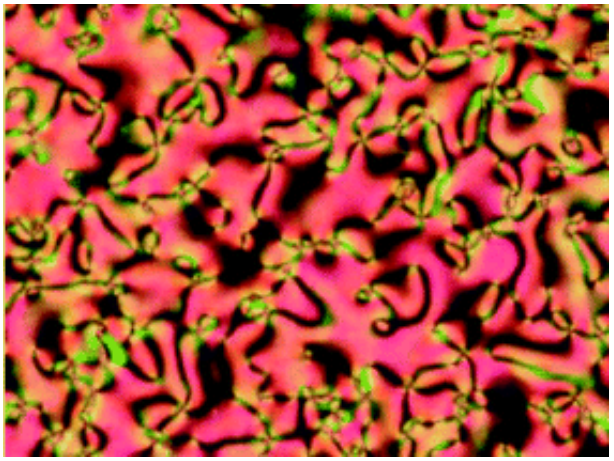

Figure 2.1: Schlieren texture as observed under a polarising optical microscope from [42]

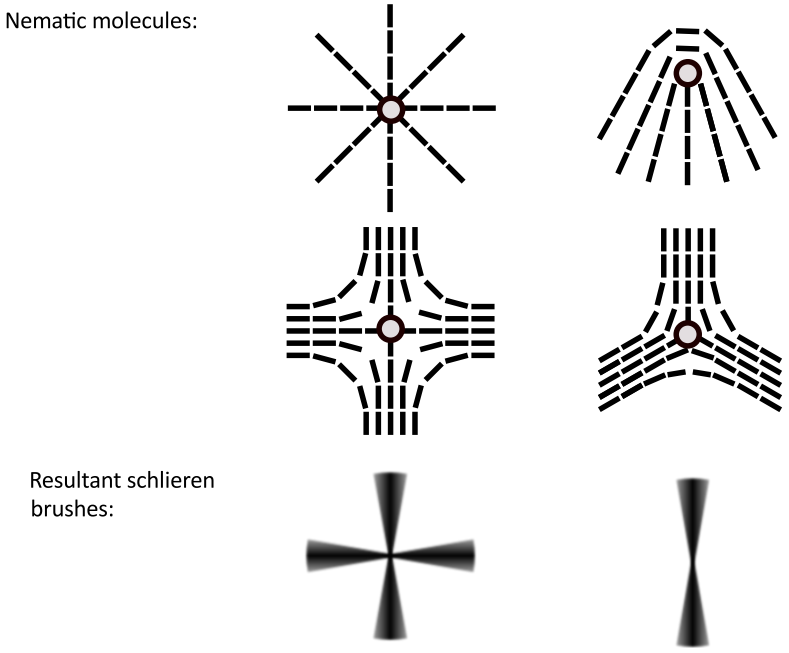

Figure 2.2: The director configurations that result in schlieren textures. In this case, the crossed polarizers would be aligned horizontally and vertically to achieve the depicted schlieren brushes.

Other LC mesophases can be identified by their own unique optical textures [15].

Therefore, in order to measure the nematic to isotropic transition temperature, DSC can be performed first in order to identify phase transition and then those temperatures can be investigated by observing the sample under polarized light in order to identify which phases or mesophases are undergoing the transition. However, the DSC stage of the experiment is not necessary in all cases - if it is known that there is only one LC phase for a specific mixture, or if a known clearing point has only been slightly affected by the addition of nanoparticles to an LC material, then polarizing microscopy can be used to observe the phase shift.

2.3 Measuring the dielectric anisotropy

The dielectric anisotropy ($\Delta\epsilon$) of an LC directly affects the Frederiks transition, and hence the electrical efficiency of a device using that material, which can in turn affect the operating voltage and efficiency of LC devices. It will be shown that a capacitance bridge can be used to accurately measure $\Delta\epsilon$.

2.3.1 LC cells as capacitors

The LC cell can be treated as a capacitor, consisting of two parallel ITO plates with a dielectric layer sandwiched in between. In this case, the capacitance is given by:

$$C = \epsilon_o \epsilon_{\text{eff}} \frac{A}{d}, \tag{2.2}$$

where ϵ_{eff} is the dielectric constant of the layer, A is the dielectric layer area and d the thickness. Units for d and A are irrelevant, as the measurement of LC $\Delta\epsilon$ consists of measuring C for an empty, and then a filled cell. As $\epsilon_o \approx 1$ for air, the ratio of C for these two cases results in ϵ_{eff} for the LC layer.

It only remains to measure ϵ_{eff} parallel and perpendicular to the director. This can be achieved by applying a DC voltage to the cell; a 0 V signal will allow one to measure ϵ_o, and a sufficiently high voltage to measure ϵ_e. The change in dielectric constant with voltage tends to become very small when the LC is completely aligned parallel to the

applied electric field, and therefore the point at which ϵ_e is being measured is normally obvious thanks to the value becoming constant with voltage. However, the voltage at which total re-alignment is achieved can be checked by performing a CPI experiment.

A Wayne Kerr precision capacitance bridge (B905) is used to measure the capacitance of cells in this thesis. A simplified circuit diagram is shown in figure 2.3.

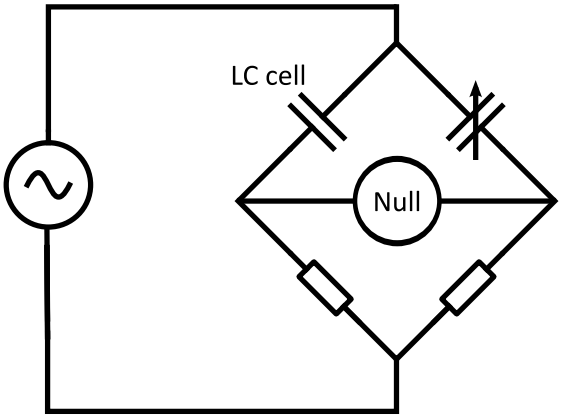

Figure 2.3: Electronic schematic of a simple capacitance bridge to measure the capacitance of an LC cell.

The variable capacitor is adjusted to balance the capacitance of the sample (in this case, an LC cell), at which point a null voltage will be recorded between the points shown in figure 2.3. The value of the variable capacitor is now equal to the capacitance of the sample, and the ratio between this value for an empty and a filled cell will give the dielectric constants.

2.3.2 The effect of electrode shape on measurements of capacitance

Section 1.3 describes how UV curable adhesive is used to fix two slides together while also controlling the thickness of the layer. Figure 2.4 shows two common shapes for ITO electrodes, and indicates the approximate positioning of the UV glue in each case. The rectangular electrodes shown in figure 2.4(a) have the glue lying between the two electrodes, which is not the case for the so-called guard electrodes [43] in figure 2.4(b). As the glue is a dielectric between the two conductive plates, with a constant relative permittivity of around 2.7 [44], a significant systematic error in the capacitance measurement would be introduced, which will follow through to the measurement of $\Delta\epsilon$,

and therefore it is often preferable to use guard electrodes when $\Delta\epsilon$ must be known to a good degree of accuracy, as in chapter 5. Guard electrodes is a term that can also be applied to guard-ring electrodes, as referenced in [45], but it is the electrode shape shown in figure 2.4 that is referred to as guard electrodes in this thesis.

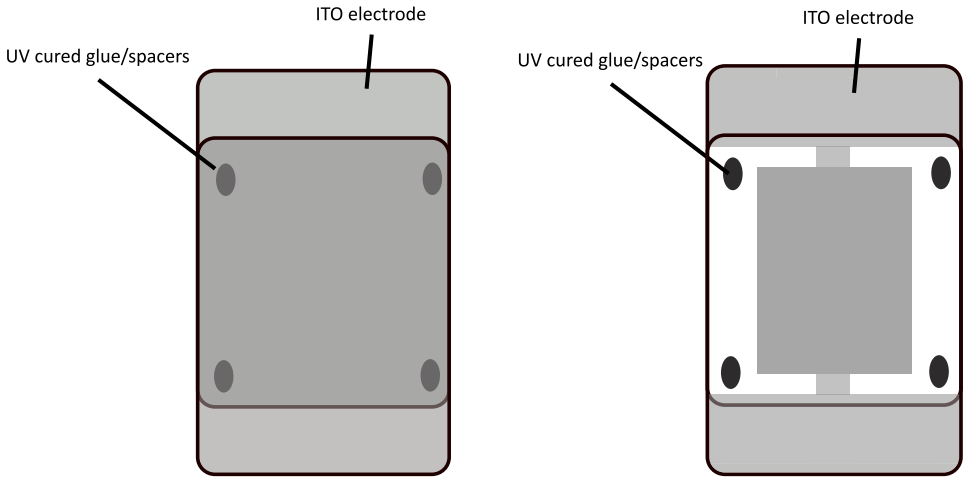

Figure 2.4: a.) Non-patterned ITO electrodes and b.) Guard electrodes, where the glue cannot affect measurements of capacitance

2.4 Crossed polarized intensity (CPI)

The birefringence and dielectric anisotropy of nematic LCs can be used to create a cell that acts as an electrically controlled waveplate. Measuring the phase lag induced as light passes through the cell allows us to characterize this electro-optic behaviour, as well as measuring important properties such as birefringence, Frederiks transition and elastic constants (depending on the geometry of the cell). This section will discuss how to use the CPI to measure the birefringence of an LC having measured the thickness of the LC layer. In chapter 3 measurements of the elastic constants $K_{1,3}$ will be described, and the measurement of the Fredericks transition will be described in chapter 5.

Restricting the discussion to planar cells, the setup is shown in figure 2.5.

It should be noted that the AC generator and diode-pumped-solid-state (DPSS) laser shown in figure 2.5 could be replaced by a DC generator and an alternative laser source respectively. For the purposes of this thesis, an AC field was generally used to switch the

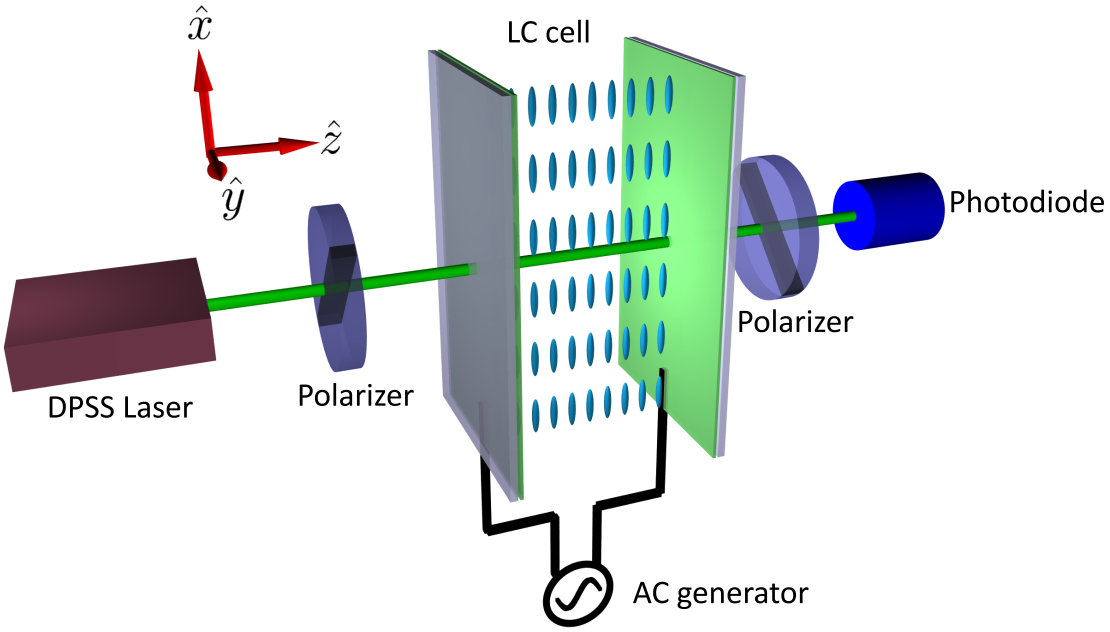

Figure 2.5: An experimental schematic showing the CPI experiment.

LC layer as DC fields can cause ionic charge layers to build up in the device and screen the electric field, an effect described e.g. by Scalerandi *et al.* [46]. A green 532 nm DPSS laser with a variable ND filter provided sufficient power for the whole range of experiments.

With no voltage applied to the cell and with incident light polarized at 45° to the initial LC director, the phase shift experienced by the light is at a maximum. After the light has passed through the cell, the two orthogonal components of the polarization will have undergone a phase shift that will be dependent on the birefringence, LC layer thickness, the wavelength of the incident light and the orientation of the LC molecules, which will generally result in an elliptically polarised output. A linear polarizer can be used to convert the output polarization state to an intensity variation, as the output intensity will depend on the polarization of the light output from the cell - generally the analyzer polarizer is perpendicular to the initial polarization, hence the name crossed polarized intensity. The fact that the output light intensity can be controlled by an applied electric or magnetic field explains how LC cells find such a wide variety of uses in optics and display technologies.

2.4.1 Calculating the maximum phase shift using a CPI measurement

It is useful to have a mathematical expression for the phase difference between two orthogonal light beams that have passed through an LC cell, as it can be used to calculate useful properties of the material being used. The maximum phase shift is given by:

$$\delta_{\max} = \frac{2\pi d}{\lambda}\Delta n \tag{2.3}$$

where λ is the wavelength of the incident light, d is the thickness of the cell and Δn is the birefringence of the material. As the wavelength is generally known, and other techniques exist to measure the thickness of an unfilled cell, CPI data are mostly used to calculate the birefringence as described in this section. The Frederiks transition can be read directly from the data, and the elastic constants can be used as fitting parameters when modelling the data.

For reference, an example trace of the intensity as a function of the applied voltage is shown in figure 2.6.

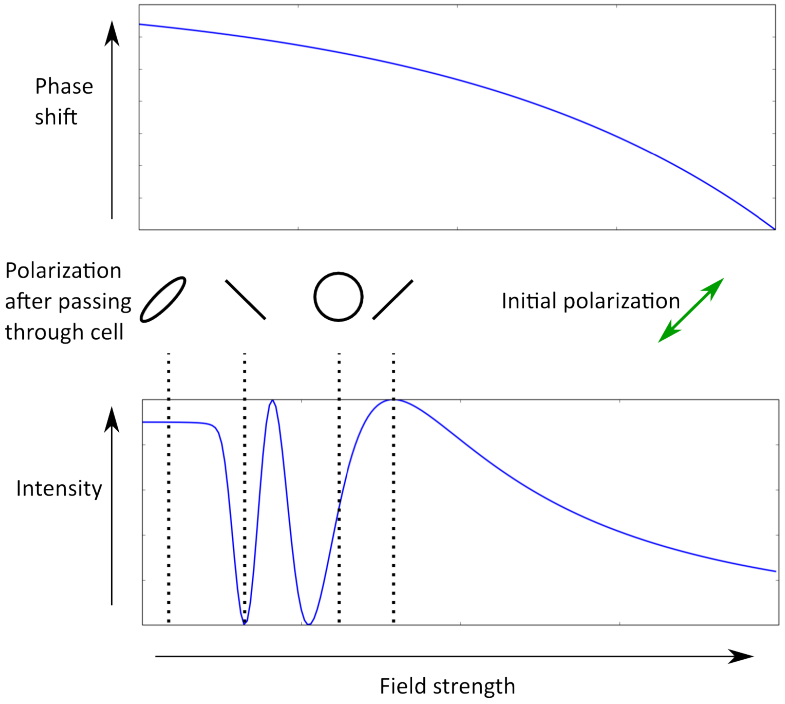

Figure 2.6: The change of the phase shift as a function of the applied field is shown at the top of the figure. The resultant polarization states for four different phase shifts are shown in the centre of the figure, along with the initial polarization of the light incident on the cell. The resultant intensity of the light after passing through the analyzer polarizer (as a function of the applied field amplitude) is shown in the bottom part of the figure.

The behaviour observed in figure 2.6 can be explained by considering the liquid crystal cell as a waveplate, with a voltage dependent birefringence, and hence phase shift. At high voltages, the cell reaches a homeotropic state where $\delta = 0$, whereas at zero volts the phase difference takes the maximum possible value. It will be shown that the voltage dependent phase shift between these two extrema will lead to the intensity profile in figure 2.6.

Linearly polarized light enters the cell, is resolved into two orthogonal components parallel to the ordinary and extraordinary axis of the LC, each component experiences a unique phase delay, and in general the combined output components result in elliptically polarised light output from the cell. In the special case where the phase shift seen by the components is equal to 0, or some integer multiple of π, the output is linearly polarised, and the intensity output from the analyzer polarizer shown in figure 2.5 will be either

0% or 100% of the maximum signal. At any other phase shift, the signal amplitude depends on the ellipticity of the light exiting the cell, and the intensity is therefore voltage dependent.

The phase difference δ between the two orthogonal beams is:

$$\delta = \frac{2\pi d}{\lambda}\Delta n(V) \tag{2.4}$$

where d is the thickness of the LC layer, $\Delta n(V)$ is the voltage dependent birefringence of the LC and λ is the wavelength of the light. Equation (2.4) assumes an angle of $\frac{\pi}{2}$ between the propagation direction of the light and the optical axis of the LC - easily achievable when setting up an experiment. If the CPI can be used to measure δ for an undistorted LC layer (i.e. the value for δ with 0 V applied to the cell), then knowing the values for two of the parameters λ, d and Δn will lead to a measurement of the third. This is particularly useful as λ is generally well known and d can be measured before filling a cell as described in section 2.1, leading to an accurate measurement of birefringence.

2.4.1.1 CPI of light passing through an anisotropic medium

In order to relate the intensity in figure 2.6, we need to determine the effect of the LC layer on two orthogonal light polarizations resolved parallel to n_o and n_e. Treating the LC layer as a uniaxial slab, we can proceed as Born and Wolf [34]. In figure 2.7, $\mathbf{n}_o$ and $\mathbf{n}_e$ are vectors pointing along the ordinary and extraordinary refractive indices respectively. OP is the initial polarization of the light, and OA is the orientation of the analyzer polarizer. OE is the amplitude of light incident on the LC layer.

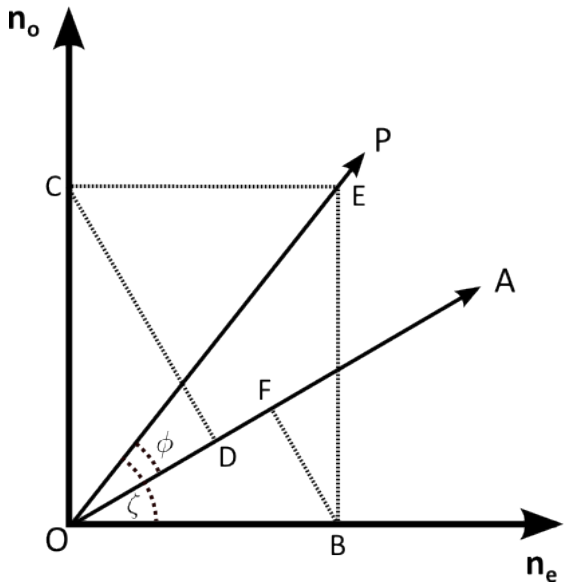

Figure 2.7: Components of a light wave travelling through an LC layer at 0 V

The first step is to resolve the light along OE onto $\mathbf{n}_o$ and $\mathbf{n}_e$, like so:

$$OB = E\cos\zeta, \quad OC = E\sin\zeta, \tag{2.5}$$

after which the components parallel to OA are found, as these are the electric fields transmitted by the analyzer:

$$OD = E\cos\zeta\cos(\zeta-\phi), \quad OF = E\sin\zeta\cos(\zeta-\phi). \tag{2.6}$$

The electric fields of the two waves superimpose after leaving the analyzer, with the total intensity (see chapter 7 of [34]) given by:

$$I = I_1 + I_2 + 2\sqrt{I_1 I_2}\cos\delta, \tag{2.7}$$

where δ is the phase difference defined in equation (2.4) and $I_{1,2}$ are the intensities of the components, found by squaring the electric fields found in equation (2.6). After some trigonemtric manipulation, one can find that equation gives us:

$$I = E^2\left[\cos^2\phi - \sin 2\zeta\sin 2(\zeta-\phi)\sin^2\frac{\delta}{2}\right]. \tag{2.8}$$

This is a general formulation of the intensity output from the CPI experiment, so we can now look at cases which simplify the expression. If the polarizers are parallel with the incident polarization aligned at 45° to the orthogonal refractive index vectors, then:

$$I_{\parallel} = E^2 \left(1 - \sin^2 \frac{\delta}{2}\right) = E^2 \cos^2 \frac{\delta}{2} \tag{2.9}$$

whereas, with perpendicular polarizers, we get:

$$I_{\perp} = E^2 \sin^2 \frac{\delta}{2} \tag{2.10}$$

Therefore, we can measure the phase shift for either of these geometries, or measure both and use:

$$\frac{I_{\perp}}{I_{\parallel}} = \tan^2 \frac{\delta}{2} \tag{2.11}$$

which is the ratio between equations (2.9) and (2.10). Equation (2.11) is solved for δ by Wu [47] *et al.*. It is often more convenient to normalize equation (2.10), $\frac{I_{\perp}}{I_0} = \sin^2 \frac{\delta}{2}$ where $I_0 = E^2$.

Solving (2.10) for δ gives:

$$|\delta| = N\pi + \arcsin I_{\perp}, \quad N = 0, 2, 4 \ldots \tag{2.12}$$

$$|\delta| = N\pi - \arcsin I_{\perp}, \quad N = 1, 3, 5 \ldots . \tag{2.13}$$

An oscillating intensity signal is shown in figure 2.6. The signal goes to 0 at high voltages where the cell becomes homeotropically aligned with $\delta = 0$. Following the trace to lower voltages, it is clear that each turning point corresponds to an addition of π to the value of $|\delta|$, and therefore N in equations (2.12) and (2.13) is equal to to the number of turning points in the CPI data. This can be clearly identified in figure 2.6.

This now allows us to calculate the value of δ when no field is applied to the cell, and the birefringence seen by the incident light is at a maximum. First, the number of turning points in the CPI data are counted, and N in equations (2.12) and (2.13) is set equal to that value. The appropriate equation is then chosen, depending on whether N is odd or even. Finally, the value for $I_{\perp}$ is read from the graph, and inserted into the

equation, resulting in the phase shift. This can be used in equation (2.4) to measure the birefringence of the LC layer.

2.5 The Voltage Transfer Function (VTF)

The VTF is an extension of the CPI measurement described in the previous section. It is used to measure the voltage drop across the LC layer relative to the polymer layers in a cell. The technique has been developed in order to characterize photoactive polymer aligning layers in LCLVs under different illumination conditions, but can be used for any layers with varying electrical properties in a cell such as the electrically commanded alignment surfaces from Komitov [48] or optically addressed surfaces first developed by Aubourg *et al* [49].

The technique and the application to LCLVs will be described in more detail in chapter 4, but a brief introduction will be given here. The fundamental principle is that the electrical Frederiks transition is given by:

$$V_c = \pi \sqrt{\frac{K_1}{\epsilon_o \Delta\epsilon}} \tag{2.14}$$

which is clearly a constant material property for a constant temperature as shown in section 1.4.1. However, it is possible to observe an apparent shift in the Frederiks transition due to a voltage drop across the photoconductive polymer layer in LCLVs, which would lead to an increase in the voltage applied to the whole device in order to switch the LC.

The VTF is a measurement of the intensity through the system shown in figure 2.5 as a function of the amplitude and frequency of an AC voltage. The LC layer can be modelled as a parallel resistor and capacitor, while the polymer layers can be modelled as a capacitor in parallel with a large resistor. Therefore the impedance of the polymer layers is only comparable with that of the LC layer at lower voltages, as the large resistance starts to come in to play. All of this means that there should be a higher voltage drop across the polymer layers when an AC voltage of a sufficiently low frequency is applied to the device, which will be observed as an increase in V_c. To emphasize: this increase

is apparent and not due to any actual change in the Frederiks transition, which occurs at a constant voltage regardless of the frequency. Therefore, the difference between the measured V_c at high frequencies and at lower frequencies will give a value for the voltage dropped across the other layers.

A theory has been developed to explain the behaviour of LCLVs characterised by VTF that models the photoconductive layer and the LC layers as parallel RC circuits, which leads to a filter circuit with a characteristic time constant that is related to the relative conductivities of the photoconductor and the LC. The Frederiks transition can be measured by finding the point at which the intensity changes by more than 2% of the initial value, and can be indicated in the resulting VTF maps (color plots showing the intensity output as a function of the voltage amplitude and frequency). Observing how the aforementioned time constant and the apparent Frederiks transition changes with changing light illumination can help to explain the origin of the photorefractive mechanism in LCLVs, as well as identifying suitable frequencies for the operation of such devices. As an example, at certain frequencies, the Friedericksz transition can appear to have smaller values as the incident light intensity increases. This is indicative of a decrease in the impedance of the photoconductive layer, and the frequency at which this effect occurs should be equal to the frequency at photorefractive modulation takes place.

2.6 Two-beam coupling

This thesis has frequently referenced LCLVs: LC devices where the refractive index is in some way related to the intensity of incident light. Other essentially synonymous terms are optically addressed spatial light modulators (OASLM), and photorefractive devices. In each case, a simple liquid crystal cell is hybridized in some way to couple the orientation of the LC layer to the incident light intensity, generally achieved by placing a photoactive layer in contact with the LC layer, or otherwise doping the LC with a photosensitive material.

For now, the discussion can be restricted to one type of light valve: a transmissive device that utilises a photoconducting layer in contact with the LC, and that is addressed by

an electric field in order to induce the photorefractive effect such as that described by Ashley *et al.* [50]. When going on to describe new materials for LCLVs in chapter 6, other technologies will be described in more detail.

When light is incident upon a photoconductive material such as amorphous silicon, the conductivity of the material changes in accordance with the intensity. Semiconducting materials are insulators, where charges lie very close in energy to the conduction band. Light of a sufficiently high frequency can be absorbed by the material and can cause charges to move into the conduction band of the material, where an applied voltage will stimulate a current. The process is depicted in figure 2.8.

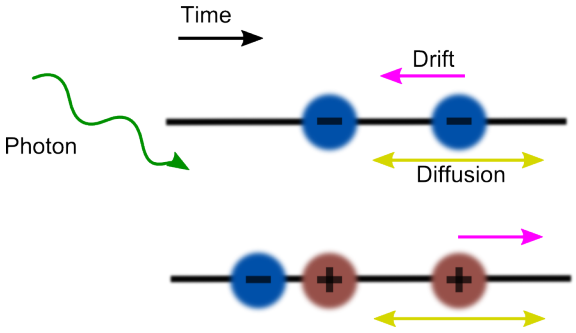

Figure 2.8: Photoconduction in a semiconductor. Light excites electrons from the high potential valence band to the lower energy conduction band, leaving a positively charged hole. The electron-hole pair can then carry a current due to diffusion (based on the charge carrier concentration) or drift (a result of an applied electric field, which can hence only occur in one direction depending on the polarity of said field).

When a voltage is applied to a photoconductor, the voltage drop across it will depend on the light intensity. Furthermore this illumination can be non-uniform, causing the potential drop to be a function of the spatial dimensions of the device. For example an interference pattern, normally incident on a photoconductor, will result in a periodic potential when a voltage is applied perpendicular to the material plane. This is the origin of wave mixing effects in LCLVs.

Any change in the voltage drop across a semiconducting layer will affect the voltage applied to an LC layer in contact with it. This will in turn affect the electric field, hence the LC alignment, and hence the refractive index of the system. Light passing through the system will undergo a phase shift depending on the light intensity in the region under investigation, which describes an OASLM, and a light valve is created when

e.g. a polarizer is added, or wave mixing occurs. The terms will be used somewhat interchangeably throughout this report.

Two-beam coupling (TBC), or wave mixing is an effect that can only be seen as a consequence of photorefractivity. Also known as self-diffraction, it can be used as an effective metric to compare between different photorefractive materials and devices, while also having significant practical uses such as optical circuit elements [51] and coherent light amplification [52].

The process by which light undergoes TBC in an LCLV is described here, and extended in chapter 4 to include a time-dependent addressing field. Two different diffraction regimes, Raman-Nath and Bragg, are explained, as well as the conditions that determine which one will be observed. The experimental set-up is then outlined.

2.6.1 Bragg and Raman-Nath TBC

Before discussing the Bragg and Raman-Nath regimes, it will be useful to qualitatively convince ourselves that beam coupling can occur in photorefractive media such as LCLVs. Beam coupling, as the name suggests, is where energy from one light beam is transferred to another, amplifying one beam while attenuating the other. When two light beams interfere on the surface of an LCLV, there will be a resultant refractive index grating with a wave vector equal to the difference between the wave vectors of the incoming beam. This grating will then diffract light from one beam which will interfere constructively with the other. It is generally necessary to tilt the cell in order to break the symmetry which causes equal energy transfer between the beams, leading to no net effect. This tilt will be taken into account when mathematically modelling the system.

The Raman-Nath regime results in multiple diffracted orders, while only two output beams are observed in the Bragg regime: an observation that helps identify experimentally which regime is under consideration. The two regimes can be distinguished further by a parameter suggested by Kogelnik [53]:

$$q = \frac{2\pi\lambda L}{n_u \Lambda^2}, \tag{2.15}$$

where L is the thickness of the grating, Λ the grating spacing, and n_u the average refractive index across the grating. The Bragg regime is in effect for $q \gg 1$, and the Raman-Nath for $q \ll 1$. In fact, the picture is somewhat more complex as reviewed in [54], and it is certainly clear that there is no distinct cut-off point between the two regimes.

In spite of that, it will be assumed for this discussion that two distinct theories exist for thick and thin gratings. These theories are helpful to understand the underlying mechanisms, and tend to be less complex than theories that seek to describe diffraction for all values of q. This report will only focus on Raman-Nath diffraction, as Bragg diffraction was not used in any of the experiments.

Daly *et al.* [55] have outlined a theory describing coupled wave equations that describe the two interfering beams as they travel through a photorefractive medium. This theory can model the beam coupling response in such systems independently of the regime under consideration, and can be shown to reproduce the existing separate equations that describe Bragg and Raman-Nath diffraction for the corresponding values of q. This theory is particularly useful to describe the response for systems where $q \sim 1$ i.e. the region where neither Bragg or Raman-Nath diffraction can be said to dominate the response. Given that the discussion here will be restricted to Raman-Nath, with $q \ll 1$, it is valid to restrict the discussion to the regime-dependent theory outlined below.

2.6.1.1 Raman-Nath theory

Raman and Nath [56] sought to theoretically describe observed diffractive effects in experiments investigating what would now be described as acousto-optic modulators (AOMs) [57]. In this case, a phase grating is set up in the photorefractive LC cell. This can be treated mathematically by considering a wave passing through a medium and experiencing a spatialy modulated phase shift due to a non-uniform refractive index profile. The mathematical form of the wave after passing through the medium will be shown to be expressible in terms of a series of plane waves, each with different amplitudes and wavevectors.

Let us for now ignore the origin of the grating, and instead start by defining a refractive index profile of the form:

$$n_m(x) = n_0 + \Delta n_m \sin \boldsymbol{K} \cdot \boldsymbol{x} \tag{2.16}$$

where $\mathbf{x}$ lies in the plane of the medium supporting the grating and $\mathbf{K}$ is the wavevector of the grating. n_0 and Δn_m are material constants that define the values n_m can take. An incident plane wave travelling in the (x, z) plane will have an electric field of:

$$E = E_0 \exp i\,(\mathbf{k} \cdot \mathbf{x} - \omega \mathbf{t}). \tag{2.17}$$

Here, ω and $\mathbf{k}$ are the frequency and wavevector of the wave respectively, and E_0 the amplitude.

As the wave travels through the medium, it undergoes an index-dependent phase shift, such that on the furthest face of the medium the transmitted electric field is given by:

$$\begin{aligned} E_t =& E_0 \exp i\,(n_0 \boldsymbol{k} \cdot \boldsymbol{x} - \omega t) \cdot \exp i(\delta \sin \boldsymbol{K} \cdot \boldsymbol{x}) \\ E_t =& \exp \left[i \left(n_0 \boldsymbol{k} \cdot \boldsymbol{x} + \frac{2\pi \Delta n L}{\lambda \cos\theta} \sin n_0 \boldsymbol{K} \cdot \boldsymbol{x} - \omega t \right) \right] \end{aligned} \tag{2.18}$$

where $L = d \cos\theta$ and $\delta = \frac{2\pi \Delta n L}{\lambda \cos\theta}$ i.e. the modulated phase shift. The factor of n_0 that scales $\boldsymbol{K} \cdot \boldsymbol{x}$ is picked up due to the definition $\boldsymbol{K} = \boldsymbol{k_1} - \boldsymbol{k_2}$ where $\boldsymbol{k_1}$ and $\boldsymbol{k_2}$ are the wavevectors of the interfering beams *outside* of the medium: a factor of n_0 must be added when considering interference inside the medium.

We can re-write equation (2.18) using the Jacobi-Anger identity for the Bessel functions [18]:

$$e^{i\delta \sin x} = \sum_{m=-\infty}^{\infty} J_m(\delta) e^{imx}, \tag{2.19}$$

which allows us to treat E_t as a sum of plane waves:

$$E_t = E_0 \sum_{m=-\infty}^{\infty} J_m(\delta) \exp i\,[n_0(\boldsymbol{k} + m\boldsymbol{K}) \cdot \boldsymbol{x} - \omega t] \tag{2.20}$$

each of which will propagate with wave vector $\boldsymbol{k} + m\boldsymbol{K}$ at an angle given by:

$$\arccos\left(\frac{\boldsymbol{k}\cdot(\boldsymbol{k}+m\boldsymbol{K})}{|\boldsymbol{k}||\boldsymbol{k}+m\boldsymbol{K}|}\right) \tag{2.21}$$

The intensity of each order as a function of the grating thickness L ($I/I_0 = J_m^2(\delta)$) is shown in figure 2.9 for the first three orders. For thicker gratings there is no highest intensity order, and therefore the thickness of the grating is extremely important when considering the strength of the non-linear response of this kind of system.

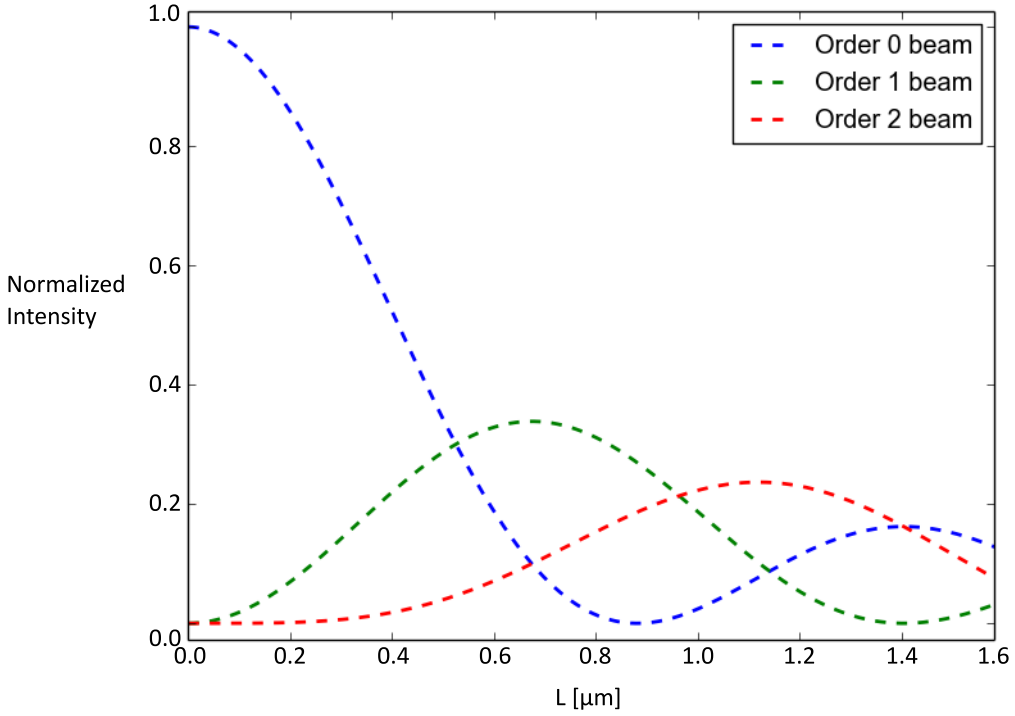

Figure 2.9: Theoretical plots of the intensity of diffracted orders in the Raman-Nath regime. The Bessel functions have been calculated using an inbuilt function in the python module scipy.

The beam coupling itself can be seen as the superposition of these orders. We will first consider the simple case shown on the left hand side of figure 2.10. Using the labels shown in the figure, the angle of the first diffracted order from the beam $\boldsymbol{k_2}$ is given by:

$$\xi = \arccos\left(\frac{\boldsymbol{k_2}\cdot(\boldsymbol{k_2}+\boldsymbol{k_g})}{|\boldsymbol{k_2}||\boldsymbol{k_2}+\boldsymbol{k_g}|}\right). \tag{2.22}$$

The dot product in the numerator can be expanded to give $k_2^2 + \boldsymbol{k_2}\cdot\boldsymbol{k_g}$, and in turn

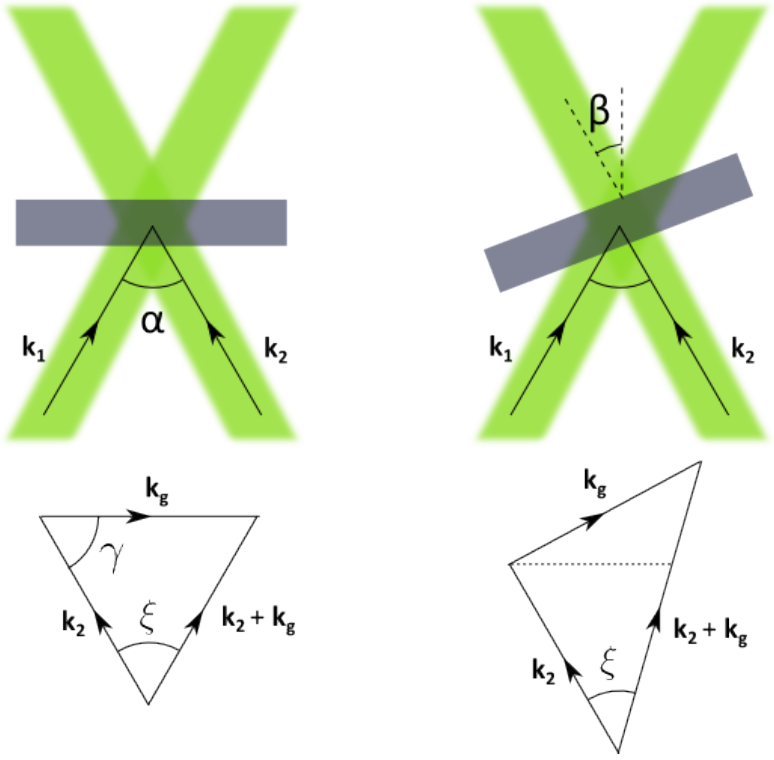

Figure 2.10: Two geometries considered in order to show that Raman-Nath conditions lead to energy exchange between beams.

the dot product $\boldsymbol{k_2} \cdot \boldsymbol{k_2} = k_2 k_g \cos\gamma$. This can be further simplified due to the fact that $\gamma = \pi/2 - \alpha/2$, and we can rewrite equation (2.22):

$$\xi = \arccos\left(\frac{k_2^2 - k_2 k_g \sin\alpha/2}{|\boldsymbol{k_2}||\boldsymbol{k_2} + \boldsymbol{k_g}|}\right). \tag{2.23}$$

The magnitude of the vector sum of $\boldsymbol{k_2} + \boldsymbol{k_g}$ can be found using the cosine rule to be:

$$\sqrt{k_2^2 + k_g^2 - 2k_2 k_g \sin\alpha/2}, \tag{2.24}$$

and the expression for the grating spacing is:

$$\Lambda = \frac{\lambda}{2\sin(\alpha/2)\cos\beta}, \tag{2.25}$$

where β is the angle between the cell normal and the bisector of the two beams - 0 in this case - which in turn yields the expression:

$$k_g = 2k_2 \sin(\alpha/2). \tag{2.26}$$

Inserting equations (2.24) and (2.26) into the expression for θ in equation (2.23) gives:

$$\xi = \arccos\left(\frac{1 - 2\sin^2 \alpha/2}{\sqrt{1 + 4\sin^2 \alpha/2 - 4\sin^2 \alpha/2}}\right). \tag{2.27}$$

The denominator of this fraction equals 1, and the remaining expression:

$$\cos\xi = 1 - 2\sin^2\frac{\alpha}{2} \tag{2.28}$$

is the double angle formula, which proves that $\xi = \alpha$, and therefore that the first diffracted order from one beam propagates along the same path as the other, coupling energy between the beams.

While this is enough to show that energy exchange is possible in this system, the actual net effect would not be observable for this case due to symmetry considerations; effectively, energy is coupled from beam 1 to beam 2 at the same rate as energy is coupled from beam 2 to beam 1, so neither beam will be more energetic. In this analysis pretilt was not considered, so some small beam coupling can in fact be observed [58], but it is more interesting and useful to introduce an asymmetry by tilting the cell as shown in the right-hand section of figure 2.10. In this case, it is possible to asymmetrically couple energy between the beams, the result of which is one beam gaining energy at the expense of the other: the conditions for two-beam coupling.

2.6.2 Experimental measurements of two-beam coupling

Two-beam coupling measurements are performed using a setup shown in figure 2.11.

The grating angle Λ can be adjusted by varying the tilt angle or by adjusting the bisector angle of the two beams, although the tilt angle is generally kept constant, as 30° has been found to give the highest beam-coupling efficiency. The bisector angle can be modified by changing the distance between the beamsplitter and the cell, and adjusting the mirror to align both writing beams on the surface. A camera can be used in place of the cell to verify that the beams are interfering at the correct position.

The beam-coupling efficiency is generally defined as:

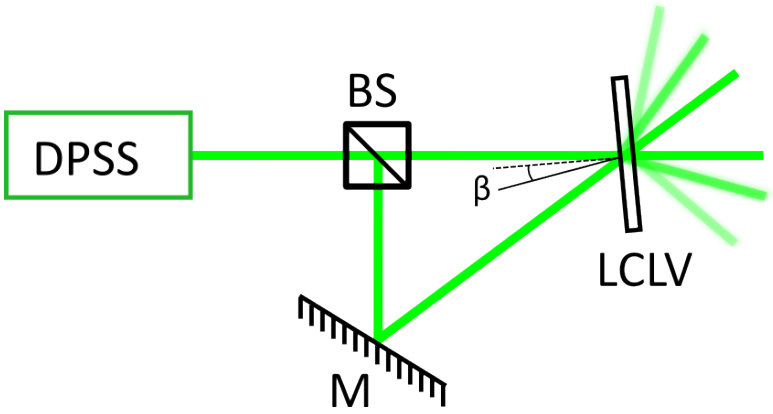

Figure 2.11: Experimental setup used to measure the two-beam coupling efficiency of photorefractive LC cells. A diode pumped solid state (DPSS) laser is often used as an intensity source. The label M refers to a mirror, and BS refers to a beamsplitter. LCLV stands for liquid crystal light valve, and it is shown tilted, with the angle between the bisector of the two writing beams (solid line) and the normal to the cell (dashed lines) denoted β.

$$\Gamma = \frac{1}{l} \ln\left(\frac{Gm}{m - G + 1}\right), \tag{2.29}$$

where l is the interaction length, m is the ratio of the intensities of the two writing beams, and G is the intensity of one beam in the presence of the other, divided by the intensity of the same beam in the absence of the other [59]. When comparing between different photorefractive LC systems, it is generally sufficient to investigate the intensity of the higher order beams and use this as a measure of the intensity [2].

2.7 Diffraction efficiency

The diffraction efficiency, i.e. how efficiently energy from a probe beam can be transferred to diffracted orders, is an alternative scheme to TBC that will still result in a reliable characterization of the strength of the photorefractive response. The experimental setup is shown in figure 2.12

Two high energy writing beams are incident on the cell, which in this case is set such that the bisector of the two beams lies parallel with the normal to the cell surface. These writing beams induce a phase grating, which can be probed using a weaker beam of a different wavelength, given that this beam will not interfere with the writing beams.

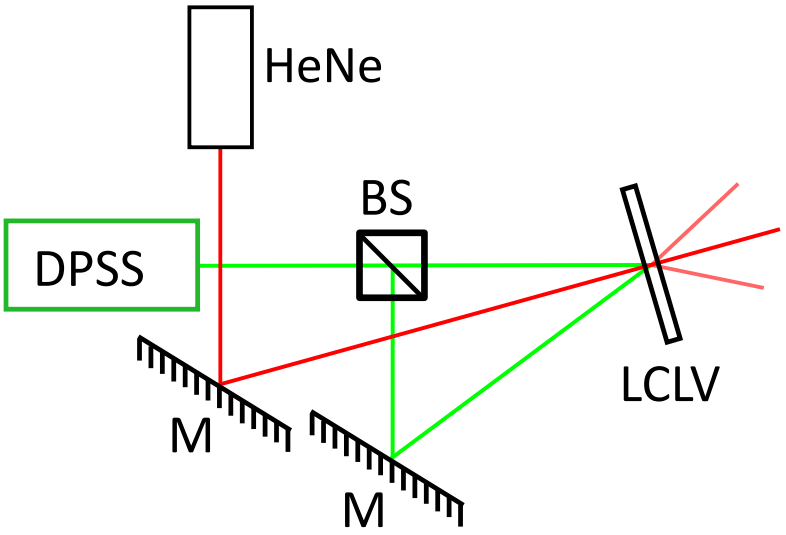

Figure 2.12: Experimental setup used to measure the diffraction efficiency of photorefractive LC cells using the same labels from figure 2.11. In this case, a red probe beam from a helium neon laser (HeNe) is shown.

The diffraction efficiency is defined as:

$$\eta = \frac{I_1}{I_0} \tag{2.30}$$

where $I_{0,1}$ are the intensities of the fundamental and first order diffracted beams respectively. One needs to be careful with this definition to ensure that it takes into account reflection losses e.g.

The theoretical treatment of this system tends to assume that the writing beams will create a sinusoidal grating, and can be derived from studies of acousto-optic modulators [60].

The diffraction efficiency in the Raman-Nath regime is given by [61]:

$$\eta = J_m^2 2\kappa d \,\mathrm{sinc}\left(\frac{Qa}{2}\right), \tag{2.31}$$

where J_m is the mth order Bessel function, d is the distance into the cell the modulation propagates, and the other variables are defined as:

$$\kappa = \pi \frac{\Delta n_m}{\lambda_0}$$

$$Q = \frac{2\pi\lambda_0 d}{n_0 \Lambda^2}$$

$$a = \frac{-n_0 \sin\theta}{K}.$$

Δn_m is a material constant that scales the refractive index modulation, λ_0 is the wavelength of the probe beam, Λ is the grating spacing, n_0 the average refractive index, and K is the grating vector $2\pi/\Lambda$. Most of these definitions and equations are identical to those used in the previous TBC section 2.6, where the theory is extremely similar. The factors that have to be taken into account when optimizing TBC response are the same as those necessary to optimize the diffraction efficiency in the system.

2.8 Conclusions

This chapter has described several measurement and characterization techniques that have been used in the investigations reported on in this thesis. Each of the measurement techniques gives a piece of data relating to either an LC material, or an LC device.

The thickness of a simple LC cell is an important parameter, as it affects the phase shift experienced by light passing through a filled cell. It can be measured using a spectroscopic technique. The clearing point of an LC material can be measured with a microscope and heat stage, and is used in chapter 5 to determine the clearing point of LC/nanoparticle colloids.

The dielectric anisotropy of an LC determines the Fredericks transition, and as such is extremely important when considering electrical efficiency. It can be measured using a capacitance bridge.

Measuring the voltage-dependent intensity of light passing through an LC cell placed between crossed polarisers allows an accurate calculation of the phase shift of light passing through the cell. This chapter has shown how this measurement can be used to

determine the maximum phase shift that light experiences passing through a planar cell, and how this phase shift can be used to calculate the birefringence of the LC material.

The voltage transfer function, two-beam coupling and diffraction efficiency measurements have been used to characterise the strength of photorefractive modulation in hybrid LC cells, described in more detail in chapters 4 and 6. The VTF measures the relative voltage drop across the constituent layers of an LC device, while the TBC and diffraction efficiency experiments are both effective ways of determining a figure-of-merit for the strength the photorefractive modulation in hybrid LC devices, and can therefore help when comparing different photorefractive systems for industrial applications.

The techniques used to describe the errors associated with these techniques are described in detail in appendix A. The specific associated uncertainties are calculated when these techniques are used throughout this thesis.

The techniques described in this chapter are all reliable, accurate, and give repeatable data sets when applied to LC cells. The following chapters describe work where these standard techniques have been employed, and in some cases modified as required.

Chapter 3

New optical probe measurement of nematic time response

This chapter describes a newly developed experimental technique that uses an optical probe to determine two viscosity coefficients of nematic LCs; anisotropic liquids require multiple coefficients to fully describe the viscosity thanks to the relative positions and orientation of the mesogens with respect to the flow. The rotational viscosity, γ_1, is one of the coefficients that can be measured using this technique. This parameter can then be used to calculate the rise and fall time of the LC, and hence how quickly a device will respond to an applied field. Both the rise and fall times are dependent on the thickness of the cell and the rise time is also voltage dependent [24], and therefore γ_1 can be used to compare the time response of different LC materials - typical values range from 10-300 mPa·s.

This chapter will begin with an overview of Erickson-Leslie theory - a continuum theory to describe flow in nematics. This theory leads to constitutive equations, which can be used to model the director in a cell under the application of any generic field. The next section shows how the behaviour predicted by these equations can be verified using a CPI experiment with a carefully controlled voltage signal, and how fitting to these data can be performed using viscosity coefficients as fitting parameters. Finally, the application of this method to three different nematic materials is described, and the resulting parameters compared to the literature.

3.1 The importance of time response for LC devices

The time response as a measure of how quickly an LC responds to an applied field is of the utmost importance when considering new materials for applications. It is one of the key factors when choosing a material for use in an LCD, and is no less important for other LC devices such as lenses or projection light modulators. The reasons for this are fairly clear; a high value for time response will limit how quickly the LC can be switched on or off and therefore prevent how quickly the device can be updated. This is of interest for the light valves discussed in chapter 6 as well, because the optical networks, sensing applications and safety equipment that would make use of such devices all rely on being able to respond to a change in the input intensity as quickly as possible.

3.2 Erickson-Leslie theory

Erickson-Leslie theory aims to adapt the continuum theory of isotropic fluids to a theory that can describe nematic LCs. Erickson was the first to put forward results that could describe the dynamics of nematics, and his work was later extended by Leslie in 1969 [62]. In 1992, Leslie formulated a version of the dynamic theory for incompressible and isothermal fluids, which is not only much simpler, but also involves the use of familiar and physically meaningful parameters such as the rate of strain tensor: a quantity that appears in earlier continuum theory. The derivation of the theory is not included here in full, but a complete description can be found in a book by Ian Stewart [24]. The method is discussed qualitatively in this section, and the resultant equations which govern nematic flow are given in section 3.5.

In order to derive equations for the fluid flow of a nematic, it is first necessary to define quantities that describe the kinematics of the nematic, i.e. quantities that describe the motion of the fluid without any assumptions about how this motion might come about. Examples include the velocity of the fluid, the angular velocity of the director and the angular velocity of the fluid at any point in the volume of the LC, as well as two tensors which appear in classical continuum theory: the rate-of-strain and vorticity tensors.

These quantities can then be used in laws for the conservation of mass and linear/angular momentum, and it is at this point that the incompressibility and hence the constant value for the density of the fluid can be assumed. Finally, Leslie assumed a rate of work hypothesis, which states that any work done on the nematic by external forces will be absorbed into the nematic free energy, the kinetic energy of the fluid or will be dissipated back out of the system via the viscosity opposing the flow. Finally, this is all brought together to form constitutive equations which describe the flow of the fluid using 6 coefficients, α_{1-6} which are known as the Leslie coefficients.

3.2.1 The Leslie coefficients

The nematic viscosities denoted by the six Leslie coefficients will be discussed briefly here, as it is somewhat difficult to ascribe any physical meaning to the viscosities by themselves. When considering the time response of an LC, it is the rotational viscosity rather than a value of α_i that is used, and hence some link must be made between the Leslie coefficients and γ_1.

Humphrey Miesowicz proposed three physically intuitive viscosity coefficients, $\eta_{1,2,3}$, for fluid flow around the director with three orthogonal orientations as depicted in figure 3.1 [63, 64]. The effective viscosity for any orientation can be written as a linear combination of these three viscosities, as well as a fourth, η_{12} which cannot easily be visualised. These viscosities do not exist in isotropic fluids.

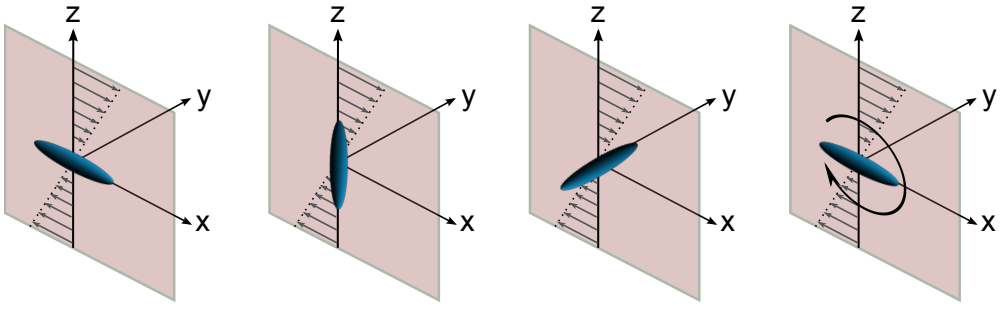

Figure 3.1: Each panel depicts shear flow in a nematic in the (x,z) plane, and the possible orientations of the LC director. From left to right, the viscosities shown are η_1 where the flow is parallel to $\hat{\boldsymbol{n}}$, η_2 where the grad of the flow is parallel to $\hat{\boldsymbol{n}}$, and η_3 where $\hat{\boldsymbol{n}}$ is perpendicular to both the flow and the grad of the flow. Also shown in the rightmost image is the director rotating and experiencing a viscous torque, an effect characterized by the rotational viscosity γ_1

By inserting expressions for the geometry of the director and shear flow velocity into the aforementioned rate-of-strain and vorticity tensors, one can show that the Miesowicz viscosities are given by linear combinations of the Leslie coefficients:

$$\begin{aligned} \eta_1 &= \frac{1}{2}(\alpha_2 + 2\alpha_3 + \alpha_4 + \alpha_5), \\ \eta_2 &= \frac{1}{2}(-\alpha_2 + \alpha_4 + \alpha_5), \\ \eta_3 &= \frac{1}{2}\alpha_4, \\ \eta_{12} &= \alpha_1, \end{aligned} \tag{3.1}$$

where use has been made of the so-called Parodi relation: $\alpha_6 - \alpha_5 = \alpha_2 + \alpha_3$ [65]. This reduces the number of independent coefficients to five, with α_6 generally being replaced appropriately.

γ_1, the rotational viscosity is also depicted in figure 3.1 as the torque associated with a rotation of the director. There is one other viscosity, denoted by γ_2 and known as the torsion coefficient, which quantifies the contribution to the torque due to gradients in the shear flow velocity. Both of these coefficients actually appear in the constitutive equations for the Erickson-Leslie theory in order to simplify the linear combinations of the Leslie coefficients, which are:

$$\begin{aligned} \gamma_1 &= \alpha_3 - \alpha_2, \\ \gamma_2 &= \alpha_3 + \alpha_2. \end{aligned} \tag{3.2}$$

It should be noted that, for calamitic LCs, it is generally valid to assume that $\gamma_1 = -\gamma_2$, which in turn allows us to neglect α_3 [66].

3.3 Fast oscillation of nematic liquid crystal director under an AC field

When an AC field of sufficiently high frequency is applied to an LC cell, the director is generally assumed only to respond to the RMS of the field as the switching time

(typically between 1-100 ms) is too high to follow any change in the amplitude. On the other hand, at lower frequencies the director will follow the modulus of the field with some phase lag, as the time period is sufficiently long for the LC to reorientate before the field completes an oscillation. The switch between the regimes where the LC follows the field, and where the LC responds to the RMS of the field occurs at a frequency determined by the time response of the LC as discussed in the VTF half of chapter 4, and typically occurs at 10 Hz.

However, this simple generalization does not, in fact, hold true. At certain frequencies it is possible to observe a mixture of the two behaviours, wherein the LC director responds to the RMS of the field, and at the same time undergoes small oscillations at twice the frequency of the field. The amplitude of these oscillations will, for any given frequency, depend on the applied voltage and the viscosity of the LC sample, and the measurement of such should allow a calculation of the viscosity of the LC.

3.4 Measuring director oscillations

The fast oscillations of the director will affect the intensity of light passing through crossed polarizers in the experiment described in section 2.4 of chapter 2, which is depicted in figure 2.5. Effectively, one should be able to observe small oscillations in the intensity of the signal when applying a single voltage of a sufficiently low frequency to the cell. With reference to the graph shown in figure 3.2, it is clear that the amplitude of these oscillations can vary with increasing voltage, and will be zero around a turning point in the CPI.

The director oscillations can be measured by applying an AC field with a fixed frequency and amplitude to the cell, and measuring the intensity of the output signal from a CPI experiment as a function of time. The resultant time trace can be used to calculate the magnitude of the director oscillations by measuring the range, or standard deviation of the signal - the standard deviation was chosen in this case as it is inherently less susceptible to noise that can distort the maximum and minimum values for intensity.

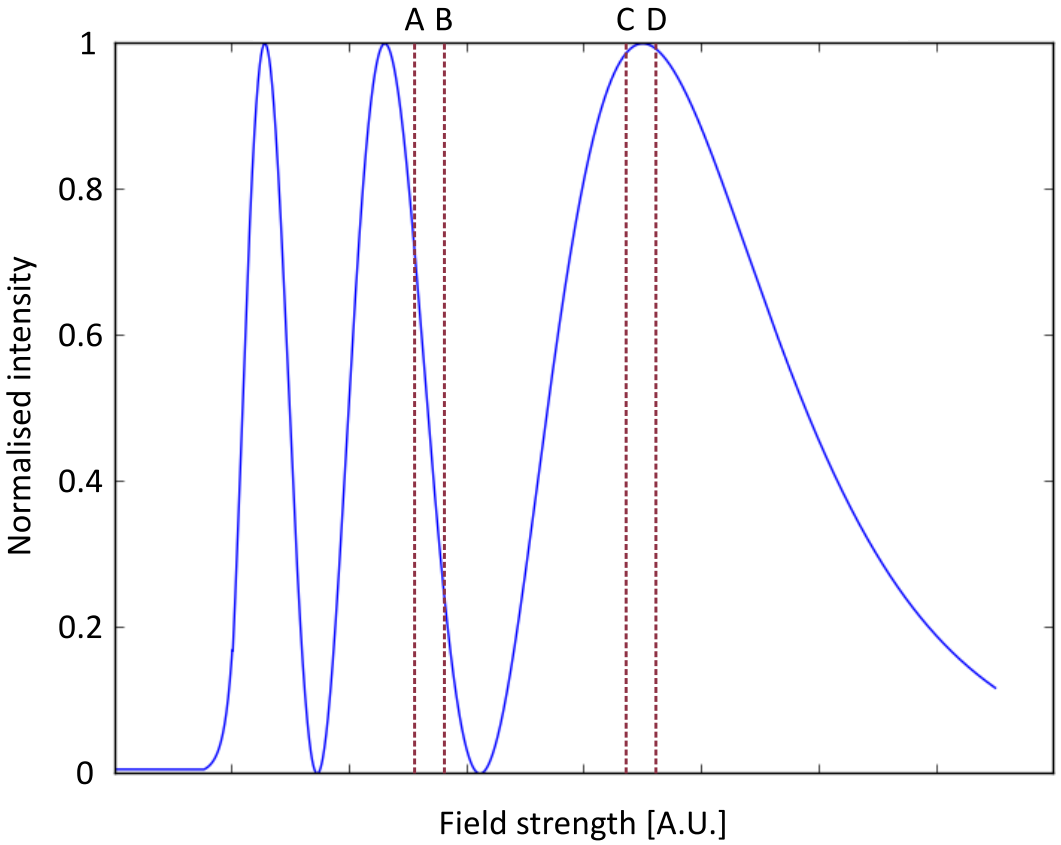

Figure 3.2: An example trace for the CPI as a function of voltage amplitude, proving that the fast oscillations will vary depending on where along this trace one is looking. The amplitude of the field oscillation between A and B is identical to that between C and D, but the intensity variation is practically 0 between C and D.

The magnitude of these oscillations will depend on the viscosities of the LC, which have been introduced. Therefore, it should be possible to extract the viscosities and calculate the time response by developing a model from Erickson-Leslie theory, and fitting to the experimental data, which were obtained using the following experiments.

3.5 Governing equations and the physical consequences

This section introduces the governing equations that result from the Erickson-Leslie treatment of flow in nematics, and how these equations can predict the output of the experiment depicted in figure 3.2.

Using the dimensions indicated in figure 2.5 (the cell wall lies in the (x,y) plane with the initial director lying along x, and light propagates along z), the director can be

parameterized by an angle θ which $\hat{\boldsymbol{n}}$ makes with the x axis, an angle which is a function of z for a planar geometry, $\hat{\boldsymbol{n}} = [\cos(\theta), 0, \sin(\theta)]$. The fluid velocity in this case will be given by $\boldsymbol{v} = [v, 0, 0]$. The two governing equations that are derived from the Erickson-Leslie theory described in section 3.2 are non-linear coupled partial differential equations, given as:

$$\begin{aligned}[K_1 \cos^2(\theta) + K_3 \sin^2(\theta)]\frac{\partial^2\theta}{\partial z^2} + \frac{K_3 - K_1}{2}\left(\frac{\partial\theta}{\partial z}\right)^2 \sin(2\theta) \\ + \frac{\Delta\epsilon\epsilon_0}{2}\left(\frac{\partial\phi(z,t;\omega)}{\partial z}\right)^2 \sin(2\theta) - m(\theta)\frac{\partial v}{\partial z} = \frac{\partial\theta}{\partial t},\end{aligned} \tag{3.3}$$

$$\frac{\partial}{\partial z}\left[g(\theta)\frac{\partial v}{\partial z} + m(\theta)\frac{\partial\theta}{\partial t}\right] = 0, \tag{3.4}$$

with

$$m(\theta) = \frac{1}{2}\left((\alpha_3 - \alpha_2) + (\alpha_3 + \alpha_2)\cos(2\theta)\right), \tag{3.5}$$

and

$$\begin{aligned}g(\theta) =& \frac{1}{2}(\alpha_3 + \alpha_2)\cos(2\theta) - \frac{\alpha_1}{8}\cos(4\theta) \\ &+ \frac{1}{2}(\alpha_3 + \alpha_4 + \alpha_5 + \alpha_1/4),\end{aligned} \tag{3.6}$$

with the electric potential profile given by:

$$\phi(z,t;\omega) = \int_0^z \frac{V(t;\omega)}{1 + \frac{\epsilon_a}{\epsilon_\perp}\sin^2(\theta)}dz' \left(\int_0^1 \frac{1}{1 + \frac{\epsilon_a}{\epsilon_\perp}\sin^2(\theta)}dz''\right)^{-1}. \tag{3.7}$$

In these equations, t is time, and ω is the frequency of the applied field. α_i, v and θ are the Leslie coefficients, fluid flow velocity and angle the firector makes with the x-axis respectively - these terms were described in detail above. In addition, $K_{1,3}$ are the splay and bend elastic constants, $\Delta\epsilon$ is the dielectric anisortopy, and ϵ_0 is the susceptibility of free space; terms which are introduced in chapter 1.

The number of Leslie coefficients that appear in equations (3.5) and (3.6) can be reduced by realizing that both α_1 and α_3 are very small for calamitic LCs such as those under

investigation here, a consequence of the equivalence of γ_1 and γ_2 as discussed by Martinoty *et al.* [66]. Therefore, there remain two linear combinations of Leslie coefficients that can be used as fitting parameters for the LC director response to a given field, namely α_2 (which is equal to γ_1 for small values of α_3) and $\alpha_4 + \alpha_5$.

The first experiment proposed to measure these two parameters involved ramping up the amplitude of an applied AC voltage with a frequency of 500 Hz. The averages of the data could be used to fit the elastic constants that appear in equations (3.3) and (3.4), while high-resolution measurements of the small, fast oscillations of the director could be modelled using these equations. Unfortunately, it was found that there was some coupling between γ_1 and $\alpha_4 + \alpha_5$.

The coupling can be seen in the forcing term $g(\theta)$ in equation (3.6), which includes $\alpha_4 + \alpha_5$, and $\alpha_2 \sim -\gamma_1$. A good and well-constrained fit could be obtained, but an equally good fit could be found by varying both of the variables simultaneously: a single value for $g(\theta)$ can be acquired for multiple values of γ_1 and $\alpha_4 + \alpha_5$. This is shown in terms of the physical effect of changing the parameters on the magnitude of the director oscillations in figure 3.3. The graph shows that a change in γ_1 can be compensated by a change in $\alpha_4 + \alpha_5$, where a change in the magnitude of the oscillations in the centre of the cell is balanced by an opposing change at the edges.

Consequently, it is necessary to determine the effect that γ_1 and $\alpha_4 + \alpha_5$ have on the behaviour of the cell in order to design experiments that can measure them independently. γ_1 is an intuitive constant that determines the time scale over which the director of an LC can reorientate, while the effect of $\alpha_4 + \alpha_5$ on the switching behaviour is somewhat less obvious. Put simply, $\alpha_4 + \alpha_5$ determines the transfer of energy between the director oscillations and the flow, and larger values will reduce the induced flow.

Therefore, finding a form of the voltage for which fluid flow is completely uncoupled from the director oscillations would allow an independent measurement of γ_1. Turning to equations (3.3) and (3.4), it is clear that the forcing term $m(\theta)$ is responsible for the coupling between the fluid flow dv/dz and the director oscillations $d\theta/dt$, and if $m(\theta)$ were to equal 0, there should be no coupling between the two and hence $\alpha_4 + \alpha_5$ will have no effect on the behaviour of the system. Experimentally, $m(\theta) = 0$ can be achieved

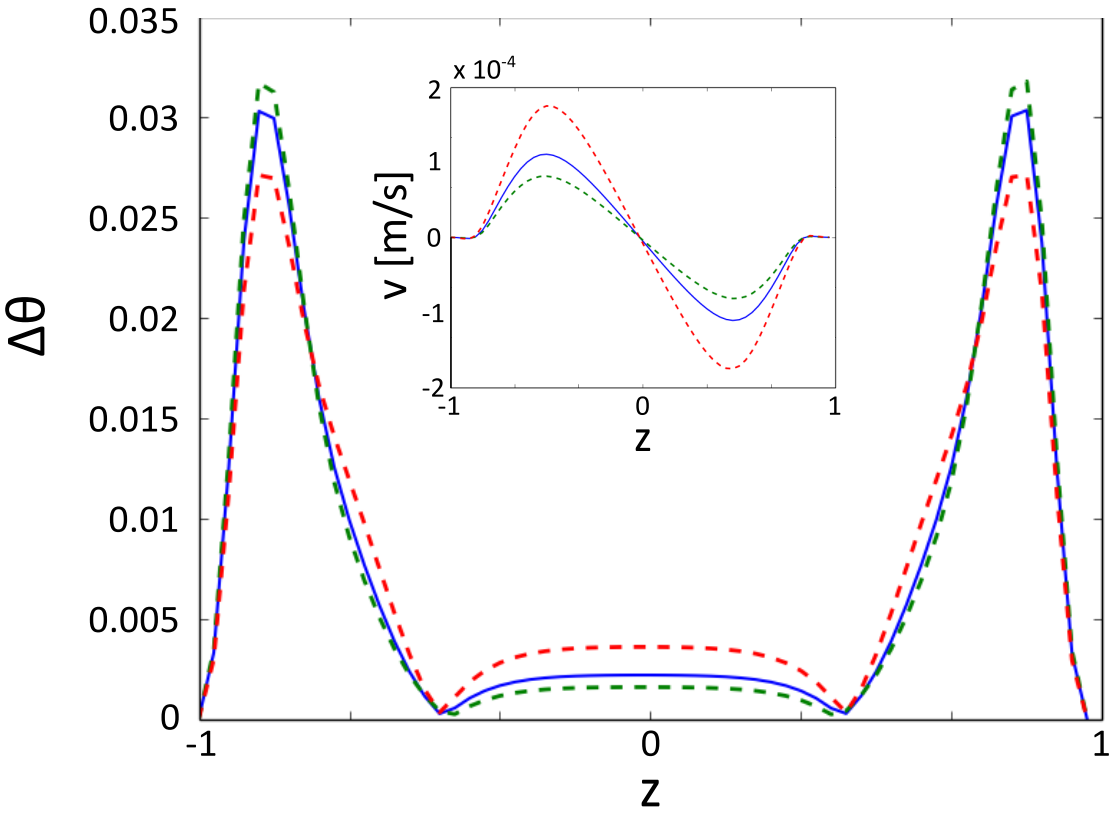

Figure 3.3: Figures showing the theoretical effect of varying γ_1 on the director oscillations and flow velocity (inset) as a function of distance into the cell. The blue line is for $\gamma_1 = 203.6$ mPas and $\alpha_4 + \alpha_5 = 431$ mPas. The red and green dashed lines show the effect of changing γ_1 by ± 10 mPas respectively, and in each case $\alpha_4 + \alpha_5$ can be modified to obtain the same value for the standard deviation of the intensity oscillations. An increase in γ_1 (red line) can be compensated by a change in $\alpha_4 + \alpha_5$, at which point the higher oscillations at the centre of the cell can be compensated by the lower oscillations at the edges.

by choosing a voltage close to the Frederiks transition, where θ and hence the $\cos(2\theta)$ term in equation (3.5) is close to zero, again assuming that α_3 is small in the case of calamitics.

The magnitude of the director oscillations is very small at these low voltages, so instead a modulated voltage with a high-frequency carrier signal, that varies slowly between two working points can be used. The frequency of this modulation can be slow in order to maximize the measured signal, and then varied so as to be modelled by Erickson-Leslie theory. In addition the working points can be chosen with large signals in mind, as described in section 3.6. Once a value for γ_1 has been determined, it can be used in the originally proposed experiment to obtain a value for $\alpha_4 + \alpha_5$.

3.6 Experimental determinations of the viscosities

In order to measure the viscosity, three cells were prepared with PI alignment layers at both boundaries. PI (Pyralin PI 2525 from HD microsystems) was dissolved into a solution of 1-methyl-2-pyrrolidinone at a concentration of 1:10 by volume. ITO-coated glass slides with an area of 3 cm^2 were cleaned using acetone and lab tissue, dusted using compressed air and mounted onto a spin coater. 400 μl of the PI solution was dropped onto the surface, and then spin-coated at 500 rpm for 6 s, followed by 4000 rpm for 30 s. The PI was then annealed at 200°C, and rubbed using a rotating velvet cloth.

The thickness of the cells was controlled by using UV glue mixed with spacer beads to secure the slides together, and each was filled with a different LC material: E7, TL205, and ZLI4792 before being encapsulated with Araldite. The LC materials were chosen for their availability, but they also demonstrate a wide range of birefringences and time constants, as well as having a large number of reported measurements of the nematic viscosities (although it should be noted that viscosities are extremely temperature dependent, and as such comparisons can be made difficult depending on the depth of detail of the reports). The cells had a variety of thicknesses to test the applicability of this method to a wide-range of different cell parameters. The cells were all prepared in the standard way using PI as the aligning layer for both substrates.

The first experiment was to ramp up the amplitude of a 10 kHz voltage signal, and measure the resultant average intensity signal. The data were modelled using $K_{1,3}$, the pre-tilt, and the cell thickness as fitting parameters, a method that is described - along with all of the fitting procedures - in section 3.7. The resultant intensity time trace was used to determine the working points described in the previous section; the first full rise or fall between 0 and 1 of the normalised intensity values was identified, and the voltages that resulted in a change of between 0.1 and 0.9 were chosen as initial working points. These working points were used in equations (3.3) and (3.4) via equation (3.7), and the effect of changing $\alpha_4+\alpha_5$ was examined: no effect would indicate that the working points are usable, whereas some residual coupling would require one to go back and choose a second working point closer to the Frederiks transition. Once these working points were

chosen, an amplitude modulated (AM) signal of the form:

$$V(t) = \frac{V_0}{2}[1 + A\cos(\omega_m)]\cos(\omega_c) \tag{3.8}$$

was applied, where V_0 and A could be chosen to give a signal oscillating between the two working points. ω_c is the carrier signal, which again was set to 10 kHz, while ω_m is the modulation frequency that was varied in order to obtain a data set that could be modelled accurately: a sweep between 0.1 and 10.1 Hz with a resolution of 0.5 Hz was found to be sufficient for this experiment.

Each voltage signal in the sweep was applied to the cell. The intensity was measured using a ThorLabs PDA25K photodiode, which converts the intensity to a voltage. This voltage was then measured using a Tektronix TDS220 oscilloscope. This allowed an observation of transient effects, where the time-dependent intensity signal is not a periodic sinusoid - these transient effects can be due to noise in the voltage signal after sending the command to change the voltage, or due to the fact that the director cannot respond to the change in voltage infinitely quickly.

Once the intensity from the CPI experiment was observed to be following a sinusoid with no transient effects, the intensity as a function of time was extracted from the oscilloscope. Ten time periods were measured for each frequency, and the standard deviation of the oscillations was measured for each value of ω_m.

Once the fit had yielded a value for γ_1, a final experiment could be used to determine a value for $\alpha_4 + \alpha_5$, which consisted of sweeping the amplitude of a 500 Hz signal and measuring the time trace of the intensity for approximately ten time periods (0.2 s) with a sampling rate of 250,000 samples per second. The average of these traces could be extracted to verify the LC parameters fit to the 10 kHz trace, but the measurement of $\alpha_4 + \alpha_5$ required a plot of the standard deviation of the time traces as a function of the applied voltage amplitude. The signal is typically extremely small, and the measurement precision as well as the careful control of noise was of significant importance when performing the experiment.

The laser used for probing the cell was a diode pumped, solid-state (DPSS) laser, with a variable ND filter wheel used to tune the intensity incident on the cell under investigation. The intensity needed to be carefully tuned along with the amplification of the photodiode in order to obtain a signal which was not so high that either the photodiode or analogue input of the data acquisition card used were bleached, but not so low as to make the small oscillatory signal impossible to read. The relatively high 16-bit resolution of the NI6211 card used was essential to resolve the signal properly. The laser had to be properly coupled to a heat reservoir in order to keep the temperature constant, and was left to warm up for 20 minutes before starting the measurement - a time that was verified to result in a constant signal based on previous characterization. All of the optics required were kept free of dust, and any other light sources in the lab were extinguished over the course of the experiment.

Having obtained these experimental data, the fitting could proceed. The fitting and data analysis was performed by Tom Bennett, a PhD student working in the School of Mathematical Sciences at the University of Southampton.

3.7 Fitting to the fast oscillations

The crossed polarized intensity can be found for a given form of θ using the following equation:

$$I(t) = \sin^2\left(\frac{\pi d}{2\lambda}\int_{-1}^{+1}[n_o - n_{\text{eff}}]dz\right) \tag{3.9}$$

where $\theta = f(z,t)$, $n_{\text{eff}} = f(\theta)$, and n_{eff} is given by equation (1.22) in chapter 1 as reproduced here:

$$n_{\text{eff}}(\theta) = \frac{n_e n_o}{\sqrt{n_e^2\cos^2\theta + n_o^2\sin^2\theta}}. \tag{3.10}$$

The integral in equation (3.9) can be evaluated using a Clencourt quadrature method, and the average and standard deviation of the intensity for a given time-varying voltage can therefore be extracted and compared directly to the experimental data acquired as per section 3.6. The next step in the process was to fit the experimental data by varying a choice of free parameters present in the constitutive equations.

The first step in the fitting procedure is to take the average of θ over a given time period, and compare it to the average of the experimental data. A reasonable value for the pre-tilt of 2° is chosen and used along with the total phase shift to measure the thickness of the cell (the birefringence and wavelength are known constants in this case). This value for the thickness, d, is used to fit the splay elastic constant K_1 to the Frederiks transition. After this the thickness and pre-tilt are fixed, and the rest of the data modelled to a given value of the elastic constants K_1 and K_3. Finally, the square of the deviation between theory and experiment is calculated, and the entire process repeated using new values for K_1 and K_3 in order to reduce this parameter. When the deviation is tolerably small the process is stopped, and the values for the fitting parameters fixed.

The next step is to find values for $\theta(z,t)$ that satisfy equations (3.3) and (3.4). This was done by first solving the equations in time, t, using a spectral collocation method, followed by a variable-step algorithm to integrate over space, ζ. The result is a series of values for $\theta(\zeta,t)$ at any given value of voltage, which can be used to calculate the crossed polarized intensity via equation (3.9). Again, the modelled values could be compared to measured values, the fitting parameter adjusted, and the process repeated to obtain a good fit. Any form of the potential could be used in equation (3.7), and this procedure can therefore be used for the determination of γ_1 at low voltages, as well as for the determination of $\alpha_4 + \alpha_5$. The obtained values can be checked against the literature values of the same parameters as described in the following results section, 3.8.

3.8 Results of viscosity measurements

The results of the viscosity measurements and the resultant fits will be presented in this section.

Firstly, a low-voltage signal was applied to the three cells in order to measure γ_1. The results of varying the modulation frequency are shown in figure 3.4.

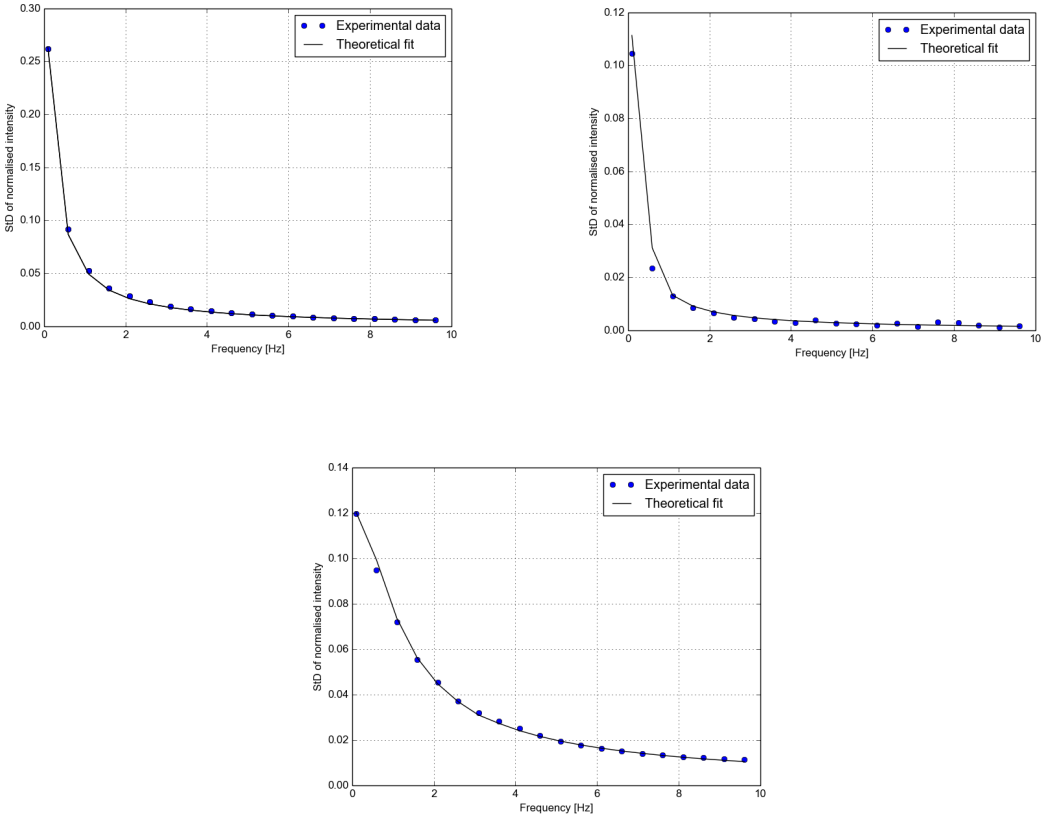

Figure 3.4: Low-frequency measurement of the standard deviation of the intensity signal as a function of applied voltage frequency. Moving clockwise from the top left figure, the LCs measured are E7, TL205 and ZLI4792. The value for γ_1 is extracted from the theoretical fits.

Having obtained the low-frequency data, the voltage frequency was fixed at 500 Hz, and the average as well as the standard deviation (std dev) of the data were measured. The results are shown in figure 3.5.

The resultant fitted parameters are outlined in table 3.1, along with literature values, or values quoted on data sheets from Merck. As can be seen, the discrepancies between these values are fairly minor, and can easily be attributed to small changes between batches, and small contaminations that can affect the LC alignment. The values for the pre-tilt are all reasonable based on past measurements of similar cells using the crystal rotation method discussed in chapter 2.

Observing the frequency-dependent standard deviation of the intensity oscillations, the deviation falls exponentially as the frequency increases, which is expected as the LC molecules are able to respond less quickly to higher frequencies. The fit is generated

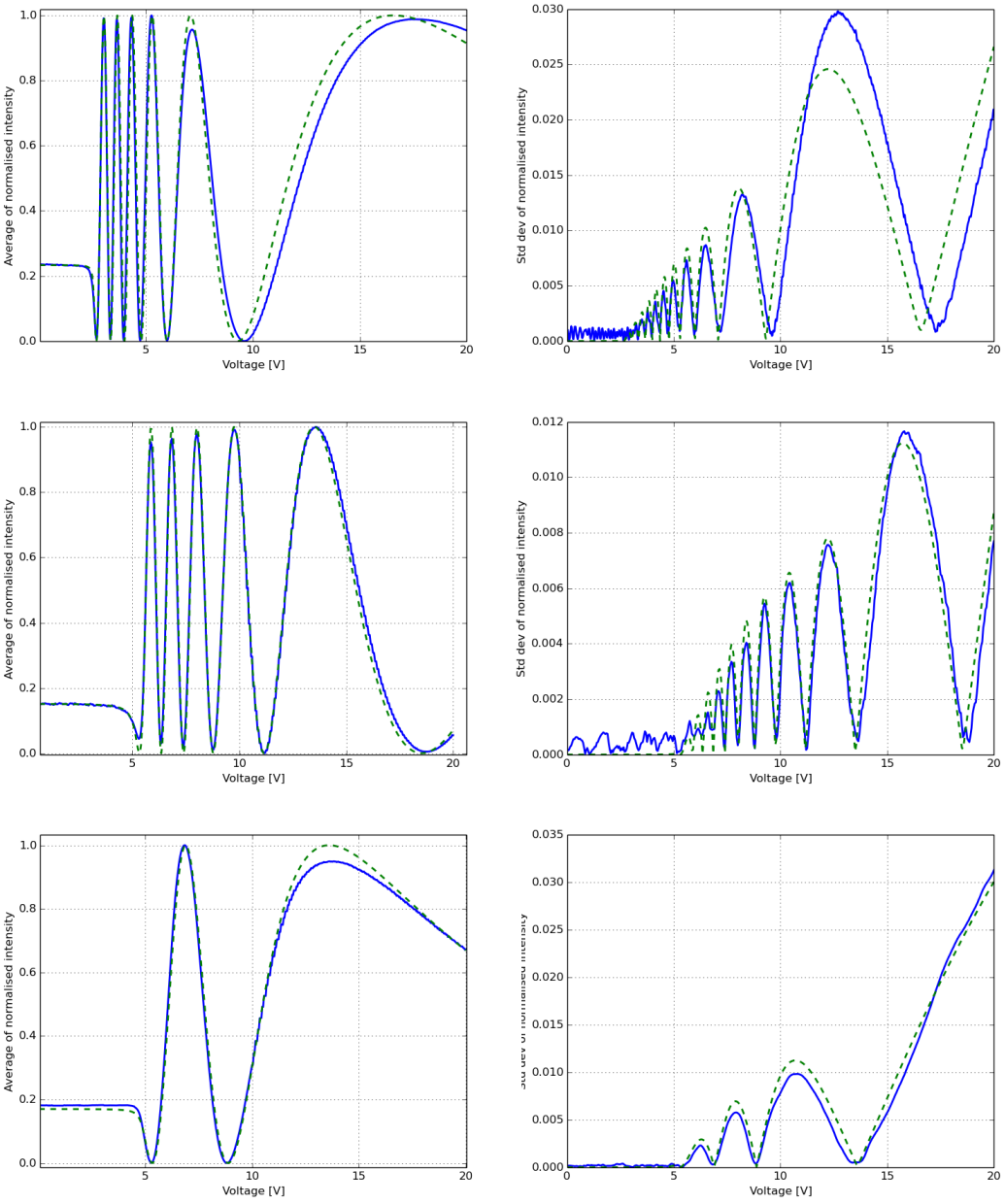

Figure 3.5: High-frequency measurement of $\alpha_4 + \alpha_5$ for E7, TL205 and ZLI4792 are shown, with the average of the intensity signal (used to measure K_1, K_3, thickness and pre-tilt) in the left-hand column, and the standard deviation of the signal (used to measure $\alpha_4 + \alpha_5$, using the previously calculated value of γ_1) shown in the right-hand column. The experimental data are shown by the blue line, and the fit is shown by the green dashed line in each case.

	d	K_1	K_3	θ_0	γ_1	$\alpha_4 + \alpha_5$
E7 [20]	14.4 μm	10.9 pN	18.0 pN	0.5°	203.6 ± 0.06 mPa s (280.8 mPa s)	431 ± 58.4 mPa s (316.8 mPa s)
TL205	15.0 μm	16.5 pN	20.3 pN	1.2°	303.0 ± 9.54 mPa s (367 mPa s)	403.0 ± 6.16mPa s
ZLI4792 [67]	11.7 μm	14.8 pN	19.8 pN	1.8°	109.6 ± 1.44 mPa s (95.0 mPa s)	133.4 ± 3.08 mPa s (115.0 mPa s)

Table 3.1: The material parameters and errors for E7, TL205 and ZLI4792 calculated from the theoretical fits shown in figures 3.4 and 3.5. The literature viscosity values are shown in brackets, and were measured at 20.3°C, 20°C and "room temperature" for E7, TL205 and ZLI4792 respectively. The TL205 literature value is from the corresponding Merck data sheet.

using the constitutive equations with the appropriate form for the voltage, and generally the points lie very close to the fitted values. Experimental errors such as laser drift, temperature fluctuations and ambient light sources were minimized during the experiment, and it has been experimentally determined (by scanning the laser intensity over a ten minute time period) that these errors are small enough not to affect the experimental data points in any meaningful way. Fortunately, the fit is strong enough to verify the theoretical method for all but one point in the TL205 data.

The values for γ_1 obtained from the fitting procedure for each LC are summarized in table 3.1, which also includes literature values for this parameter where available. γ_1 is highly sensitive to temperature, an effect which is discussed in section 3.9.

The graphs showing the 500 Hz voltage scan in figure 3.5, along with the traces fitted to the data using the measured value of γ_1 and the fitting parameter $\alpha_4 + \alpha_5$. The behaviour is expected due to the known behaviour of the CPI, which accounts for the deviation of the intensity oscillations falling to 0 where there is a turning point in the CPI (see figure 3.2), and is also predicted by equations (3.3) and (3.4), which show that there is a higher transfer of energy to the centre of the cell for a higher applied voltage.

3.8.1 Discussion of time response data

Statistical tests have been performed in order to judge the significance of varying the fitting parameters, and they have shown a high degree of significance, as well as proving that the fitted parameters are well constrained. However, there is some observable deviation between the measured values and the fit, particularly for the case of E7 as shown in figure 3.5. This deviation is almost certainly due to the same effect that has altered the CPI, where it is clear that the normalized peaks do not always reach a value of 1. This means that the laser intensity output from the system is either higher or lower than expected at one or more of the turning point voltages seen in the CPI.

It is not yet clear what the cause of these deviations are. Experimental tests of common noise sources, such as laser drift and electrical noise in the photodiode and amplifier circuits, have been eliminated as potential candidates, leaving one to conclude that the source of error (or missing physics from the model), lies with the LC cell itself, and therefore presumably with the LC dynamics. One possible candidate is scattering, which can occur in LC cells with imperfect alignment and hence a non-uniform refractive index profile in the x-y plane, although it is an effect that is most commonly seen around the Frederiks transition, and hence is not likely to be the dominant effect in this case where the error source affects the intensity at a higher voltage.

One effect that definitely is missing from the model is a term in the free energy that describes the flexoelectric effect, which is described in some detail by Osipov [68], but essentially describes an effect whereby deformations in the structure of the mesogens cause a small electrical polarization, which contributes to the electrical term in the free energy functional. The flexoelectric coefficient of E7 [69] is higher than that for TL205 (which has been shown as being too low to measure by Dr Ben Snow of Merck Chemicals) or ZLI4792 [70], and therefore it is possible that this effect could account for the fact that the theory does not fit the E7 data as well as the TL205 data. This was checked by introducing the flexoelectric term into the free energy used to fit the CPI data and checking the effect that the known flexoelectric coefficient of E7 would have on the director configuration and hence CPI intensity. Unfortunately, it was found that the coefficient for E7 was not high enough to make a significant difference to the

behaviour of the system, and therefore one can assume that the flexoelectric effect is not responsible for the deviation of the E7 CPI from the expected response.

One last potential candidate to explain this departure is pre-twist. It is impossible to obtain a perfectly aligned surface using a rubbed polymer technique, thanks both to stray strands in the rubbing cloth itself, and small contaminations due to ambient conditions. There may potentially be very small twist variations at various points in the cell. Interestingly, when the effect of pre-twist was investigated by this group, it was found that the effect would be very difficult to spot when observing a cell under crossed polarizers, but the effect could change the height of the peaks in the crossed polarised intensity. There was no time to investigate introducing this effect into the model for fitting the CPI, but it is for now the strongest candidate that can account for the poor fit in the E7 cell used for this experiment.

High temperatures tend to lower the nematic viscosity coefficients, as is the case in isotropic liquids. The viscosity is in fact extremely sensitive to temperature changes, which makes the vague recording of "room temperature" in many publications a challenge when comparing to previous results. This temperature dependence holds true for every viscosity coefficient as predicted by Imura-Okano theory [71], where it is shown that the tensors used in the derivation of equations (3.3) and (3.4) are dependent on some order parameter, which in turn is temperature dependent as stated in section 1.2.1. This theory has been used to model the temperature-dependent rotational viscosity of E7 by Wang *et al.* [20]

The error values were not calculated by the author, but a brief overview is given in section A.4.3.1. The method for finding these error values takes into account the goodness of fit as well as how well constrained the fitting parameters are. It should be noted that more repeats of the experiment are necessary, as the Fisher information (see section A.4.3.1) used to calculate the errors will underestimate the error values with a single data set.

3.9 Conclusions of the optical-probe measurement of nematic time response

Despite the slight limitations in the method when it is applied to certain cells, one can conclude that the technique presented here is a reliable way of measuring the viscosity parameters γ_1 and $\alpha_4 + \alpha_5$ by using a standard CPI setup and carefully controlling the applied voltage signal. In particular, γ_1, which is the parameter responsible for the rise and fall times of LC devices and is hence the more technologically useful material constant, can be measured extremely easily using a low-carrier-frequency AM voltage signal, where the two voltage working points can be chosen by analysing a CPI trace.

$\alpha_4 + \alpha_5$, the parameter responsible for coupling between the oscillations of the director and fluid flow in the cell, can be measured by taking the standard deviation of the intensity signal as a function of voltage during a CPI experiment. The frequency of the voltage signal must be sufficiently low for these oscillations to be non-negligible, and the experimental setup must be tuned very carefully, especially with regards to laser intensity, photodiode amplification and the resolution of the data acquisition hardware used. Future experiments could investigate the effect that frequency has on these oscillations in more detail, in order to chose an optimal frequency which will give a higher signal and, in turn, further reduce the signal-to-noise ratio.

Error values for each of the parameters in table 3.1 have been calculated using the Fisher information as described in section A.4.3.1, although this method will underestimate the error when it is applied to a single data set. Future work will need to focus on repeating the experiment in order to calculate these errors more precisely. As it stands, there are large discrepancies between the values measured in this experiment, and literature values for the same parameters. While these discrepancies can potentially be accounted for by temperature variations and contaminations in different batches of LC, it will be important to repeat the experiment in order to have a reliable error value for comparison.

The main advantage of this method is the simplicity when compared with any other methods for measuring the time response of LCs, particularly as the optical setup is present in most LC laboratories. It is a fast way of determining the rise and fall time

of any nematic material in planar alignment, and can in principle be more useful to the average researcher than any previous characterization technique.

Thus far, numerous experimental techniques for measuring LC parameters have been discussed in chapter 2, and a new method for measuring the time response of nematic fluids has been outlined and described in this chapter. The following chapter, chapter 4, describes two more novel characterization techniques that can be applied to LC light valves.

Chapter 4

Measurements of voltage transfer function, and two-beam coupling

This section outlines two new experimental techniques that are used, in this case, to characterize liquid crystal light valves (LCLVs as described later in chapter 6) - hybrid LC cells where one of the alignment layers is photoconductive, leading to a photorefractive response. The two techniques have been introduced in chapter 2 as the voltage transfer function (VTF) and AC two-beam coupling (TBC).

The VTF in particular could find applications in other studies of liquid crystal devices as discussed in this chapter. The techniques will be described in detail, as will the resultant calculations of LCLV parameters and response to optical and electric fields.

Finally, there will be a discussion on the theory refinements necessary to improve the accuracy of the predictions and the interpretations of the resultant data, and a framework for that theory will be proposed.

The work presented in this chapter has been published in [1] and [2].

4.1 Photorefractive liquid crystal systems under an AC field

Photorefractive effects can be achieved in liquid crystal systems in many different ways, such as thermal non-linearities, dye doped systems and the use of photorefractive crystalline windows.

The systems under consideration in this thesis are constructed in the same way as a normal planar cell, but with one of the passive alignment layers replaced by a material with photoconductive properties, as described in chapter 2 and in more detail in chapter 6. The photorefractive effect is a result of optical modification of the conductivity of one of the alignment layers, which can in turn modify the voltage dropped across the LC layer. In this way, variations in the intensity of incident light can lead to changes in the refractive index of the system.

Herrington *et al.* [72] suggested that photorefractive effects, characterized by TBC gain, could be enhanced in systems using poly-vinyl carbazole (PVK) doped with C_{60} as an alignment layer when probed with a low-frequency AC field rather than a DC field. An earlier study from Song et al [73] also used an AC field to achieve TBC in a photorefractive LC system, but the mechanism in this case is due to a photo-active, fullerene dopant, and the LC was homeotropically aligned.

The work of Herrington et al was inspired by two inherent problems with controlling a photorefractive LC system using a DC field. Firstly, a DC field applied to a cell for long periods of time can cause damage to a cell [74], and secondly, the field can induce ions in an LC to move towards the surfaces of the cell. These ions form space charge layers which screen the field as shown in figure 4.1. Scalerandi et al described the time evolution of ion layers in LC slabs in more detail [46], and found that charge screening can begin on time scales less than that of the LC response, but also that the formation of these layers can continue over several hours. It is therefore very difficult to say with any certainty that a steady state has been reached if using a DC field with these devices.

An AC field should immediately remove these two issues, as the charged ions in the cell experience, on average, no field, and it is for this reason that most modern LC displays

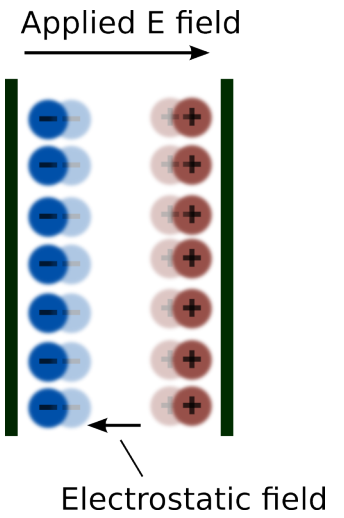

Figure 4.1: Space charge layers induce an electric field, anti-parallel to the applied field.

use an AC field to switch LC pixels [11]. Of course, if the frequency is low enough that the time period is comparable to the time scale over which charge layers form, then the effect of charge layers must be considered when modelling the electrical response of the cell. This will be discussed as future work in chapter 7.

The challenges are to determine whether the system would exhibit a photorefractive response when probed with an AC field, and whether the photorefractive mechanism in the AC case is the same as in the DC case, challenges which the VTF and TBC measurements are designed to solve. Results from [72] show that it is possible to achieve a higher TBC gain in an AC regime, which is a result that can be further verified by the techniques. Optimizing the photorefractive performance of these cells, either by finding the ideal operating voltage frequency or by measuring the VTF or TBC while changing other parameters would be extremely helpful when designing and implementing photoconductive polymer based LC light valves, which already exhibit extremely high optical nonlinearities [75].

The VTF as described in chapter 2, is designed to directly measure the relative voltage drop across the aligning polymer layers and the LC layer in an LC light valve. This is done by measuring changes in the Frederiks transition as the frequency of the applied field changes. Furthermore, we have developed a simple model to reproduce the experimental results, which has two characteristic time constants: one relating to the

relative conductivity of the layers, and another relating to the time response of the LC layer. While the model is not accurate enough to measure material parameters with high precision, it is sufficient to explain the difference in how different LCs respond to the low frequency portion of VTF plots, and the time constants do allow a comparison between different materials as well as helping to predict relative TBC strengths for different materials.

Measuring the VTF under different light illuminations will grant insight into the photorefractive mechanism under the application of an AC field. Ultimately, photorefractivity is the result of the voltage drop across the LC layer being coupled to the incident light intensity, and the VTF will allow a direct measurement of this voltage drop as a function of the applied voltage frequency. Furthermore, observing the voltage drop over the course of one time period of the voltage oscillation will grant insight into the charge movement in the layers, as e.g. electrons and holes tend to have different mobilities in the photoconductor [76], as well as experiencing different injection barriers at the ITO layer [77].

TBC is a useful technique for assessing the strength of optical non-linearities in this system as a function of the applied voltage, as well as being a useful application for LCLVs. Analysis of the peaks observed in these data grant an insight into the material parameters that have the most profound effect on the TBC strength, which in turn will help when designing an optimal device. These insights will be carried over to chapter 6, where new materials for use in LC light valves are discussed in detail.

4.2 Measuring the voltage transfer function

The experimental set-up has been discussed in detail in chapter 2, and is shown in figure 4.2.

The main difference between the previously mentioned CPI experiment and the VTF is in how the voltage is applied for the VTF. The voltage application process is as follows.

A voltage signal, $V = V_0\mathbb{R}\left[\exp\left(i\omega t\right)\right]$ - where V_0 is the voltage amplitude, ω the frequency and t is time - is applied to the cell. In the initial state, $V_0 = 0$ and ω is at the highest

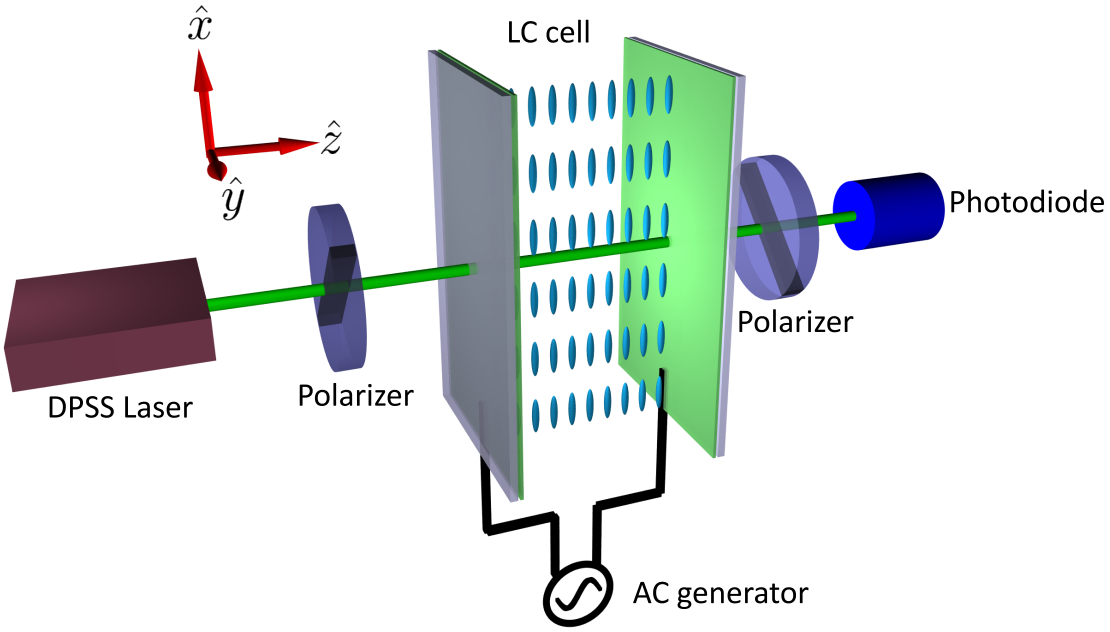

Figure 4.2: Schematic diagram for VTF.

set value: typically, the frequency $f = \omega/2\pi$ will be varied between 1000 Hz and 0.1 Hz. V_0 is then increased by an increment, the intensity is measured for ten time periods and V_0 increased again until $V_0 = V_{\max}$ where $V_{\max}$ is typically set to 10 V. V_0 is then set once again to 0 V, the frequency is reduced by a logarithmic increment, and the entire process is repeated until the lowest value of frequency is measured.

In this way, the CPI is measured for a varying voltage frequency. While the resolution of the voltage amplitude is generally lower for the VTF than for the CPI experiments described in chapter 2, it is still possible to resolve the important features, namely the peaks in the CPI and the Frederiks transition. The lower resolution is necessary thanks to the long acquisition time, as low frequency measurements have a higher time period: the lowest frequency investigated is 0.01 Hz, at which point the measurement of ten time periods would take ~ 17 minutes.

The experiments described here used the following parameters. The laser source was a diode pumped solid state (DPSS) laser operating at 532 nm. The maximum power of the laser is 60 mW, output into a beam with 1 mm radius, but it could be varied by employing a variable neutral density (ND) filter. Linear Polaroid polarizers were used, with an extinction ratio of 10000:1, meaning some light from the laser contributed to a baseline that was removed from the data. The voltage was varied such that V_0 took

values between 0 - 3.5 V, while the frequency f was varied logarithmically from 10^3 to 10^{-2} Hz. LC cells were constructed as described in section 1.3 with one PI layer, and one layer of photoconductive PVK:C_{60} [78]. In both cases, the LC layers were 12 μm thick, and filled one with E7 and one with TL205. In both cases, the displayed results omit areas of no interest, where no change in the behaviour is observed while changing the field.

The procedure was automated using Python software. The intensity output from the cell was measured by a ThorLabs PDA25K photodiode, with an in-built amplifier, although the amplifier circuit was not required in this case. The voltage output from the photodiode was converted to a digital signal and recorded by a NI-6211 data acquisition card. The voltage was applied from an Agilent 33120A waveform generator, that was controlled via a serial connection. The remote control of this experiment meant that it could be run at night, when vibrations could be minimised, and in a dark room to prevent ambient light conditions from affecting the result.

Given that the technique can be applied to photorefractive cells in order to measure the response to varying light conditions, an additional experiment was performed where the laser beam passed through a variable ND filter before hitting the cell. In this way, the light intensity could be controlled remotely, and the VTF performed for various light intensities. The ND filter wheel was attached to a stepper motor, controlled by an Arduino UNO [79], which allowed the intensity to be controlled as part of the Python program.

The measured intensity was then plotted on a color chart as shown in figures 4.3 and 4.4.

4.3 Modelling the VTF intensity behaviour

A non-linear filter model is developed here to describe the results of the VTF in terms of two characteristic time constants. One of the time constants is related to the relative conductivity between the LC layer and the photoconductive layer, and can be calculated as a function of the incident light intensity. Both the relative conductivity and the

photoconductivity in the light and dark conditions are important to consider when predicting the photorefractive response of LC light valves, which is a result that will be proved in section 4.7.2 of this chapter. The second time constant is related to the time response of the LC, which is an important characteristic for applications of LC light valves, as shown in chapter 3. The model was developed by Dr James Bateman of the department of Physics and Astronomy at the University of Southampton.

It should be noted that the goal of this model is not to provide accurate predictions of the VTF data. In order to do this, a more robust model that takes into account the ionic charge in the LC layer [32], as well as the non-ohmic behaviour of PVK [80] should be developed. In this case, the model is designed to identify the physical properties of the system (i.e. the relative conductivities of the layers and the time response of the LC) that have an effect on the VTF when measured under various light illuminations, but it is not designed to quantise these properties accurately.

The cell is modelled as an electronic circuit. Each layer has a characteristic impedance, described by a resistor in parallel with a capacitor. For this model, the alignment and space charge layers are treated as a single impedance which is in series with the LC layer.

The impedance of these single layers is given by:

$$Z = \frac{R}{1 + i\omega RC} \tag{4.1}$$

where R is the resistance and C is the capacitance. For higher frequencies this reduces to a pure capacitance, while for lower frequencies this reduces to a pure resistance. The alignment layers are extremely thin compared to the LC layer, and the capacitance of the layers, C_K is therefore much larger than that of the LC. The consequence is that the voltage drop is entirely across the higher-impedance LC layer at high frequencies.

The alignment layers are highly resistive however, and therefore will cause a voltage drop at lower frequencies, where the voltage is shared more equally between the polymer and LC layers. This voltage drop should be measurable, as it will manifest as a higher

apparent Frederiks transition, where the measured voltage value for the transition is the sum of the polymer voltage drop and the voltage required to switch the LC.

We can therefore treat the voltage drop across the LC layer as experiencing a high pass filter with a cut-off frequency of $1/C_K R_L$ which we will label ω_{VTF}. The voltage measured across the LC layer will therefore be given by [81]:

$$V_L(\omega) = \frac{1}{\sqrt{1 + (\omega_{\mathrm{VTF}})}} V_0 \tag{4.2}$$

The next step for this modelling is to characterize how the LC responds to an applied voltage subject to this filter. According to DeGennes and Prost [31], the LC responds to the square of the field. The square of a voltage which is oscillating in time at frequency ω gives two terms: one constant in time, and the other oscillating at 2ω, both of which are halved.

A forcing term which contains these two contributions is given by:

$$U_{\mathrm{eff}} = U_0(\omega) + U_2(\omega) \cos 2\omega t \tag{4.3}$$

where t is time, and the next step is to derive expressions for these two terms in terms of the driving voltage. $U_0(\omega)$ is simply the squared, non-varying voltage $\frac{V_0^2}{2}$. For the second term in equation (4.3), it is necessary to consider another aspect of LC response.

The LC can only follow an oscillating voltage up to a point due to the intrinsic time response, τ_i. The time response is given as a ratio between the rotational viscosity, γ_1 and the elastic constant describing the deformation, K_1 in this case. If the forcing term is oscillating with a frequency sufficiently higher than the reciprocal of this time response, then the LC cannot follow the voltage at all.

We can treat this response as a low-pass filter applied to the voltage, with a cut-off frequency relating to the LC time response. $U_2(\omega)$ can therefore be given as:

$$U_2(\omega) = \frac{U_0(\omega)}{\sqrt{1 + 2\omega/\omega_T}} \tag{4.4}$$

where $\omega_T = \frac{2\pi}{\tau_i}$.

The modelling results are shown in section 4.3.2. The full details of the model are discussed by Bateman *et al.* [1].

4.3.1 Fitting to the VTF data using the non-linear filter model

To start fitting the data, we need some way of relating the applied voltage to the intensity measured. This is done by taking a cross section of the intensity data as a function of amplitude at one high-frequency voltage, where the forcing term reduces to $\frac{V_0^2}{2}$. This gives a relationship, $I_\perp(U_{\text{eff}})$ which can be used as a callibration curve to relate the rest of the intensity data to the forcing term. A least-squares fit is used to find the values for τ_i and ω_{VTF} which give closest agreement between the model and the experimental data. This is done for the mean and the range of the intensity over one time period of intensity oscillation.

4.3.2 Results of VTF characterization for two LCs, and comparison to theory

The resultant VTF measurements for two LC cells are shown in figures 4.3 and 4.4.

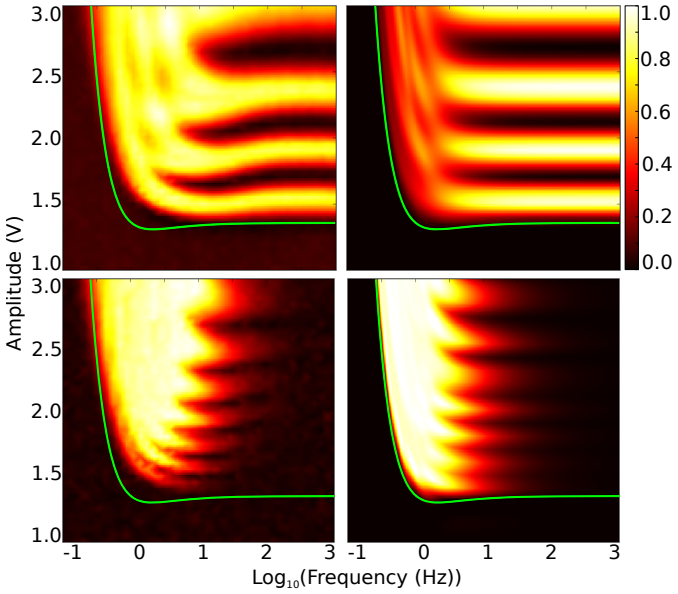

Figure 4.3: VTF plots showing the mean and range (top and bottom respectively) and the experimental/theoretical data (left and right respectively) for E7. The color bar shows the normalized intensity, scaled by a factor of 10^{-3} for the range data. The green line traces the apparent Frederiks transition described in section 4.4

.

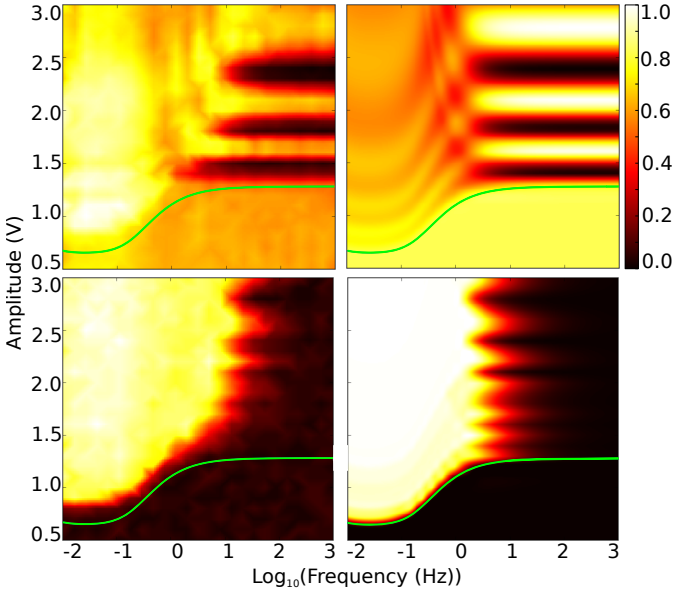

Figure 4.4: VTF plots showing the mean and range (top and bottom respectively) and the experimental/theoretical data (left and right respectively) for TL205. The color bar shows the normalized intensity, scaled by a factor of 10^{-3} for the range data. The green line traces the apparent Frederiks transition described in section 4.4

.

The VTF was also performed under varying light intensities. Four intensities are shown for E7 in figure 4.5, and two for TL205 in figure 4.6. The VTF for TL205 did not vary significantly with light intensity, and hence only the lowest and highest intensity (0.092 mW/cm^2 and 22 mW/cm^2) investigated are shown.

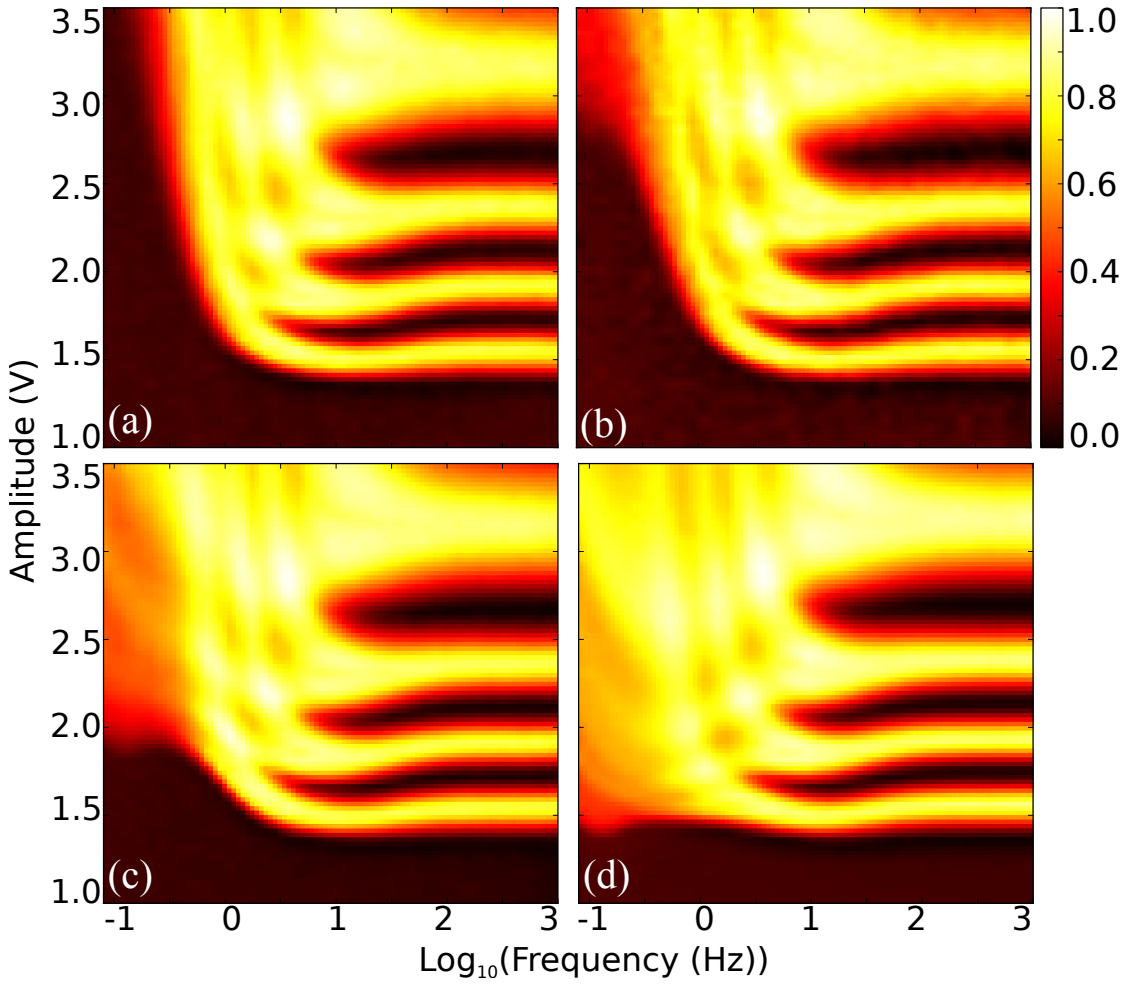

Figure 4.5: VTF plots showing the mean intensity for E7. The color bar shows the normalized intensity. The intensities incident on the cell are (a) 0.18 mW/cm^2; (b) 1.8 mW/cm^2; (c) 5.7 mW/cm^2; (d) 68 mW/cm^2. The behaviour shown here is explained in section 4.4.

The difference in the apparent Frederiks transition was estimated as the point at which the intensity deviated from the initial low-voltage value by 0.1, and the Frederiks transition as a function of applied frequency for various light intensity levels in the E7 experiment is shown in figure 4.7

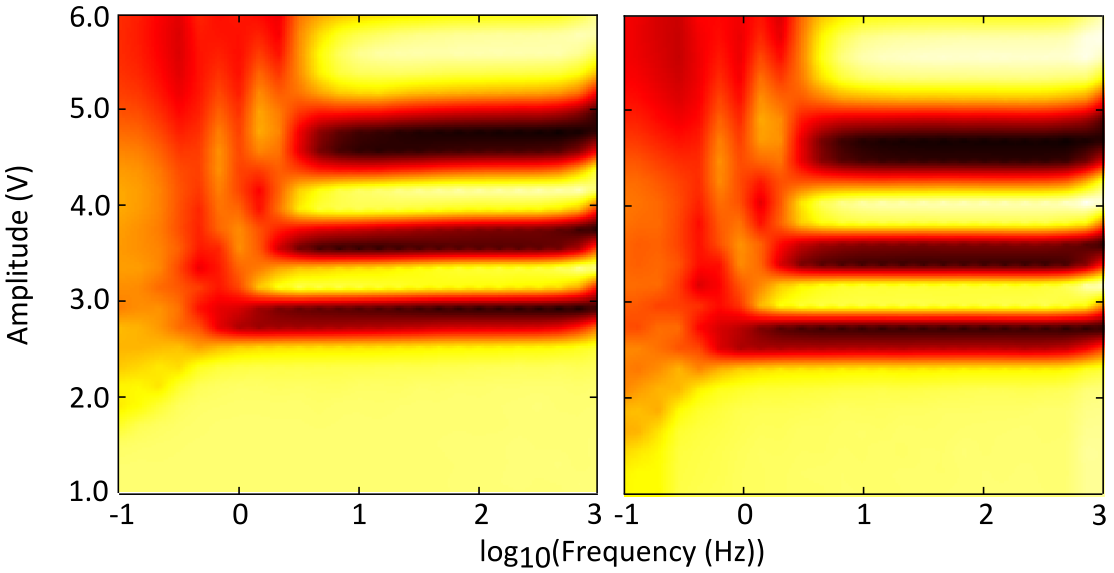

Figure 4.6: VTF plots showing the mean intensity for TL205. The color bar shows the normalized intensity. The intensities incident on the cell are 0.092 mW/cm^2 for the left-hand plot, and 22 mW/cm^2 for the right-hand plot. The behaviour shown here is explained in section 4.4.

4.4 Discussion of resultant VTF data and theoretical fit

The fitting parameters obtained for the best fit are compared to literature values for conductivity and time response of the two LCs used in this experiment, in order to verify that the relative conductivity and the time response of the liquid crystal are key parameters when explaining the VTF results.

Firstly the conductivity, which is responsible for ω_{VTF}, the characteristic frequency that appears in the high-pass filter described in section 4.3, is discussed. Converting to a time constant $\tau_{\mathrm{VTF}} = \frac{2\pi}{\omega_{\mathrm{VTF}}}$, the fitted value for E7 is 1.24 ± 0.05 s. The fitted value for TL205 on the other hand, is $\omega_{\mathrm{VTF}} = 0$, which implies that the time constant is greater than 100 s: the highest time period measured in this experiment. This is actually immediately obvious from figure 4.4, as the high-pass filter should decrease the voltage drop across the LC layer at lower frequencies. Since the apparent Frederiks transition does not increase, we can conclude immediately that the high-pass filter is not coming into effect at the measured frequencies.

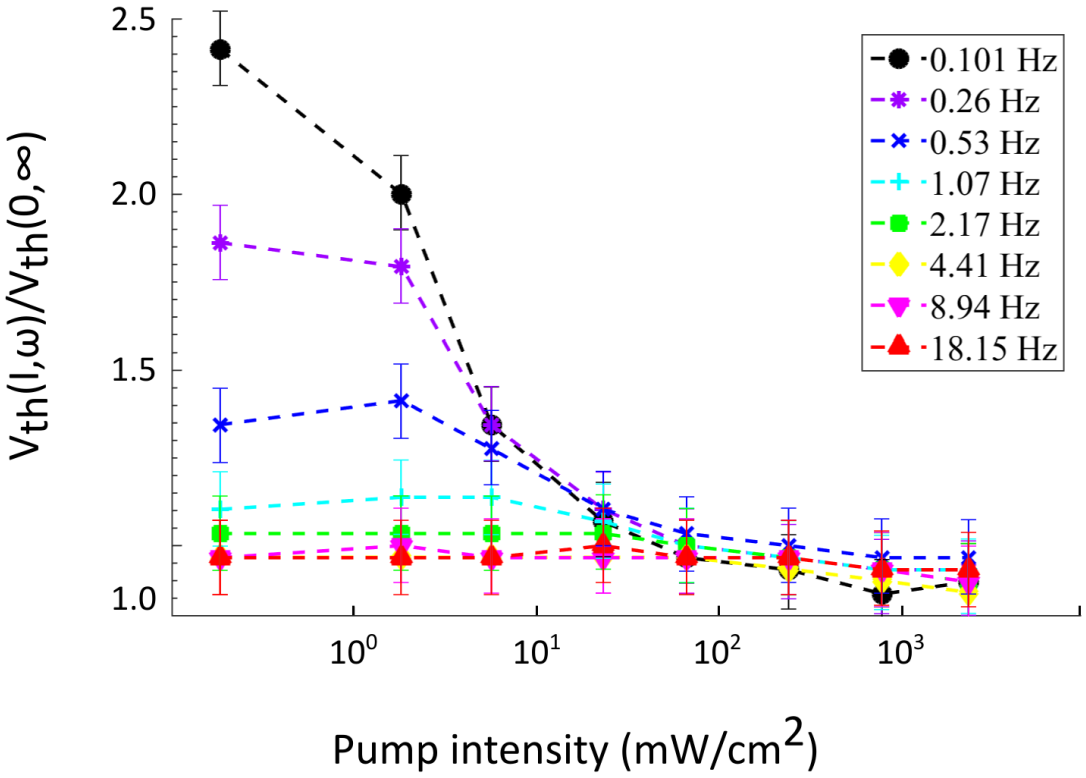

Figure 4.7: The apparent Frederiks transition - scaled by the Fredericks transition at high frequency - as a function of light intensities in a PI/PVK:C_{60} cell filled with E7 are shown. Each colored line corresponds to a different applied frequency. All data were extracted from figure 4.5, as well as two additional plots not shown in figure 4.5. The error bars are calculated using the method described in section A.5.

The measured time response τ_{VTF} can be compared to a calculated value for E7. In order to do this, we convert $\tau_{\mathrm{VTF}} = R_L C_k$ to:

$$\tau_{\mathrm{VTF}} = \epsilon_0 \epsilon_k \frac{d_L}{d_k \sigma}, \tag{4.5}$$

where ϵ_0 and ϵ_k are the vacuum permittivity and the relative permittivity of PVK:C_{60} respectively, d_L and d_k are the thicknesses of the LC and PVK:C_{60} layer respectively, and σ is the conductivity of the LC. σ is given as 10^{-8} Sm^{-1} (siemens per metre) by Tomylko *et al.* [82], while the dielectric permittivity of PVK is 3 according to D'Angelo *et al.* [76], and we assume that the low doping concentrations of C_{60} do not have a large effect on this value. In this case, 12 μm cells are used, and the PVK:C_60 has a thickness of $\approx$ 50 nm measured by atomic force microscopy. Inserting these values into equation (4.5) gives a value of 0.6 s. There are no measurements of the conductivity of TL205

in the literature, making it impossible to calculate τ_{VTF} accurately. However, there are references to it being at least two orders of magnitude lower than E7 [83], which would correspond to a value of τ_{VTF} for TL205 of > 60 s.

The measurement of τ_T, the characteristic time response of the low-pass filter described in section 4.3, is now discussed. Ignoring fluid flow, the time response is given by $\tau_T = \frac{d^2\gamma_1}{K_1}$ as described in chapter 3. For the cells measured here, $d = 12$ μm, and γ_1, K_1 are 225 mPa s, 11.2 pN for E7, and 367 mPa s, 17.3 pN for TL205 [84, 85]. These give values for τ_R of 2.9 and 3.1 s for E7 and TL205 respectively, while the fitted value of τ_T is 0.7 ± 0.1 s for both LCs.

The green line traced on figures 4.3 and 4.4 represents the apparent Frederiks transition (i.e., the voltage applied to the cell at which the Frederiks transition occurs), and is obtained by finding the point at which the intensity changes by more than 5% of the maximum intensity value. As we know the voltage drop across the liquid crystal layer is the same at this point, regardless of frequency (again, the Frederiks transition is a constant material property), we can use the green line to work out the relative voltage drop across the other layers in the system for any frequency. This green line has been used to extract the values for the apparent Frederics transition plotted in figure 4.7.

Measuring the VTF for different light intensities shows that a TL205 cell reacts very differently from an E7 cell. It is easy to see from the extracted data shown in figure 4.7 that the light intensity affects the Frederiks transition at frequencies lower than 0.128 Hz. Changing the intensity of light while holding a cell at these frequencies can change the Frederiks transition by a factor of up to 2.4 at the lowest measured frequency of 0.08 Hz. This effect is far smaller for the equivalent TL205 cell.

4.5 AC two-beam coupling

In addition to applications in optical networks, two-beam coupling (TBC), as introduced in chapter 2, is an effective tool for obtaining a figure-of-merit: a parameter which can be used to compare between different photorefractive materials and systems. However, in order to achieve TBC in an LC light valve, it is necessary to apply an electric field.

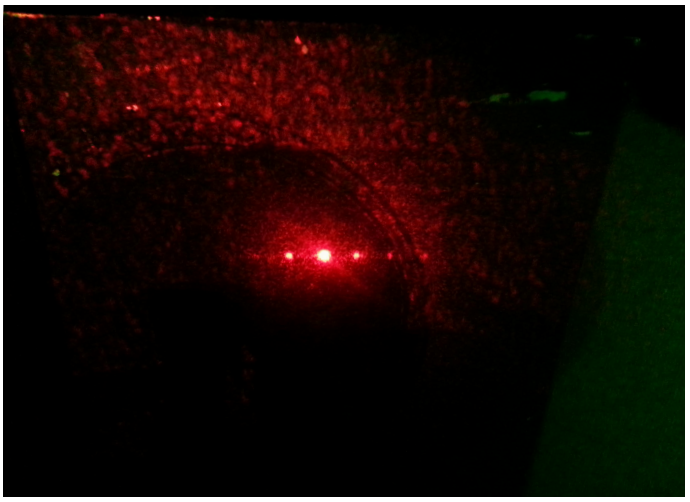

Figure 4.8: Photograph of self-diffracted beams from a typical liquid crystal light valve.

While this has its drawbacks - e.g. the use of ITO electrodes causes the systems to be opaque at certain wavelengths such as terrahertz radiation [86] - it does allow TBC gain to be switchable and tunable over timescales defined by the time response of the LC. However, addressing the light valves using a DC field can be detrimental as described in section 4.1, and it is therefore useful to determine whether or not these devices will work in an AC regime.

When this was attempted by Herrington *et al.* [72], it was discovered that the gain could be higher when addressing cells with an AC field. What follows is a more comprehensive study into the effect of an AC field, and how the mechanism compares to the DC case.

4.6 Measuring AC beam coupling

The experimental set-up we used to measure AC TBC is shown in figure 4.9. Two 12 μm cells were measured, one filled with E7 and the other with TL205. The ITO/glass cell walls were spin-coated, one with PI and the other with PVK:C_{60} as described in chapter 1. E7 and TL205 have a similar birefringence, while the conductivity of E7 is much higher than TL205 as quoted earlier [83], which will allow us to investigate the role of conductivity in TBC strength and the AC frequency at which beam coupling occurs. The cells were tilted at 30° in order to induce beam coupling as described in chapter 2, and the angle bisecting the two writing beams was set accordingly to give a grating pitch,

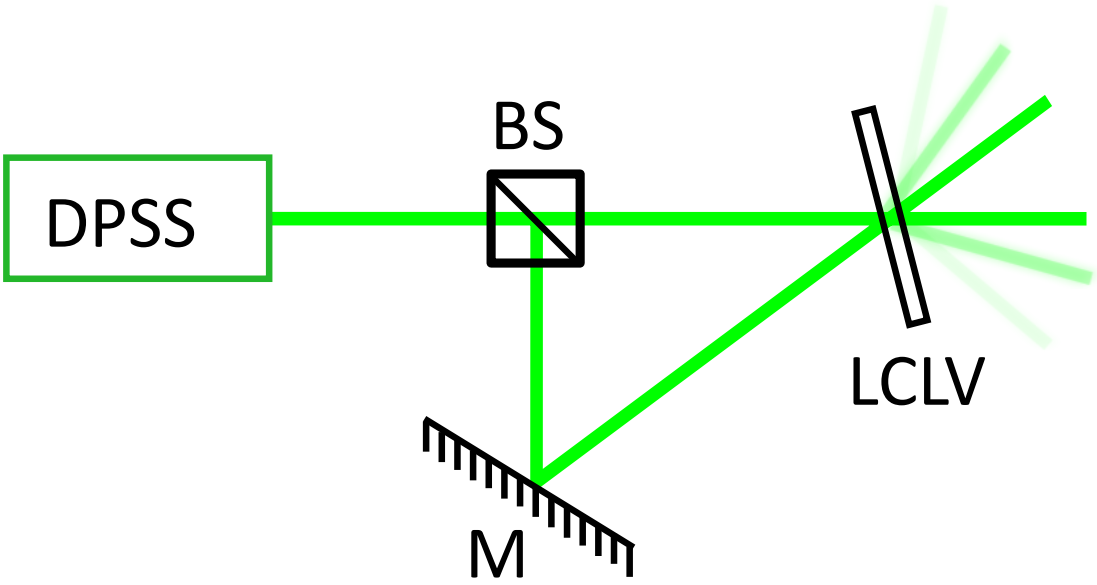

Figure 4.9: Schematic diagram showing the experimental set-up for AC TBC. Light output from the diode-pumped, solid-state laser is split by a 50/50 beam-splitting cube (BS). The two beams are overlapped on the LCLV being measured using a mirror. The cell is fixed onto a rotating stage, and the mirror can be brought closer to the beamsplitter, allowing fine control of the interference fringe spacing.

Λ of 18 μm. The writing beams are split from the output of a DPSS laser operating in the green (532 nm).

The voltage was applied in a similar way to the VTF as mentioned in section 4.2: fixing a value for the frequency of the applied field, scanning up in amplitude, and then repeating the process for a lower frequency. The interesting information occurred for lower frequencies, inspiring the use of a logarithmically varying set of frequency values. The intensity of the two fundamental beams was measured for each frequency/amplitude pair of values, as well as some of the diffracted orders - the number somewhat dependent on the number of available photodiodes.

The intensity measurements were taken concurrently for each photodiode, to avoid transient effects due to laser or voltage drift. The intensities were not measured immediately after the voltage was applied to the cell; instead a 10 s pause is used, in order to allow the LC to reach a steady state, and remove any transient due to the changing voltage conditions. This period was found to be sufficient by observing the behaviour of the LC

on an oscilloscope under a number of different voltage conditions, where the behaviour was observed to regulate < 10 s after applying a voltage.

The behaviour of photorefractive cells at low frequencies will depend on the electrical response of the PVK:C_{60} layer under different field magnitudes and directions. For example, the charge carrier mobility in semiconductors tends to be different for holes and electrons [87], and therefore the conductivity of PVK:C_{60} can change depending on the polarity of the field applied to it.

In order to qualitatively investigate the effect of polarity and the strength of the field on the TBC response of a photorefractive cell, a low-frequency field of 0.1 Hz, with a voltage amplitude of 40 V was applied to a photorefractive E7 cell. The diffracted orders were filmed along with the voltage trace on an oscilloscope, which meant that the diffracted orders could be observed at different points in the voltage cycle.

4.7 Results of TBC in PI-PVK cells

Figure 4.10 shows the intensity of the +0, ±1, and +2 order beam as labelled in figure 4.9. The AC voltage was varied logarithmically in frequency space from 1 kHz to 0.01 Hz, and the voltage amplitude was varied linearly from 0.01 V to 30 V.

The four diffracted orders are shown in figure 4.10 to show the typical TBC behaviour, but in order to characterize the beam coupling response it is only necessary to consider the ±1 order beams rather than the absolute value of TBC gain. This is because the technique is being investigated rather than the devices, and the ±1 order beams are sufficient to compare the TBC gain between E7 and TL205 cells. Therefore, the position and relative strength of peaks of intensity in the first order color maps in figure 4.10 will be considered when modelling the response of these light valves.

The intensity maps of the ±1 order beams for the same experiment with an E7 PI/PVK:C_{60} cell are shown in figure 4.11

The diffracted orders at different points in a low-frequency voltage cycle are pictured in figure 4.12. Four points along the voltage cycle are shown, two points at the peak of

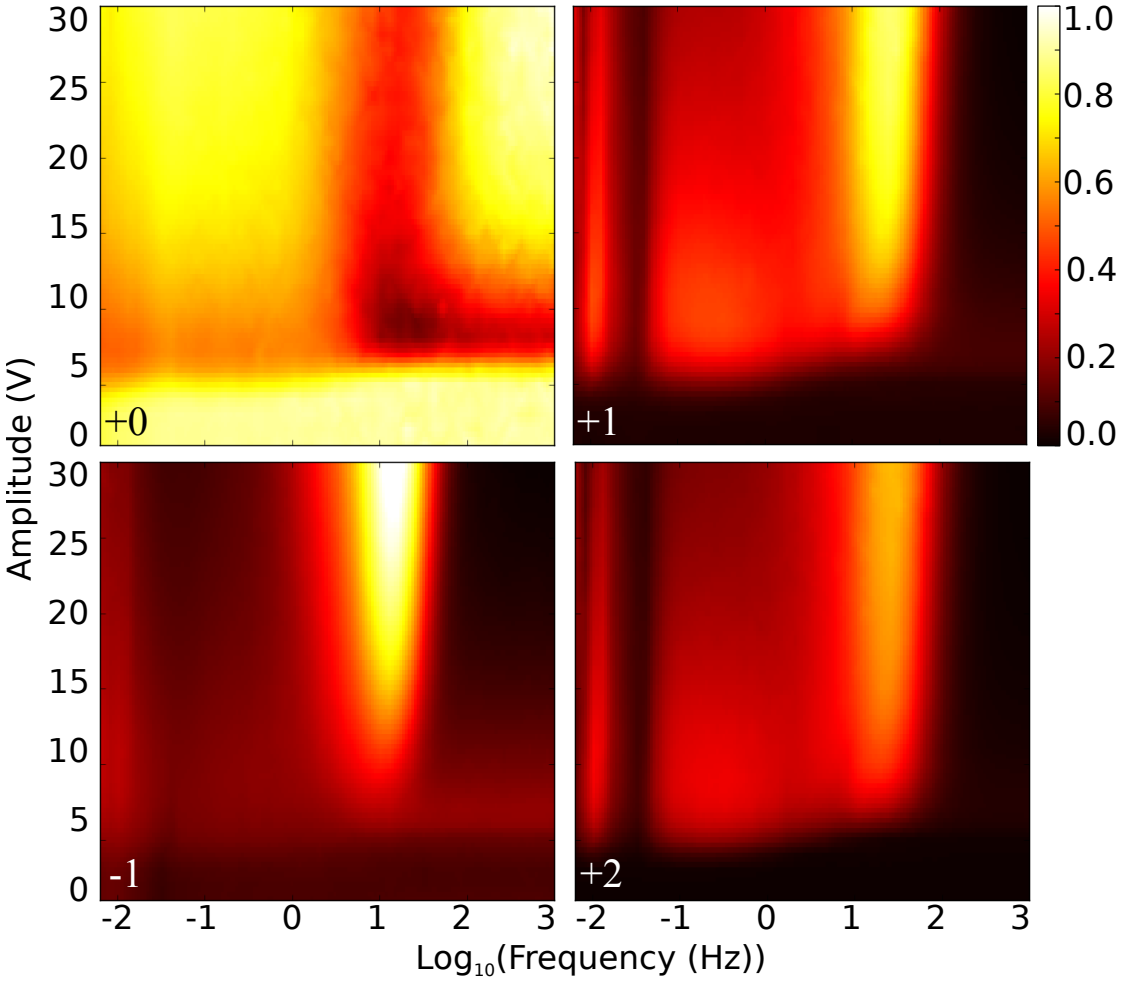

Figure 4.10: Intensity of four diffracted orders for a photorefractive TL205 cell as a function of the frequency and amplitude of the voltage applied to the cell. The color scale covers different ranges for each plot. As fractions of the incident intensity: +0 from 0.9 to 1; ±1 from 0 to 10^{-3}; and +2 from 0 to 5×10^{4} . The average intensity of the beam was 600 mW/cm^2 and the grating spacing 18 μm.

the voltage amplitude, and 2 at a lower, non-zero voltage amplitude. The points also investigate the two different field polarities.

4.7.1 Discussion of TBC data for TL205 and E7 cells

Figure 4.10 shows the energy being transferred between the beams. There is a loss of energy from the +0 order beam centred around $f = 10^{1.1}$ Hz, which corresponds to energy being coupled from this beam into the ±1 order beams.

There appear to be two distinct beam coupling regions for both LCs. In TL205, there are two distinct peaks that can be seen in the ±1 maps: a thin region centred at

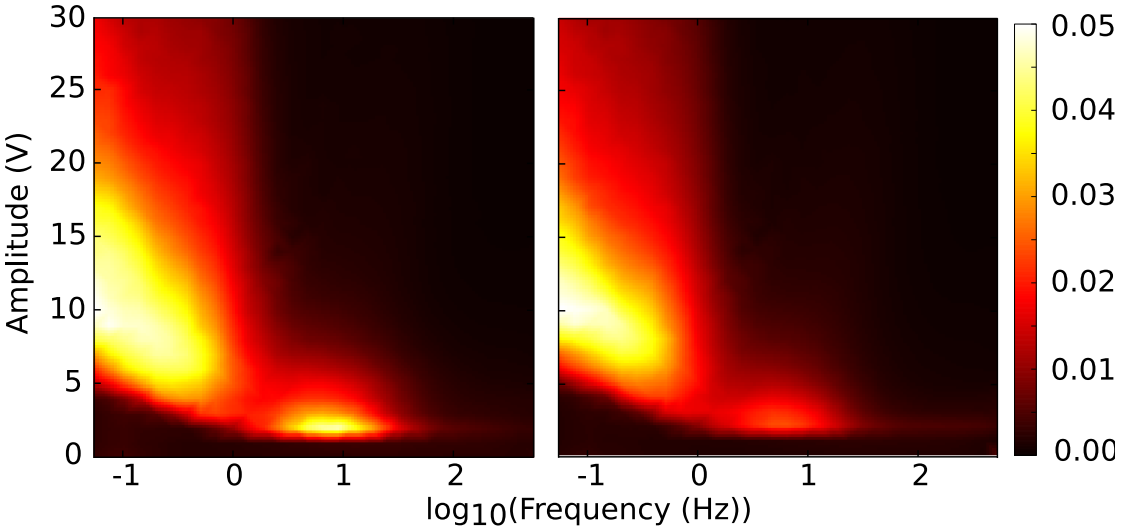

Figure 4.11: The intensity of the ±1 diffracted orders in a photorefractive E7 cell, as a function of the applied voltage frequency and amplitude. The intensity relative to that of the incident beams is shown on the color scale.

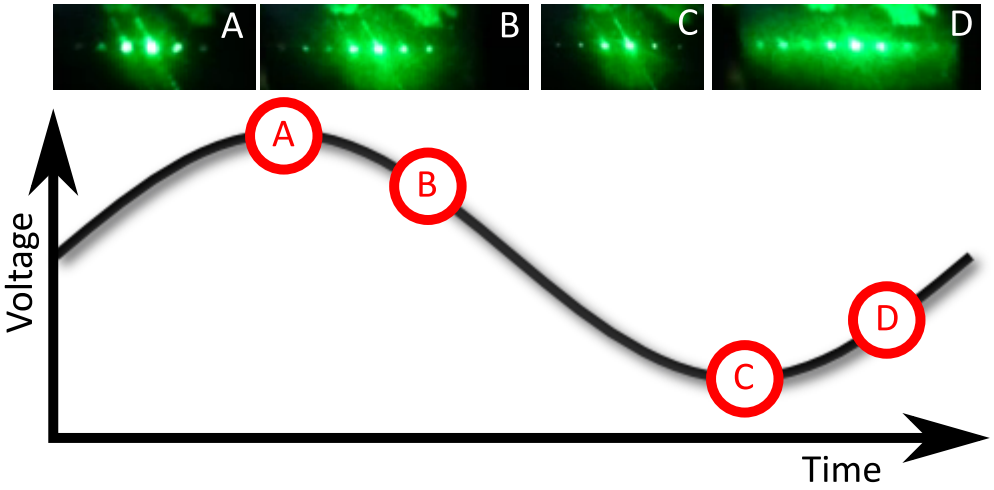

Figure 4.12: Photographs of the diffracted orders from a photorefractive E7 cell in a TBC experiment at different points along the voltage cycle. The voltage frequency was 0.1 Hz, and the amplitude was 40 V.

$f = 10^{-2}$ Hz, and a thicker, more intense peak centred at $\sim 10^{1}$ Hz. In the case of E7, the two peaks are much more distinct, presumably due to the higher intensity of the orders. The low-frequency ($\sim 10^{-1}$ Hz) peak extends over a higher area in this case, while the higher frequency peak at $\sim 10^{0.8}$ Hz disappears very quickly as voltage amplitude increases. The magnitude of the beam coupling, characterized by the relative intensity of the ±1 order beams is 50 times higher for the E7 cell than for the TL205 cell.

Different cells constructed in the same way may give slightly different results; e.g., the

low-frequency peak in the ±1 maps in figure 4.10 is not present for all TL205 cells. Although the cells were constructed in the same way, it is possible that there are some differences due to contaminates in the preparation areas, and the long-term contact between the LC and polymer layers in an older cell may effect the ionic content of the LC or surface charges on the polymer. Furthermore, the VTF results discussed in this chapter suggest that the conductivity of the polymer layers plays an important role in the voltage dropped across each cell layer as the voltage frequency decreases. This role could be affected by even very small variations in the thickness of the polymer layers.

While the experimental results are sufficient to show the voltage frequency and amplitude at which TBC takes place, as well as the TBC gain at these voltages, a theoretical model would describe the physical mechanism that accounts for TBC. Section 4.7.2 outlines the development of such a model.

The diffracted orders at different points in a low-frequency voltage cycle are pictured in figure 4.12.

4.7.2 Theoretical model of AC two-beam coupling

In order to model the electrical behaviour of the illuminated LCLV that leads to the re-orientation of mesogens responsible for TBC, we have to choose an appropriate approach. One way is to combine experimental information of the electro-optic properties of PVK with or without doping (found in the literature: e.g. [88, 89, 90, 76, 91]) with dynamic models of charge-transport in LCs, such as those found in [46, 92, 93] in order to accurately predict the voltage across the LC layer for all applied voltages and light intensities. However, this approach has drawbacks, most notably the lack of accuracy and reproducibility when it comes to measuring the electrical properties of PVK:C_{60}, particularly when it is in contact with an LC. This would make it difficult to reduce the errors of such a model to any significant degree. In addition, such a model would be constrained to one specific system - a given photoconductor in contact with an LC layer. Considering a more generic material in contact with an LC will allow us to build a model applicable to numerous LCLV systems, such as those found in [49, 50].

Therefore the conclusion from Daly *et al.* [94] that the strength of the beam coupling in this type of light valve is roughly proportional to the modulation of the voltage across the LC layer is used. As such, we need not consider the reorientation of the LC at all, nor the beam coupling mechanism itself, but can instead concentrate on the electrical properties of the materials that determine the aforementioned voltage modulation. We consider three layers with different thickness: PVK:C_{60}, the LC and PI. Each layer is parameterized by a homogeneous permittivity and an electrical conductivity which is modulated in the PVK:C_{60} layer.

This model turns out not to be sufficiently accurate to directly predict the behaviour seen in our TBC maps. However, it is a useful tool for interpreting the results in terms of the physical mechanism responsible for TBC, and for intuitively predicting general trends.

The model will be described quantitatively here, while the full mathematical form given in [2] can be found in appendix B. The main results will be duplicated here, as they help to explain the origin of the measured effects.

In order for the photorefractive effect in these cells to exist, there must be transfer of voltage between the PVK:C_{60} and the LC layer. This transfer is defined in the model as a modulation transfer function (MTF), and the strength of the TBC gain should increase with the MTF. The MTF can be calculated using the modulated conductivity of the PVK:C_{60} layer, and the relative voltage in the LC layer.

In order to find the voltage in the LC layer, a solution is found for the divergence of Ampères law, which is equal to zero (the divergence of the curl of a vector field is always zero [23]). A solution for the resulting equation can be inserted into the equation for the MTF, resulting in:

$$\Psi = \frac{A_2}{\sigma_{1,1}} e^{-K_g L_2 \sinh(K_g L_2)}, \tag{4.6}$$

where L_2 is the non-dimensional thickness of the LC layer, $\sigma_{1,1}$ is the non-dimensional conductivity of the LC with respect to the PVK, K_g is the modulus of the grating vector, and A_2 is a proportionality constant, all of which are discussed in appendix B.

4.7.3 Results of TBC model

The modulation transfer function is plotted in figure 4.13 as a function of the non-dimensional frequency and PVK:C_{60} conductivity, for two different grating spacings.

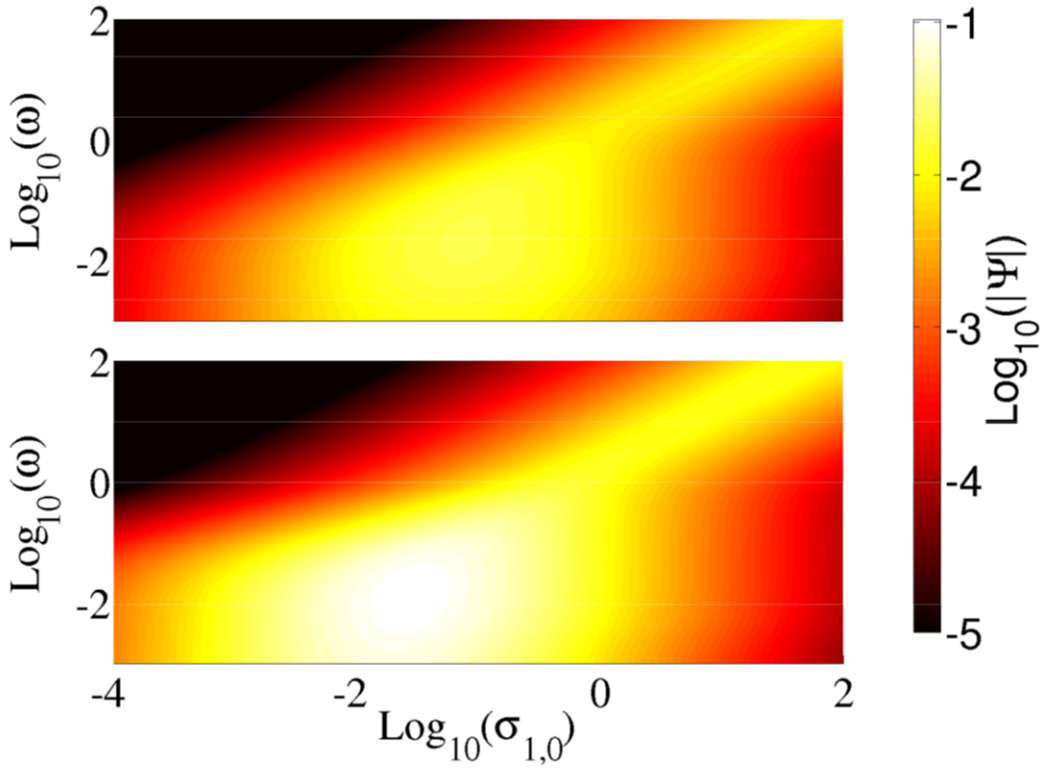

Figure 4.13: The modulation transfer function as defined in equation (B.8), as a function of the PVK:C_{60} conductivity and the non-dimensional frequency (plotted logarithmically), for two different grating spacings: 2 μm and 18 μm for the top and bottom graph respectively. The cell considered has $L_1 = 150$ nm, $L_2 = 12$ μm, and $L_3 = 10$ nm, $\epsilon_1 = \epsilon_3 = 3\epsilon_0$, $\sigma_3 = 10^-3$ and $\sigma_1, 1 = 0.1$. Assuming that the conductivity of TL205, $\tilde{\sigma}_2 \sim 10^{-10}$ S/m (This is two orders of magnitude higher than E7 [83, 82]), we find that $\omega = 1$ corresponds to a frequency of 2 Hz applied to a TL205 cell.

The first point to make about the plots in figure 4.13 is that they are effectively independent of the type of LC used, i.e. the features seen in figure 4.13 do not change as $\tilde{\sigma}_2$, the non-dimensional conductivity of the LC, is changed. Changing the LC will only move the position of the peaks in frequency space, as is clear from the definition of the non-dimensionalized frequency: $\omega = \tilde{\epsilon}_2\tilde{\omega}/\tilde{\sigma}_2$ (these definitions are explained in more detail in appendix B). As an example, figure 4.13 uses a value for $\tilde{\sigma}_2 = 10^{-10}$ Sm^{-1} which corresponds to an estimated value for TL205 (the exact value is difficult to pin

down in the literature, but it is quoted as being two orders of magnitude lower than E7 [83], which has a given conductivity in the order of 10^{-8} Sm^{-1}[82]).

The MTF shown in figure 4.13 is smaller than predicted by a resistance ladder model, which is interpreted as being due to lateral currents ignored by a resistance ladder model. In fact, even for the larger grating spacing case of 18 μm, the difference is significant: 10% for the model considered here, and 25% for a resistance ladder model. The effect of lateral currents is to limit the effect the conductivity modulation has on the LC layer. Equation (B.1) can be solved numerically when relaxing the small conductivity modulation condition, which will give a higher value for the MTF, but even so the effect of the lateral currents still remains.

The amplitude of the modulation, which is an extremely important parameter when considering the effectiveness of these devices, is only significant when the conductivity of the LC layer and the PVK:C_{60} layer are comparable, which in this case corresponds to being within two orders of magnitude of each other.

4.7.4 Liquid crystal response to the MTF

Now that the modulation transfer function has been found, it is possible to examine the response of an LC layer to this field variation. The effect of the grating spacing will be investigated, followed by the effect of the driving frequency.

4.7.4.1 The Bragg and Raman-Nath regimes

The difference between Bragg and Raman-Nath beam coupling has been described in sub-section 2.6.1 of chapter 2. Therein, it was only assumed that light was interacting with a spatially inhomogeneous refractive index grating, and the nature of the grating itself was undefined. Of course, we can now say that such a grating is achieved in an LCLV due to the interaction between the electric field induced by the modulated conductivity of the polymer layer and the LC bulk.

It has been mentioned that no significant beam coupling is observed in the Bragg regime, where the grating spacing is low; we have modelled the MTF for $\Lambda = 2$ μm for this case.

However, this is not predicted by the modulation transfer function, as the figures for the Raman-Nath and Bragg case in figure 4.13 are essentially identical in terms of the amplitude of the MTF. The slightly lower value for the peak MTF for a two micron grating can be explained as an effect of lateral currents, which will more effectively balance the potential difference between two neighbouring points. However, this is somewhat irrelevant as the LC responds not to the potential, but to the electric field which is proportional to $\Delta V_{\mathrm{LC}}/\Lambda$, a ratio which is almost constant.

We therefore look to the response of the LC to interpret the experimental response under Bragg conditions. The expression for the free energy of an LC system is reproduced here:

$$\tilde{\mathcal{F}}_d = \frac{1}{2}K_1[\nabla \cdot \hat{\boldsymbol{n}}]^2 + \frac{1}{2}K_2[\hat{\boldsymbol{n}} \cdot (\nabla \times \hat{\boldsymbol{n}})]^2 + \frac{1}{2}K_3|\hat{\boldsymbol{n}} \times (\nabla \times \hat{\boldsymbol{n}})|^2 - \frac{\epsilon_0 \Delta\epsilon}{2}(\boldsymbol{E} \cdot \hat{\boldsymbol{n}})^2. \quad (4.7)$$

The electrostatic energy term is effectively a constant, assuming a low dielectric anisotropy and given the invariance of $\Delta V_{\mathrm{LC}}/\Lambda$. However, as the grating spacing decreases, the elastic energy terms will increase as Λ^{-2} due to $\hat{\boldsymbol{n}}$ varying much quicker as a function of length parallel to the grating vector. Therefore under this simplistic analysis, we would expect the MTF to decrease considerably as we decrease the grating spacing applied to the cell.

Kubytskyi *et al.* have drawn a similar conclusion with a more robust phenomenological description of TBC in LC systems [95]. They first solve Maxwell's equations to find the field, given a sinusoidal modulation of the potential at the aligning layers, and the resulting field is applied to an LC. The modulation in the refractive index is then probed by two beams, and the resulting diffraction efficiency (the first order intensity of a single diffracted beam scaled by the incident intensity of same) is plotted as a function of the angle between the two writing beams. They find that the diffraction efficiency reaches a maximum, at which point increasing the bisector between the two beams will decrease the diffraction efficiency.

Two LC parameters are therefore key to obtaining a high modulation. Firstly, while the grating pitch ultimately limits the modulation, this can be mitigated by choosing an

LC with lower elastic constants to reduce the energy contributions of these terms. The wide availability of different LC materials due to their prevalence in the display industry would make this kind of selection easier than might be expected.

The second parameter is the conductivity of the LC, which can of course be predicted to some extent by performing a VTF measurement. The lower the conductivity, the larger effect lateral currents are going to have in balancing the modulation of the potential, although this can of course be mitigated by increasing the grating spacing.

Fortunately, this can be verified independently by considering the work of Sutherland *et al.* [96]. The LCLV design in this case is an LC layer sandwiched between two crystalline photorefractive windows. The electric field is modulated due to the creation of a static space charge distribution that forms in response to the inhomogeneous light field. In their system, stronger beam coupling is observed for LCs with a lower ionic content which is consistent with our predictions relating to lateral currents. In our system however, the electric field distribution is due to a voltage applied across the whole cell. Therefore, as an LC tends to infinitely low conductivity, the voltage drop will tend to be entirely across the LC, removing any beam coupling effect. It would be necessary to carefully control the conductivity of an LC to balance these two effects.

4.7.4.2 The effect of AC frequency

In the experimental maps shown in figure 4.10 two distinct beam coupling regions can be observed in the ± 1 order beam intensity. These regions occur at different driving frequencies: a thinner region centred at 10^{-2} Hz and a thicker one centred at $10^{1.5}$ Hz. We attempt to explain these separate beam coupling regions by looking at the conductive properties of the photoconductive layer.

PVK is a non-ohmic conductor, where the resistance changes depending on the voltage applied to it. In actual fact, there are two conductive regimes: one ohmic region at low voltages where the current density is proportional to the applied voltage, and one regime dominated by space charge limited current where the current density is proportional V^{m+1} where V is the applied voltage, and $m+1$ is dependent on the temperature of

the sample, and $m + 1 \sim 2$ at room temperature. These two regimes are measured and explained briefly by Lai *et al.* in reference [97], but the electronics of these kinds of systems will be discussed in far more detail in chapter 6, where alternatives to PVK:C_{60} are introduced.

For the purposes of this model, we can imagine that the conductivity of the PVK:C_{60} follows the approximate voltage dependence shown in the top part of figure 4.14. While it is possible to model the conductivity more accurately by considering the origin of the effect, it is not necessary for this approximate model of the modulation. Instead, the conductivity is simply modelled as having two ohmic regions, one at high voltage, and one at low, where the transition is a hyperbolic tangent function. The bottom part of figure 4.14 plots ΔV_{LC}, which is the amplitude of the voltage modulation at the interface between the LC and the PVK:C_{60} layer as a function of the frequency and voltage of the applied field. As such, it shows the same conditions plotted in figure 4.10

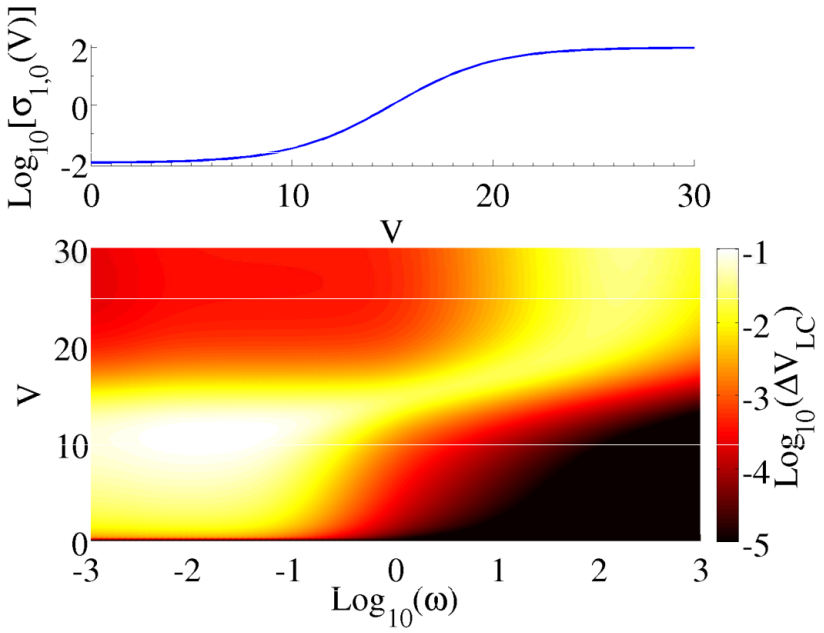

Figure 4.14: Top panel: an arbitrary function designed to represent two conductivity regimes for PVK:C_{60} as voltage increases. Bottom panel: The resulting voltage modulation at the LC/polymer interface as function of the applied voltage and the non-dimensional frequency.

It is immediately clear that the modulation calculated in figure 4.14 does not predict quantitatively the experimental beam coupling shown in figure 4.10. It does however have two distinct coupling regions, and can therefore be used to explain why two such

regions are observed experimentally. At lower voltages, the conductivity of the PVK:C_{60} layer is low, and the relative conductivity of the LC layer increases. We can see directly in figure 4.14, or by considering the relevant region in figure 4.13 that the beam coupling will therefore occur at a lower non-dimensionalized frequency than it would for the lower relative conductivity of the LC at higher applied voltages. We do indeed observe the high-frequency peak in figure 4.10.

Of course, the two peaks do not occur in the same experimental maps for E7 (figure 4.11). E7 is a much more conductive LC than TL205, and the relative conductivity will therefore be much higher at all applied voltages. Therefore, we may expect not to see the low-frequency beam coupling peak for an E7 cell until reaching lower frequencies than have been tested in this experiment. Of course, as the time period of the field increases, Debye charge layers will start to screen the voltage applied to the cell [32], so a model would have to include these layers to properly explain the behaviour.

4.8 Conclusions

The conclusions for the two experiments will be discussed separately, followed by a summary of how the techniques complement each other and the future direction for the work.

4.9 Discussion and conclusions for VTF results

A simple, multi-spectrum technique has been developed that uses an optical signal to characterize the electrical behaviour of an LC cell subject to a varying AC field, and the results have been interpreted using a physical model of the cell, based on interpreting the constituent layers as parallel RC circuits, and the time response of the LC as a low-pass filter. It has been shown that two time-constants, relating to the relative conductivities of the layers and the time response of the LC material can be measured by fitting theoretical data generated by the model to the experimental data. Furthermore, the

Frederiks transition can be measured as a function of the applied voltage frequency, and the affect light intensity has on this behaviour can be measured.

The measured high-pass filter time response, τ_{VTF} is equal to 1.24 s for E7, and is infinite in the case of TL205, although it should be noted that the TL205 result is certainly due to the fact that it was impossible to use voltage frequencies low enough to measure the value for TL205. A value for τ_{VTF} for E7 can be calculated using values for the dielectric constant of PVK and the conductivity of the E7, which results in a value of 0.6 s. While there is insufficient data to make the same calculation for TL205, there are references to the conductivity being two orders of magnitude lower than in E7 [83]. This is also supported by impedance measurements of cells containing these two LCs, as in [72], chapter 4. In this case, τ_{VTF} would be two orders of magnitude higher than for E7. Meanwhile, the measured low-pass filter time response is 0.7 s for each LC, and 2.9 s and 3.1 s for E7 and TL205 respectively

The values obtained from the model are inconsistent with calculated values from the literature. This suggests that the model is insufficient to predict the results of a VTF experiment. However, it is entirely possible that the model could be improved by separating the alignment layers, and by introducing effects such as the transient build up of charge layers at low frequencies - an effect described by Scalerandi *et al.* [46] where charge builds up over a time period of 15 s. What the model does allow is a powerful way of comparing the relative behaviour between two different cells. τ_{VTF} was measured to be at least twice as high in E7 as in TL205, and values for τ_T for both LCs were measured to be equal; both of these results are consistent with literature values. Therefore, one can conclude that modelling different LC systems measured by VTF can allow one to compare and contrast the conductivities and time response of the LCs involved.

The VTF has also been measured for photorefractive cells under varying light conditions in order to determine if there is a difference in the behaviour between cells in dark and light conditions. This should allow insight into the behaviour of cells in photorefractive experiments such as TBC, as the illuminating light in these experiments oscillates between low and high intensities. The intensities investigated in the experiment have been chosen to reproduce the intensities of dark and light fringes in TBC experiments.

The resulting plots for E7 show that there is a large difference in the Frederiks transition at light and dark illuminations, provided the frequency is sufficiently low (< 0.128 Hz). This is a useful method to determine at which voltage frequency photorefractive effects such as TBC are likely to be strongest. The refractive index change between the light and dark states must be highest where differences in the electro-optic response is seen in the light and dark VTF plots. There is no significant difference in the VTF plots for photorefractive TL205 cells in light and dark conditions, which leads to the conclusion that beam coupling should be much weaker in the case of TL205.

The VTF can be applied to systems beside the photorefractive devices described in this thesis. In particular, if the voltage drop across non-LC layers in an LC device plays a significant role in the device operation, then a VTF measurement is an excellent way to measure this drop. One example is the work by Komitov *et al.*, where ferroelectric LC polymers are used as electrically addressable alignment layers [48]; a measurement of the electric field across those layers would help to find the optimum driving voltage where the highest possible share of the voltage is dropped over these aligning films.

4.10 Discussion and conclusions for TBC results

The strength of the non-linear response of photoconductive polymer/LC light valves has been measured and modelled by considering the electric-field origin of the phase grating, which is probed with an optical field. The VTF can be used to measure the relative voltage drop across the LC layer as a function of the applied voltage and frequency, and under different illuminations in order to determine the effect an inhomogeneous light field would have on the cell. Two beam coupling has been performed while scanning the voltage frequency and amplitude, and a figure-of-merit, the modulation transfer function, has been devised and predicted in order to predict the experimental result.

The modulation transfer function is a measure of how much of the voltage can be transferred to the LC layer from the photoconductive layer. The non-dimensionalization allows one to apply it to any LC. The plots of the MTF predict the voltage required for

optimal beam coupling in systems with two different LCs, where the frequency predicted matches well with experiment.

The grating spacing has also been investigated, particularly as there is a large difference in the effect of Raman-Nath and Bragg regime beam coupling. Experimentally, it has been found that there is no significant beam coupling for lower grating spacing, which is not predicted by the calculation of the MTF, which, while taking a lower value for the smaller grating spacing due to the effect of lateral currents, does not account for zero beam coupling. Furthermore, the LC responds to an electric field, which scales with the inverse of the grating spacing, and hence does not change significantly. However, we have accounted for the effect by considering the elastic energy of the LC, which will increase due to the sharper gradient of the director field orientation at lower grating spacing, an effect which has been described in more detail in the literature.

Finally, the two distinct regions of beam coupling seen in TL205 cells has been described by the voltage dependence of the conductivity of PVK:C_{60} in contact with ITO. A simplified function of the conductivity is applied to the model in order to plot the voltage modulation as a function of applied voltage frequency and amplitude, and two regions are indeed observed. The model is not accurate enough to quantify the beam coupling in this way, but it does predict the main features of the graph, including the fact that E7, a more conductive LC, would not exhibit a second peak at the frequencies tested in this experiment.

For these systems, it is important to consider the balance between the conductivities of the layers when trying to optimize the non-linearities and hence operation as light valves. It is extremely important to keep the LC conductivity matched to within two orders of magnitude to that of the unmodulated photoconductor in order to prevent a low voltage drop across the photoconductor. It is also important to carefully tune the dark and light conductivity of the photoconductor such that it can be modulated to be higher and lower than the LC conductivity in the light and dark states respectively, and larger differences between dark and light conductivities will result in higher TBC efficiency. Further work on polymer tuning is discussed in chapter 6. The limitation on the grating spacing will always exist, although it can potentially be mitigated by

choosing an LC with lower elastic constants - a possibility considering the wide range of available materials.

The time-dependant beam coupling shown in figure 4.12 provides some important insight into the effect of different voltage signals on the PVK:C_{60} conductivity, and hence the beam coupling strength. Firstly, it is immediately clear that beam coupling is much stronger in the negative part of the cycle, labelled by C and D. This is clear evidence of the lower electron mobility with respect to the hole mobility in PVK, as shown in [88, 89, 76], and also of the difference in hole/electron acceptor levels in C_{60} [91]. These effects will cause the conductivity and photoconductivity of PVK:C_{60} composites to be affected significantly by the field polarity.

The second observation from figure 4.12 is that the beam coupling strength seems to reach a peak at a given voltage, and then decreases at the maximum voltage. This is very clear evidence for the reduced PVK conductivity at higher voltages [97], which would lead to a reduced beam coupling efficiency as shown by the solution to the MTF in equation (B.8). This result allows an interpretation of the beam coupling features seen in figure 4.11. For frequencies < 1 Hz, the beam coupling efficiency decreases with increasing voltage amplitude. At these higher voltages, a greater share of the voltage cycle is in the low-PVK-conductivity regime, and hence the average beam coupling strength over the entire cycle will decrease.

4.11 VTF and TBC as methods to characterize photoconductive polymer based LCLVs

Measurements of the VTF and TBC play different roles when being used to characterize LCLVs. A measurement of the VTF, and subsequent modelling will result in measurements of the relative conductivity of the photoconductor and the LC, as well as the time response of the LC (although the time response can be measured more accurately using the technique outlined in chapter 3). The next stage is to illuminate the cell with a varying intensity laser beam in order to measure the dark and light conductivity of the polymer with respect to the constant conductivity of the LC.

These relative measurements of the conductivities can be extremely useful when trying to determine a suitable new material, LC or polymer, for use in LCLV systems. E.g., a new polymer that exhibits a small variation in light and dark conductivity regimes would presumably be unsuitable in LCLV systems, as would an LC polymer combination with a very high or low relative conductivity, i.e. if the conductivities were 3 or more orders of magnitude different from each other. Therefore, the VTF should be used to determine at an early stage the viability of new materials.

The TBC measurement can be used to measure the optimum voltage frequency and amplitude to use in photorefractive applications. In this case, the model of the system is insufficiently accurate to reproduce the results of the TBC. However, it has given insight into what role the relative conductivities of the constituent layers, and the contrast between the dark and light conductivity of the polymer, have in determining the TBC gain and the frequency at which one would expect to see high TBC gain.

These experimental techniques can be used to characterise photorefractive devices that use any photoconductive material. Alternative materials are described in chapter 6. The next chapter 5 describes hybrid LC materials that, amongst other properties, are designed to increase TBC efficiency when used in these kinds of device.

Chapter 5

Multiferroic nanoparticle colloids

This chapter describes work investigating the effect of multiferroic, core-shell nanoparticles dispersed at low concentrations in a nematic LC host. It will be shown that such a colloid should display a lowered Frederiks transition in both magnetic and electric fields, as well as higher values for birefringence, dielectric anisotropy and photorefractive efficiency, paving the path for highly efficient electro-optic materials that can be switched remotely using relatively low magnetic fields.

Inorganic colloids in LCs have been studied extensively ever since the idea was posited by Brochard and deGennes in 1970 [98]. In this case, it was suggested that ferromagnetic grains could cause low-magnetic-field reorientation due to the interaction of the induced field in the grains with the diamagnetic anisotropy of neighbouring LCs. The main experimental challenge is achieving stable solutions, which cannot be obtained using the large grains reported on by Brochard and deGennes. More recent studies tend to use smaller nanoparticles coated with a surfactant designed to mimic the chemical makeup of LCs, the use of which has enabled low concentration stable suspensions of both ferromagnetic and ferroelectric nanoparticles [99, 37].

Both ferroelectric and ferromagnetic nanoparticles have a stronger coupling to the respective fields than nematic LCs. The magnetic response of LCs is particularly low due to their small diamagnetic anisotropy ($\Delta\mu$), and correspondingly large magnetic fields are required to switch samples [100]. If it were possible to address LC devices using

smaller electromagnetic coils, then it could remove the need for electrically conductive films, which are both cost prohibitive and interfere with the transmission of certain electromagnetic frequencies, particularly terrahertz radiation.

The layout of the chapter is as follows. A discussion of the theory of ferroelectric and ferromagnetic nanoparticle colloids in LCs will feature in the first section, with particular attention paid to the problem of obtaining stable suspensions, and what role particle size and surfactant layers can play. The section will finish by applying the same theoretical framework to core-shell multiferroic nanoparticles. The next section will relate how multiferroic nanoparticle suspensions were created, and the experimental characterisation that took place. Finally, the results will be analyzed to see if they show that multiferroic/LC suspensions are more sensitive to both magnetic and electric fields, and are therefore a viable technology for high-sensitivity magneto- and electro-optic devices.

5.1 Ferroelectric and ferronematic nanoparticle colloids

It has been known for quite some time that extremely high magnetic fields are required to re-orientate LCs, particularly when using aligning layers to create devices [31]. This is expected, as the diamagnetic response of most materials tends to be very low, certainly when compared to their dielectric response [101]. Interest in switching LC devices with magnetic fields has been maintained over the years, due to the relatively high cost of ITO electrodes, the lack of transparency across the EM spectrum of these same electrodes, and the possibility of switching devices remotely, paving the way for extremely compact switchable waveplates which need no electronic circuitry. Of course all this is achievable, but requires the use of large, heavy, expensive and non-portable electromagnets.

The first method to increase the magnetic sensitivity of LC devices was suggested by Françoise Brochard and Pierre de Gennes, who theorised that coupling between the magnetic moment of ferromagnetic grains and the LC director could in principle increase the magnetic sensitivity of doped LC mixtures [98]. Much theoretical and experimental work followed. For example, Burylov and Raikher extended the continuum theory of

Brochard and de Gennes to identify the nature of the coupling described above [102, 103]. The first so-called ferronematic suspension was created in 1983 by Chen and Amer [104], where the common nematic MBBA was doped with iron oxide needles of 500 nm length in a homeotropic cell. The stability of that suspension has been queried due to evidence of irreversible aggregation, and because the results have yet to be replicated [37]. More recently, the Burylov-Raikher theory has been extended to include diamagnetic switching of the LC, treating the coupling between the ferromagnetic moments and the LC molecules as small perturbations; a model that is well supported by experimental work [37].

Ferroelectric nanoparticles can have a similar effect on LC materials, albeit reacting to electric fields. The addition of ferroelectric nanoparticles to LCs has been theorised to increase the dielectric anisotropy of the undoped LC [99], thereby decreasing the electric Frederiks transition. In addition, it has been found that ferroelectric colloids exhibit a higher birefringence [105] and increased beam coupling efficiency [106] in photorefractive LC devices, which are discussed in chapter 6 of this thesis.

5.2 Core-shell multiferroic nanoparticles

Ferroelectric nanoparticles have been shown to significantly decrease the Frederiks transition of LC materials, due to an increase of the dielectric anisotropy [99]. At the same time, mixtures of ferroelectric nanoparticles with LCs show an increase in birefringence [105] and beam-coupling efficiency [106] in LCLVs. Meanwhile, Ferromagnetic colloids decrease the Frederiks transition in the magnetic field [98, 37], which could in theory lead to low-field magneto-optic switching - ~ 0.5 T would allow switching using rare earth magnets [107]. The motivation behind the use of multiferroic nanoparticle colloids is to develop a material that combines these properties. The main advantage would be the development of a versatile material that can be used in devices where ITO electrodes can be used, and in those where ITO electrodes cannot be used thanks to the cost opacity

Multiferroic materials do exist [108], but tend not to combine the ferroelectric and ferromagnetic properties that would be useful in an LC device (an example is bismuth

ferrite [109] which is both ferroelectric and *anti*-ferromagnetic). The alternative is to use some form of composite nanoparticle using a ferroelectric and ferromagnetic material. For this project, core-shell nanoparticles, as shown in figure 5.1, were used.

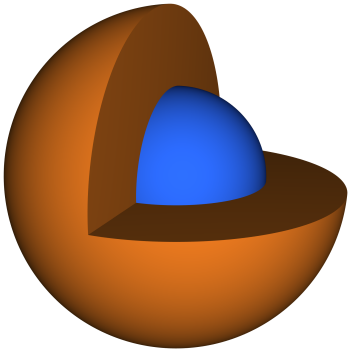

Figure 5.1: A generic core-shell nanoparticle with shell cutaway

In principle, core-shell multiferroic nanoparticles will combine the effects of ferroelectric and ferromagnetic particles. There is no interaction between the materials that would inhibit their interaction with their respective fields - cobalt ferrite will still magnetize and rotate under the application of a magnetic field, regardless of the fact that it is in contact with barium titanate. Coupling between the induced dipole in the nanoparticle and the LC director will remain, as will coupling between the director and the orientation of the nanoparticles. Provided that it is possible to maintain stable solutions, this is a viable method to create LC mixtures which combine the benefits of ferronematics and ferroelectric/LC colloids. The stability of LC/nanoparticle colloids is discussed in the following section.

5.3 Obtaining stable suspensions of nanoparticles in liquid crystal solvents

One of the key issues when attempting to create LC/nanoparticle suspensions is the fact that the inorganic nanoparticles tend to have a low solubility in the organic LC solvent [110]. The size, concentration and surfactant layers of nanoparticles all have to be considered when attempting to create such suspensions. Logically, a higher concentration

of nanoparticles will correspond to an increased effect, so the discussion in this section will focus on how to obtain the highest concentration suspensions possible by controlling the particle size and surfactant coating.

This section will describe two parameters which can affect the solubility of nanoparticles in LC hosts: the size of the nanoparticles, and the chemical structure of surfactant coating layers. The substituent nanoparticle material is assumed to have no affect on the solubility, as the chemical interaction between surfactant-coated nanoparticles (such as those investigated in this chapter) and the LC mesogens occurs only between the surfactant and the LC. Therefore, results from studies of gold nanoparticles will mainly be used to investigate these effects.

5.3.1 Effect of particle size on solubility

Soulé *et al.* [111] have put forward a model that computes the free energy of an LC/-nanoparticle colloid that includes the effect of nanoparticle size. In their case, the nanoparticles under investigation were made of gold, but the model is perfectly adequate for the case of multiferroic nanoparticles. The free energy consists of four terms: the isotropic mixing energy which considers the mixing energy of hard spheres in an isotropic liquid, two similar terms which account for nematic and crystalline ordering in the LC, and a term that accounts for interactions between the LC and the nanoparticles, particularly due to anchoring. The isotropic mixing term, f_{iso}, describes the effect of nanoparticle size on the solubility, and is given by:

$$\frac{\phi_{LC}}{v_{LC}} \ln\left(\phi_{LC}\right) + \frac{\phi_{NP}}{v_{NP}} \ln\left(\phi_{NP}\right) + \frac{\phi_{NP}}{v_{NP}} \frac{\left(4\phi_{NP} - 3\phi_{NP}^2\right)}{\left(1-\phi_{NP}\right)^2} + \chi a_{NP}\phi_{NP}\psi_{LC}. \tag{5.1}$$

The first two terms describe the entropy of the LC and the nanoparticles, where $\phi_i = N_i v_i / V$, i refers to the LC or NPs, v is the volume of the mesogen/particles, N_i is the number of particles, and V is the volume of the sample [112]. The third term is the Carnahan-Starling equation, which describes the mixing entropy of particles in a hard-sphere model, and is derived from the effect of the non-overlapping nanoparticle volumes [113]. The final term describes the surface interaction between the LC mesogens and the nanoparticles. χ_a describes the one-on-one interaction between the two materials (the

LC and the surfactant layer in this case), and $\psi_{LC} = \phi_{LC}a_{LC}/(\phi_{LC}a_{LC} + \phi NPa_{NP})$ is the area fraction of the LC - where a_i indicates surface area - and represents how likely it is that the nanoparticle is in contact with an LC molecule [114].

f_{iso} gets higher as the nanoparticle volume v_{NP} increases, leading one to conclude that larger nanoparticles increase the free energy and therefore the instability of the resulting colloid (nanoparticles can precipitate out of the LC if the system is unstable). This is confirmed by experimental observations made by Goodby *et al.*, where 5 nm gold particles were insoluble [115] in an LC host, whereas otherwise identical 2 nm particles were soluble in the same host [116]. Similar results have been obtained by Mirzaei, Shivakumar *et al* [117, 110].

5.3.2 The role of surfactant coatings

As has been mentioned, it has been postulated that the constituent material of nanoparticles dissolved in LCs plays no role in the solubility, as there is no significant chemical interaction between LC molecules and metallic surfaces. Instead, the interaction generally takes place between the LC molecules and a layer of surfactant bound to the surface of the nanoparticles, another quasi-epitaxial effect that possibly plays the most significant role in determining LC solubility.

This is a complex and poorly understood interaction, despite the wide range of experimental studies using various surfactants, nanoparticle sizes, and host LCs. In particular, there are no studies, apart from the original paper by Brochard and deGennes [98] that describe nanoparticles which are entirely insoluble in nematic LCs. Nevertheless, some observations have been made that can be helpful in selecting an appropriate surfactant.

The LC chemicals used in this investigation are defined as being polar, that is possessing a non-negligible molecular dipole due to the molecular geometry. Nanoparticles have a fairly high solubility in non-polar LCs, where relatively simple alkane-thiol nanoparticle functionalizations are sufficient to increase solubility, as shown by Mirzaei *et al.* [117] and Shivakumar *et al* [110]. Meanwhile, for polar LCs, the chemicals required to increase nanoparticle solubility need to be more complex. The ligands need to have a higher

polarity than the simple alkane-thiol structures required in non-polar solvents, as is noted by Brust *et al* [118]. Relevant work has been done in the earlier field of polymer-dispersed nanoparticles, where solubility is also a large issue: in this case, one needs a surfactant layer with a similar chemical structure to the repeating unit of the polymer [119].

Choosing a surfactant with a similar chemical makeup to the LC solvent is therefore essential to achieving high-concentration solutions of nanoparticles in LC solvents [120]. This was the most important control parameter in this investigation, and allowed solutions of nanoparticles of up to 0.2 % by weight as described in the following section 5.4

5.4 Development and characterization of multiferroic nanoparticle colloids in LCs

This section describes how core-shell multiferroic nanoparticle were dissolved into LC materials, and the resultant cell fabrication process. Finally, the experimental techniques that were used to characterise the cells are described, along with the predicted results.

The multiferroic nanoparticles were donated to us by the group of Ronald Ziolo from the Centro de Investigacion en Química Aplicada in Mexico, and are described in a paper by Corral-Flores *et al* [121]. The core consists of ferromagnetic $CoFe2O_4$ (cobalt ferrite, or CFO), and these nanoparticles are produced using a coprecipitation technique, where CFO is dissolved in a solvent, and then forced to precipitate out in nanoparticle form by the addition of a precipitating agent [122], which in the case of Corral-Flores' method was 5 M NaOH.

The ferroelectric shell was grown onto the surface of the CFO using a sol-gel technique [123], using $BaTiO_3$ (Barium titanate or BSO) as the ferroelectric material. Two samples were donated to this project - one where the nanoparticles consisted of 20 % by weight of CFO, and one with 50 % by weight of CFO with respect to the BTO weight. TEM images found in [121] show that the ferroelectric shell for the 80/20 nanoparticle varies

between 5 and 7 nm in thickness. The ferromagnetic nature of the nanoparticles was verified by measuring the magnetization as a function of applied magnetic field strength.

The nanoparticles were supplied in powdered form. The next stage of the project was to dissolve the nanoparticles into an LC host, resulting in stable LC/nanoparticle colloids; this is outlined in the next section.

5.4.1 Development of LC/nanoparticle colloids

Two nanoparticle samples were provided with different ratios of ferroelectric to ferromagnetic material. Sample 1 was in the weight ratio 80/20 BTO to CFO, while sample 2 was 50/50. The samples were supplied as dry powders. In order to mix the nanoparticles into the chosen LC, 10 mg of the nanoparticle powder were added to 10 cm^3 of acetone, and 9 mg of 4-n-Octyloxybiphenyl-4-carboxylic acid (OBPh) were added to the mixture. OBPh was used as a surfactant, which bonds to the surface of the nanoparticles via the $COOH$ group shown in the chemical structure in figure 5.2(a) [99].

The resulting solutions were sonicated for 30 minutes, and left to rest for 1 minute. The resulting solutions were then centrifuged at 2000 RPM for 1 minute in order to check that all of the two solutes had dissolved fully. Given that no sedimentation was observed at the bottom of the sample tube after cetrifugation, the conclusion was that the samples were fully dissolved. It is likely that a portion of the OBPh dissolved in the solution does not bond to the nanoparticle in this case, but the effect of non-bound OBPh on LC response has been previously investigated, and shown to be negligible [124].

A fixed amount of the solution was drawn off, and added to 1 g of E7, 6CB, TL205, and 18523 resulting in solutions with 0.1 % and 0.2 % of nanoparticles by weight. The LC solutions were mixed using a magnetic stirrer and heated to 40°C while under a constant nitrogen feed until the acetone had completely evaporated. After 4 hours the solvent was observed to have evaporated, although the samples were generally left for 12 hour periods in order to ensure that all traces of acetone had been removed.

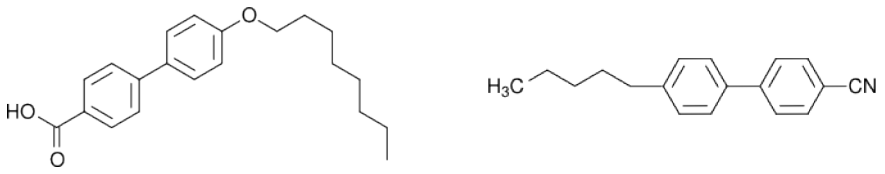

(a) (b)

Figure 5.2: Chemical diagrams of a.) OBPh and b.) 5CB, the most prominent component of the nematic LC mixture E7

As shown in section 5.3.2 the surfactant and LC used have to have a similar chemical structure in order to increase solubility, and therefore it was useful to investigate numerous LC solvents. 6CB was found to have a clearing temperature too close to room temperature, such that the heating effect of the coils in the magnetic characterization setup destroyed the nematic state. TL205 has proved to be an effective host for nanoparticle dopants in the past [105], but the suspensions using these nanoparticles resulted in large aggregates that did not dissolve in the LC. 18523 is a low-birefringence LC that, in a similar way to TL205, has proven to be an effective host for nanoparticles [105], and E7 is a common LC used in nanoparticle colloidal investigations: both were used in this investigation. The stability of the suspensions can be observed, as nanoparticles precipitating out of an LC solution leave a dark line at the meniscus. Therefore, it was determined that stable samples 0.1% by mass in E7 and 0.1%-0.2% in 18523 were obtained, and could be characterized in LC cells.

5.4.2 Cell fabrication

LC cells were produced as described in section 1.3, although it is important to emphasise some aspects of the process. ITO-coated glass slides were used as transparent electrodes. The slides were spin coated with PI, before being rubbed with a rotating cloth and fixed together using UV-curable adhesive mixed with Mylar spacer beads. The result was a layer of planar-aligned LC, where the final thickness could be controlled through the use of the spacer beads, and across which an electric field could be applied to re-orientate the LC molecules.

The thickness of the LC layer is important to consider when characterizing the LC response to a magnetic field. As $\Delta\mu \ll \Delta\epsilon$, an extremely high magnetic field. The

relationship between electric field and voltage leads to the electric Frederiks transition being thickness independent, while the magnetic transition is inversely proportional to the LC layer thickness as discussed in section 1.4.1:

$$H_c = \frac{\pi}{d}\sqrt{\frac{K_1}{\mu_0 \Delta\chi}}; \tag{5.2}$$

this was discussed briefly in chapter 1. Therefore, it is prudent to have a relatively thick LC layer ($\approx$ 50 μm) when characterizing the magnetic response in order to actually observe some response at an achievable low field value. Furthermore, it is not in fact necessary to use ITO coated glass for cells to be characterized in the magnetic field set-up, although it can be useful to check that the planar alignment has been achieved by using an electric field experiment.

5.4.3 Electrical and magnetic field characterization of LC/multiferroic nanoparticle colloids

The electrical and magnetic Frederiks transition were measured for the multiferroic nanoparticle colloids. This is an important parameter for LC applications, and the effect of the nanoparticles should be to reduce it in both cases [98, 99]. Furthermore, the birefringence of the materials should increase due to the ferroelectric material [105], and one should observe a magneto-optic effect below the Frederiks transition due to the ferromagnetic material [37].

The cells described in section 5.4.2 were characterized as follows. In order to test how the addition of nanoparticle colloids affected the field at which reorientation occurs, the director reorientation of the LC was probed optically as a variable-amplitude magnetic or electric field was applied: the CPI experiment described in chapter 2. The test was conducted in order to determine the effect of the nanoparticles on the field sensitivity, as well as to measure any change in birefringence or low-field ($<$ Frederiks transition) behaviour.

The angle between the initial polarization vector and the initial LC director is set to 45°, the analyzer polarizer is set to be orthogonal to this initial polarization, and the

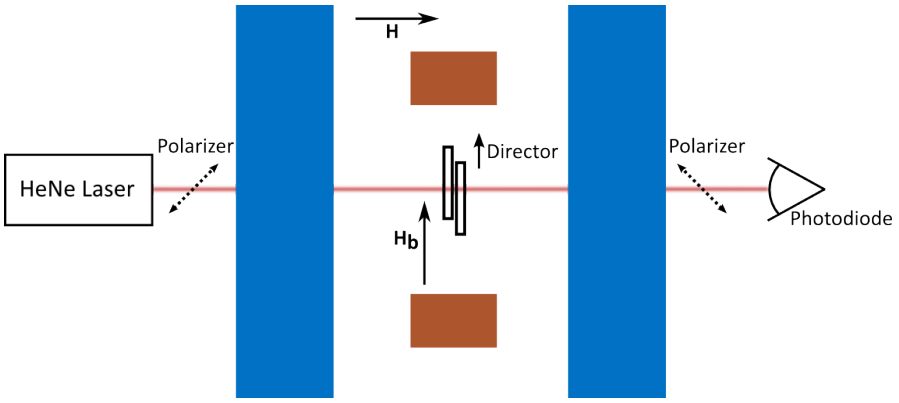

Figure 5.3: Experimental setup used to measur the magnetic Friedericksz transition, and low-field magneto-optic response of LC cells. The Helmholtz coils used to apply a field, $\boldsymbol{H}$, to the cell are shown in blue, and the smaller coils that apply the bias field, $\boldsymbol{H_b}$, are shown in red. Also shown are the initial LC director, and the crossed polarisers used in the experiment described in section 5.4.3.

resultant light intensity is measured using a photo-diode as the field is ramped up. The electric field used was an AC field with frequency 1 kHz output from an Agilent 33120A waveform generator, while the magnetic field was applied using a large pair of Helmholtz coils, which can achieve field strengths of up to 2 kOe. The magnetic field was measured using a Hall probe output to an NI USB-6501 data acquisition card, and the optical intensity was measured using amplified ThorLabs PDA25K photodiodes. In the magnetic field case, the voltage output from the photodiode was recorded using the same USB-6501 data acquisition card, while in the electric field case an NI6211 card was used.

A low-magnitude, non-varying bias field is applied to the cell throughout the magnetic field CPI experiment. The field is aligned parallel to the initial director, which is defined by the polymer rubbing direction. This field is important in ferromagnetic/LC colloids (ferronematics), as it reorientates the nanoparticles such that their magnetic moments lie parallel to the initial LC director, as shown by Burylov *et al.* [125], although Podoliak *et al.* were later able to show that this bias field can reduce the magnetic Frederiks transition even for undoped nematic cells [126]. The bias field was applied parallel to the initial director using two Helmholtz coils, with a magnetic field strength of 10 Oe. The geometry used is shown in figure 5.3.

In addition, the dielectric anisotropy was measured using a capacitance bridge as described in chapter 2 in order to check if the ferroelectric nanoparticles affected the dielectric constants of the material. Guard electrodes (section 2.3.2) were used in order to eliminate the systematic error that can occur in rectangular electrode cells due to the dielectric glue. The results of these characterization experiments are shown and discussed in the next section.

5.4.4 Clearing temperature of LC/multiferroic nanoparticle colloids

The clearing temperature of nanoparticle mixtures can often decrease due to a reduction of the order parameter; this effect is independent of the material makeup of the nanoparticle [127]. Therefore, the temperature transition was measured for the mixtures.

The completed cells were loaded into a Mettler Toledo HS82 hot stage, which has a viewing window. The hot stage was fixed onto the viewing stage of an optical microscope with polarizing optics, and the sample was viewed between crossed polarizers. The temperature was initially set to 10°C below the data sheet value for the clearing temperature for the material: 61, 87.4 and 55 for E7, TL205, and 18523 respectively [85]. The temperature was then ramped up in 0.5°C increments, and held at each temperature for 30 s. Once the sample was observed to turn dark, it was concluded that the isotropic state had been achieved, and the temperature was recorded. The experiment was then repeated starting from a temperature 2°C below this recorded temperature, and the resolution increased to 0.1°C.

This transition is not easy to observe, as different parts of the sampled area may undergo transitions at different temperatures, even when the temperature is held steady for a long period of time. Therefore, in order to be consistent between measurements, the temperature at which over 80% of the observed area was in an isotropic state was recorded as the clearing temperature - a DSC trace would be required to accurately measure the transition as discussed in section 2.2. The experimental error was around ±0.5°C.

5.5 Results and discussion of characterization of LC/multiferroic nanoparticle colloids

The following sections describe the results of the clearing temperature measurements, the electrical CPI experiment, the measurement of the dielectric anisotropy, and the results of the magnetic CPI experiment for multiferroic nanoparticles doped into E7 and 18523.

5.5.1 Results of clearing temperature measurements

Table 5.1 shows the measured clearing temperatures for each material. The predicted values for the undoped 18523 and E7 materials are from the Merck datasheet [85]: 55°C for 18523 and 61°C for E7. Large aggregates of $\sim$ 1 μm diameter were observed for TL205 mixtures, and the results are therefore not shown here. However, the aggregates were probed with a permanent rare-earth magnet in order to test the ferromagnetic behaviour, and were observed to move when in close proximity to the magnet.

Mixture	Measured clearing temperature
18523 + 0.1% 50/50	53.0
18523 + 0.2% 50/50	50.4
18523 + 0.1% 80/20	52.8
18523 + 0.2% 80/20	53.4
18523 Undoped	54.2
E7 + 50/50	59.1
E7 + 80/20	59.0
E7 Undoped	59.7

Table 5.1: Measured values for the clearing temperature in LC/multiferroic nanoparticle colloids. All temperatures have units of °C. The error in clearing point values is described in section A.3, and is equal to ±0.5°C in each case.

5.5.2 Results of electric characterizations

The intensity of light passing through doped E7 samples between crossed polarizers, along with an undoped E7 cell for reference, are plotted in figure 5.4. The samples were both doped at 0.1% of either 50/50 or 80/20 nanoparticles as described in section 5.4. The data have been normalized, and background noise measured and subtracted. The temperature of the lab for each of the experiments was $24° \pm 0.5°$, although the temperature fluctuations for the cell due to the coils was much higher, which is a source of error discussed in section 5.5.3.1.

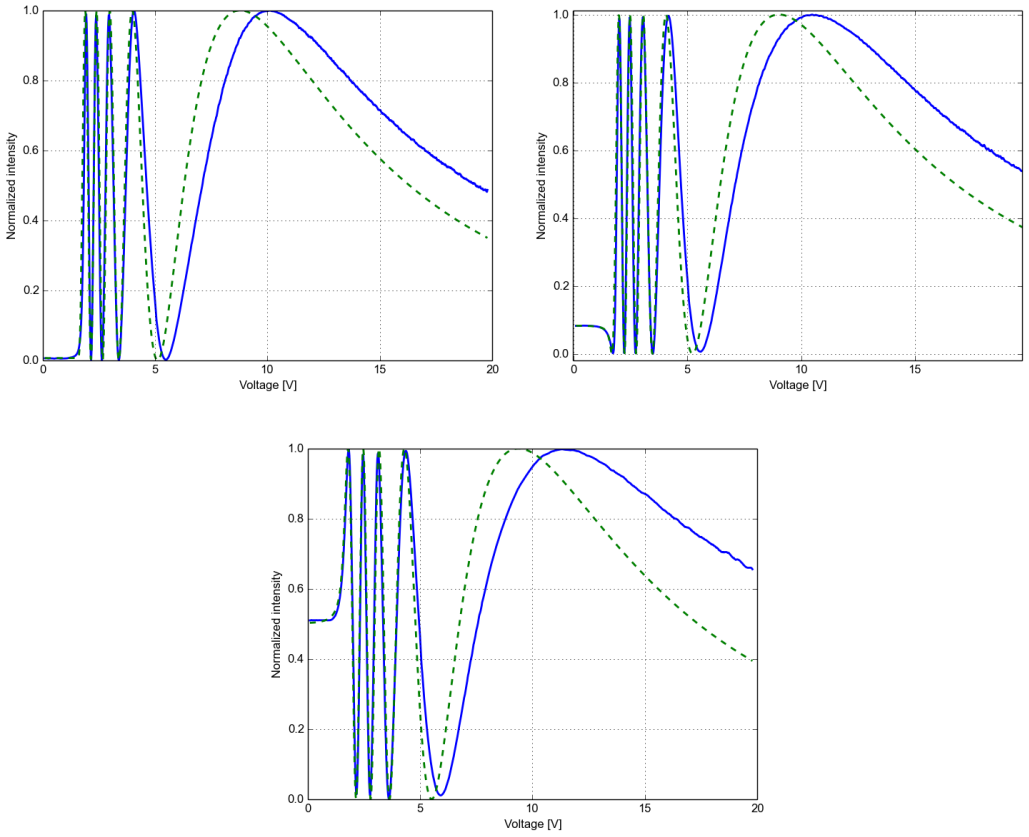

Figure 5.4: The intensity output for the CPI characterization of MFNP doped E7, with a control undoped sample. Clockwise from top left, the graphs show experimental (solid blue line) and theoretical (dashed green line) for E7 doped with 50/50 nanoparticles, 80/20 nanoparticles and the undoped sample.

The theoretical fits shown in the graphs in figure 5.4 are obtained using the same procedure outlined in section 3.7, using the elastic constants and pre-tilt as fitting parameters. The birefringence can be calculated using the method described in section 2.4.1.1 given

that the thickness of the empty cells was measured using the spectroscopy technique described in section 2.1.

The Frederiks transition is theoretically defined as the point at which a uniform solution for equation (1.17) becomes unstable under small perturbations, and a non-uniform solution is required instead. This point does not exist for the case of non-zero pre-tilt, as is clear from the gradually varying intensity around the transition point at 1.5 V in the graphs shown in figure 5.4. In this case, the procedure for measuring the Frederiks transition is to calculate it using:

$$V_c = \pi \sqrt{\frac{K_1}{\epsilon_0 \Delta\epsilon}}, \tag{5.3}$$

but this is not valid in this case thanks to the fact that $\Delta\epsilon$ can change due to the addition of ferroelectric nanoparticles. Therefore, the Frederiks transition in each case was measured by eye as being the point at which the gradient of the intensity curve started to change for the plots in figure 5.4.

The results for birefringence, as well as the fitted values of K_1, K_3 and pre-tilt are shown in table 5.2.

Mixture	Birefringence	K_1 $[10^{-12}$ $N]$	K_3 $[10^{-12}$ N]	Pre-tilt [○]
E7 + 50/50	0.206	4.4	7.3	0.3
E7 + 80/20	0.198	4.8	6.9	1.7
Undoped	0.197	5.0	10.4	3.3

Table 5.2: Calculated values of birefringence, and fitted values for $K_{1,3}$ and pre-tilt for MFNP doped E7.

The corresponding graph for 18523 is shown in figure 5.5. The cell thickness, birefringence and fitted constants for 18523 are shown in table 5.3.

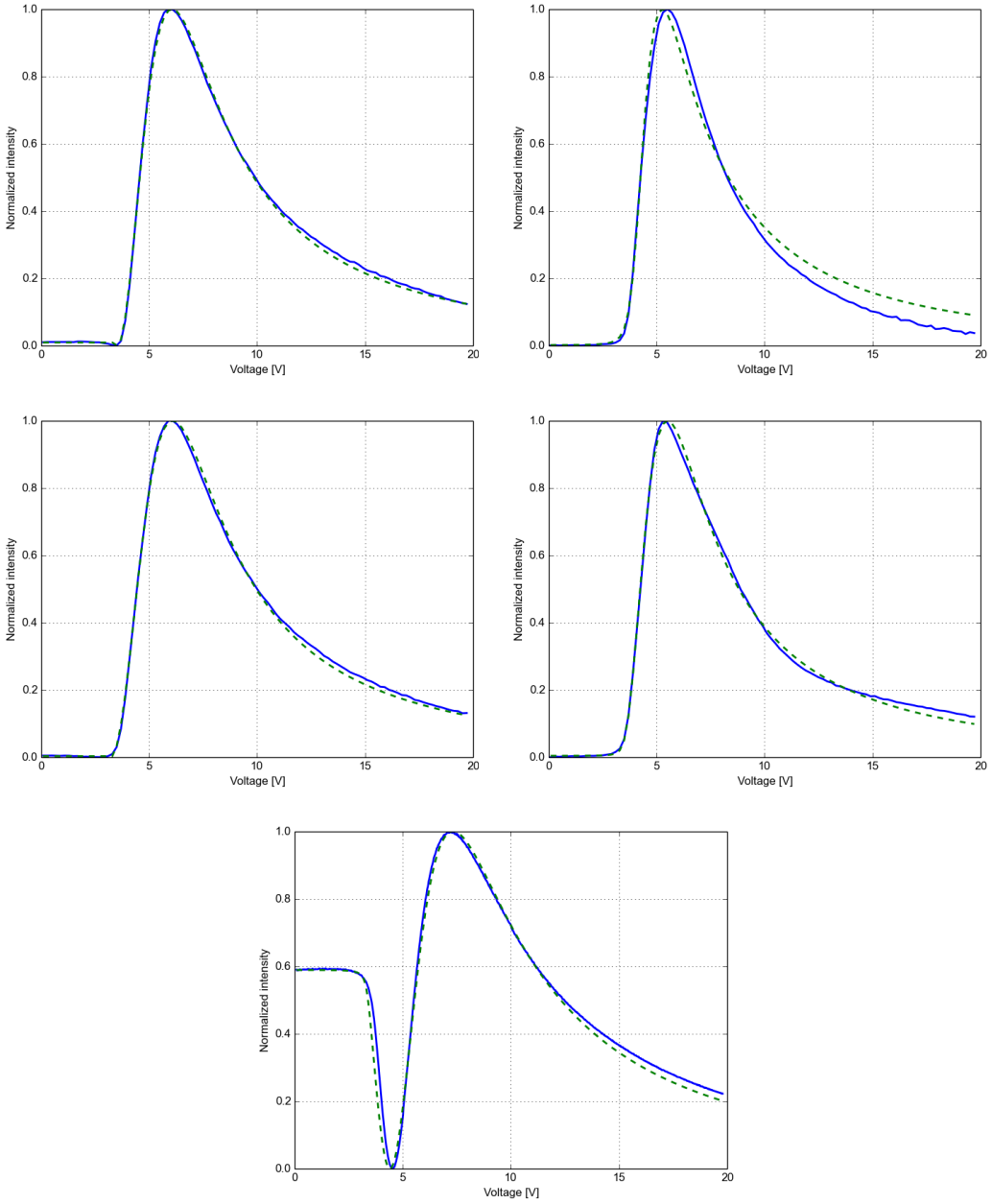

Figure 5.5: The intensity output for the CPI characterization of MFNP doped 18523, with a control undoped sample. The top and bottom row show the graphs for 50/50 and 80/20 suspensions respectively, and the left and right-hand columns correspond to doping at 0.1% and 0.2% concentration of nanoparticles by weight respectively. The bottom graph is for undoped 18523. The experimental values are shown by the solid blue lines, and the fit by the dashed green lines.

Mixture	Birefringence	K_1 [10^{-12} N]	K_3 [10^{-12} N]	Pre-tilt [$\circ$]
18523 + 0.1% 50/50	0.043	3.6	6.3	0.0
18523 + 0.2% 50/50	0.042	5.1	2.6	10.0
18523 + 0.1% 80/20	0.040	3.0	7.8	0.0
18523 + 0.2% 80/20	0.042	4.0	4.5	4.3
Undoped	0.047	3.6	7.7	1.7

Table 5.3: Calculated values of birefringence, and fitted values for $K_{1,3}$ and pre-tilt for MFNP doped 18523.

The final electrical characteristic to be investigated was the dielectric anisotropy of the suspensions, the results of which for E7 suspensions are shown in figure 5.6.

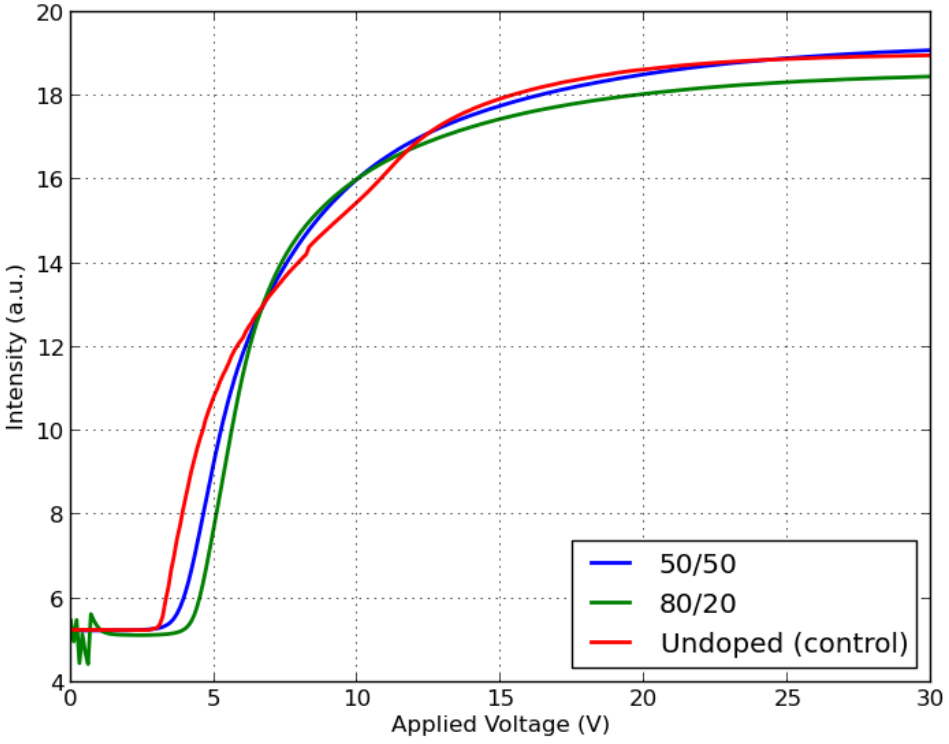

Figure 5.6: Dielectric constants of E7 suspensions under application of a DC aligning field

The equivalent 18523 cells were not constructed using guard electrodes, making it impossible to separate the effect of the glue from the effect of the LC when measuring the dielectric constants of the cell. A calculation of the dielectric anisotropy based on the

fitted value for K_1 and an estimated value of the Frederiks transition shall be discussed in section 5.6.

In figure 5.6, we see essentially no change in the values for $\epsilon_{\parallel}$ or $\epsilon_{\perp}$ for the doped and undoped mixtures. The values match well with the literature values for E7. Therefore, we have to conclude that if nanoparticles are dispersed in the mixture, then they are not ferroelectric, or at the very least that there is no coupling between induced ferroelectric dipoles in the nanoparticles and the LC director (there is no physical explanation for the second statement).

5.5.2.1 Errors in electrical characterizations

In this section, the sources of error in the electrical characterization are discussed, as well as the effect in the measurements quoted in the previous section.

In order to conclude from the values for Δn shown in table 5.2, a value for the error is required. The largest magnitude contribution to the error comes from the thickness measurement of the cell, as the thickness will not be uniform across the cell. Although care is taken to measure the crossed polarized intensity and the thickness in exactly the same place, it is still reasonable to expect an error in the measurement of the thickness of ± 0.4 μm, which given the equation for birefringence ($\Delta n = \frac{\delta\lambda}{2\pi d}$) means that the error in the measured birefringence is $\pm \sim 0.03$ (this is discussed in more detail in section A.2). This in turn allows us to conclude that the birefringence of E7 has not been altered outside of the uncertainty range due to the addition of MFNP.

The error in the estimation of the Frederiks transition is difficult to quantify exactly, as the Frederiks transition is estimated from the plots by eye. There is some voltage range within which this change occurs, and the Frederiks transition could fall anywhere in this range. The range over which a transition can definitely be said to take place is 0.3 V, which is obtained by observation of the traces in figures 5.4 and 5.5 - this is the smallest range required to ensure that the intensity is in fact changing, indicating a transition.

The errors in the measurements of the elastic constants can be calculated in the same way as for the CPI experiment in chapter 3. The error analysis is discussed in more

detail in section A.4.3. However, it was not possible to complete this analysis within the project timescale. Therefore, conclusions based on these elastic constant measurements will be speculative, and require more rigurous error analysis in the future. The dielectric constant errors described in section A.4, and are 4 orders of magnitude smaller than the recorded dielectric constants - they are therefore assumed negligible.

5.5.3 Results of magnetic characterizations

Again, the E7 and 18523 suspensions were tested independently by placing them between crossed polarizers and measuring laser transmission through the system as a function of applied field strength. It has been mentioned needed to induce a response in a nematic LC are extremely high, and a large electromagnet was required to reach the necessary fields, a consequence of the typical values of $\Delta\mu$. In fact, it was found in the case of 18523 that the field required to cause the LC to begin reorientation was $>$ 1800 Oe, which is higher than the measurement range of the hall sensor used in this experiment. Reorientation couls be observed by measuring the intensity signal on an oscilloscope while increasing the field beyond 1800 Oe, but the results cannot be presented here without a higher range Hall probe. Conversely, it is possible to see a magnetic response in undoped E7 providing that the cells are thick enough: 50 μm in this case. The results for E7 are shown in figure 5.7.

It is immediately obvious from figure 5.7 that the magnetic measurements are inherently less accurate than corresponding electrical measurements. This is due in part to the higher temperature due to the magnetic coils (and furthermore the possible shifts in temperature of the nematic mixtures), as well as an inherent lack of stability of the applied fields; the magnetic field strength will be affected by temperature and current fluctuations as well as any nearby metallic or electrical sources.

Estimating the Frederiks transition is necessary in the magnetic field case, as it is not possible to measure $\Delta\mu$ with the available equipment. The noisy signal made this measurement very difficult in the undoped case, and there is a predicted low-field response in the doped cells, which makes the Frederiks transition impossible to estimate in those

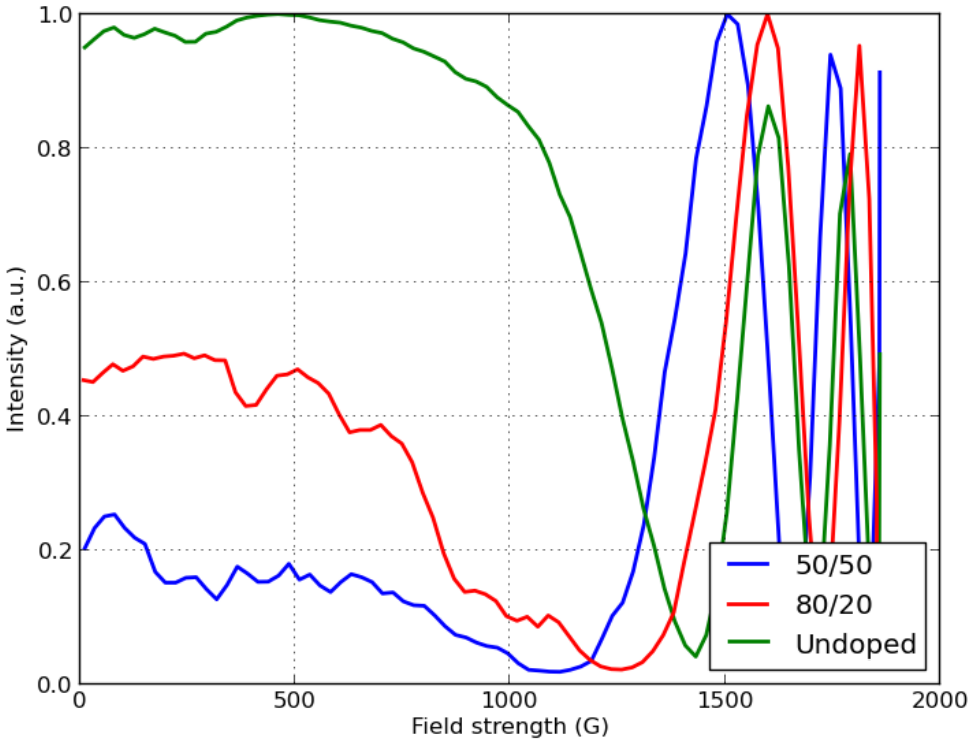

Figure 5.7: The effect of increasing magnetic field magnitude (measured in Gauss) on the optical retardation in E7 suspensions.

cases. The birefringence and elastic constants were identical to those shown in table 5.2, as the mixtures were the same in both cases.

5.5.3.1 Errors in magnetic characterizations

In this section, the sources of error in the electrical characterization are discussed, as well as the effect these errors have on the measurements quoted in the previous section. It is immediately clear from the data seen in figure 5.7 that the noise is significantly higher than measuring the CPI in an electric field, and this will be a significant contributor to the errors involved.

The variation in intensity seen in the traces in figure 5.7 will have two contributions - one from scattering effects due to large nanoparticle aggregates, and one due to heating effects from the magnetic coils which will affect the birefringence as described in section 1.2.1.

A scan measuring the intensity transmitted through the experiment with no voltage applied to the cell would allow a measurement of the contribution of scattering to the noise, as this effect is field-independent. This experiment was not performed due to time constraints. The measurement of the CPI for the undoped cell should allow one to estimate the error due to the heating effect of the coils, as there can be no scattering aggregates in this cell. The noise value can be estimated as the range of the intensity values measured while the field is below the Frederiks transition. For the undoped sample, this random error is 5.6%, and the error for the doped samples is 8% for the 80/20 sample, and 18% for the 50/50 sample. Without further investigation into the heating effect, it is impossible to speculate the physical origin of this error, but the values can be used to estimate the error in the measured values of birefringence.

The Frederiks transition was not given a value in this experiment, as the transition itself is not sharp enough to reliably extract a value. However, the field strength at which the LC reorientates can be compared between the samples, giving an idea of the relative transition. In other words, it should be possible to order the LC mixtures from lowest to highest Frederiks transition. In order to incorporate the error, the field at which the intensity changes by more than the quoted error values is used as a rough estimate of the transition, and these estimates can be used to compare between the different mixtures.

5.6 Conclusions from the resultant characterization of LC/-multiferroic nanoparticle colloids

There are several effects one would expect to observe if multiferroic nanoparticles have been well dissolved in an LC host. These effects are a lower electrical and magnetic Frederiks transition, a higher dielectric anisotropy, a higher birefringence, and higher beam-coupling efficiency in photorefractive systems. These effects are due to the interaction between the LC and ferromagnetic/ferroelectric characteristics of the nanoparticles. The experiments characterizing colloidal systems in E7 and 18523 were designed to verify all of these possible outcomes, apart from the increased beam-coupling efficiency.

This conslusions section focuses first on the electro-optic characterization, and then on the magneto-optic.

5.6.1 Electro-optic characterization of MFNP colloids

As stated in section 5.5.3.1, it was impossible to complete the error analysis for the measurements of the elastic constants. These conclusions will therefore be restricted to identifying general trends, and it is assumed that further error analysis is required to confirm the accuracy of the elastic constant measurements.

The Frederiks transition for a cell with non-zero pretilt is impossible to define exactly, but the point at which the LC starts to respond to a field can be estimated from the CPI plots shown in figures 5.4 and 5.5, and in each case there was no significant change in the transition. The errors on this estimation are fairly large thanks to the effect of the pre-tilt, which adds a significant curve to the intensity behaviour around the transition. The error on this estimation is approximately $\pm 0.3\ V$ (see section 5.5.3.1), which in turn means that all of the estimated Frederiks transitions for the E7 cells are within error (the values are 1.45. 1.36 and 1.23 V for the 50/50, 80/20 and undoped cells respectively). An alternative method for calculating the Frederiks transition is to use the measured values for K_1 (table 5.2) and $\Delta\epsilon$ 5.6 in the equation:

$$V_c = \pi \sqrt{\frac{K_1}{\epsilon_0 \Delta\epsilon}}, \tag{5.4}$$

which can still be used to estimate the transition point, despite the fact that it is not physically descriptive for non-zero pre-tilt. Using this definition, the values for the Frederiks transition are 1.52, 1.49 and 1.53 V for 50/50, 80/20 and undoped mixtures, where the discrepancies can easily be accounted for by the effect of pre-tilt.

Therefore, it is valid to conclude either that the dipolar electric field present in the nanoparticles is not being coupled to the dielectric anisotropy of the LC mesogens, the nanoparticles are not ferroelectric, or that the nanoparticles are not in fact present in the mixture. The change in K_3 in the mixtures, along with the absence of an observable dark-colored precipitate in the samples verifies that the nanoparticles have been

successfully dissolved in the LC mixture [124]. Given this fact, it is extremely unlikely that the nanoparticles are not coupled to the LC director as the same materials have been investigated previously [128, 37], and the most likely conclusion to draw is that the nanoparticles are not ferroelectric. This will be discussed in more detail after the results for 18523 and the magnetic characterization of the E7 colloidal systems have been analyzed, as these results support the conclusion still further.

There is an anomalous result for the mixture of 18523 with 0.2% 50/50 nanoparticles. This is clear from the fitted values of the pre-tilt (10°) and K_3, which is lower than K_1; both results are very unlikely when compared to the other 18523 cells and typical values in the literature [129, 31, 15]. This discrepancy may be explained by formation of aggregates, where the nanoparticles coalesce to form large particles, which can lead to severe disinclinations in the LC alignment, as well as potential interference with the chemical interactions at the boundary which will affect the pre-tilt. The results for this cell are discarded when drawing conclusions.

The Frederiks transition in the 18523 cells was not observed to change significantly in the plots in figure 5.5. The discrepancies in the estimated Frederiks transition can be explained by the large errors in the estimation, and the small changes in K_1, and do not constitute evidence of an increase in $\Delta\epsilon$ Furthermore, while there is a change in the birefringence of the mixtures when compared to the undoped case, the behaviour is the opposite to that predicted: the birefringence decreases when nanoparticles are added.

One can draw two conclusions from these observations. The changes in the elastic constants, as well as the reduced birefringence in the case of the undoped 18523 all suggest that nanoparticles are present in the system. Nanoparticles can affect the order parameter of LCs [127], and changes in the order parameter will lead to changes in the elastic constants of the system [20]. These order parameter changes can also account for the difference in birefringence of the 18523 samples. The presence of the nanoparticles is also confirmed by the magnetic measurements, as discussed below, and by the fact that no precipitate was observed in the mixtures after the nanoparticles were added to the LC hosts.

The second conclusion is that the nanoparticles do not exhibit ferroelectric behaviour. The fact that there is no evidence of an increase in birefringence or dielectric anisotropy is evidence of this fact, given that the nanoparticles are clearly present in the mixture. Experimental verification of the lack of ferroelectric behaviour was confirmed by Jean-Françoise Blach of Unité de Catalyse et Chimie du Solide by attempting to harvest MFNP dispersed in a solvent, a technique that involves using a shaped electrode that can generate large electric field gradients, as described by Cook *et al* [130]. As predicted by the LC experiments described here, he was unable to harvest any of the nanoparticles, confirming that the ferroelectric effect is not present.

The thickness of the ferroelectric shell may explain why the nanoparticles lack a ferroelectric response. The nanoparticles synthesized are reported as having a range of radii between $15 - 28$ nm [121]. This in turn puts the diameter of the ferroelectric layer far below that of a critical size, below which the liquid and crystalline states are indistinguishable. In this state, ferroelectric behaviour cannot exist. This critical diameter is given by $D_0 = \sigma_{90}/(2\kappa\alpha\beta^2)$ with σ_{90} and α denoting the density of 90° domain walls and the material's elastic stiffness respectively. κ is a fitting parameter, and β is the ratio of material lattice constants (the derivation is explained in detail in [131]). The value for D_0 in barium titanate is 40 nm, meaning that the ferroelectric layer is certainly too thin to exhibit any ferroelectric behaviour. Some studies have shown that smaller nanoparticles of BTO can exhibit ferroelectric behaviour, notably a study by Rudzki *et al.* where the size dependence is investigated, but in these cases milled nanoparticles are used [132]. The milling process could induce surface stresses which lead to ferroelectric behaviour, although this is speculative at this point. In any case, the sol-gel process has never been used to successfully fabricate sub-40 nm particles which exhibit ferroelectric behaviour.

5.6.2 Magneto-optic effects in MFNP colloids

The magnetic field results show a low-field (below Frederiks transition) response, which is strong evidence for the presence of ferromagnetic nanoparticles in LC colloids as shown by Podoliak *et al.* [37], and is due to coupling between the ferromagnetic particles and

the LC director. The ferromagnetic particles can respond to significantly lower fields than the LC mesogens, and therefore one would expect to see some LC rotation at low fields. At the same time, direct coupling between the field and the diamagnetic anisotropy of the LC is responsible for the Frederiks transition like behaviour seen at 1000 G in all samples - of course it is essentially impossible to assign a value to this transition.

The field value at which the measured intensity in the magnetic CPI experiment changes more than the errors (described in section 5.5.3.1) can be used to roughly compare the Frederiks transition of the mixtures. The field values are 800 G for the undoped sample, 720 G for the 80/20 sample and 1000 G for the 50/50 sample. The first two values support the conclusion that ferronematic suspensions have been achieved, while the 50/50 sample is anomalous. The error is much higher for this sample, which may explain why the method of incorporating the error in the intensity into this measurement has given such a high comparison value. These values are inconclusive, but provide weak evidence that ferronematic samples have been achieved.

The fact that the nanoparticles are ferromagnetic is further confirmed by particle aggregates in TL205 that were observed to be ferromagnetic under a polarised microscope, and the action of a permanent ferromagnet. Furthermore, Corral-Flores *et al.* [121] confirmed the ferromagnetic nature of the nanoparticles using magnetometry techniques.

Clearly, these nanoparticles are not in fact multiferroic, and new batches would need to be made before multiferroic/LC colloids could be realized. These batches would either need to use $BaTiO_3$ layers thicker than 40 nm, or to be processed using a milling process in order to induce surface stress. The principle is still sound, and preliminary results in this report suggest that the ferromagnetic core means that, in the absence of an electric field, multiferroic colloids behave in the same way as ferromagnetic colloids: an encouraging conclusion for future work involving this type of nanoparticle.

The nanoparticles seemed to have an effect on the order parameter and hence elastic constants of the material, which may need to be studied in more detail using electrically and magnetically passive nanoparticles, e.g. silica; understanding the elastic effect of the nanoparticles is crucial to predicting switching behaviour, as well as time response. It

would furthermore be of interest to measure the rotational viscosity of these equivalent colloids in order to calculate an exact vale for the time constant: an important parameter when evaluating device performance.

The achievement of stable multiferroic nanoparticle colloids in LCs is achievable, resulting in versatile materials for applications in electric and magnetic field switching applications. One of the uses of such a material would be in photorefractive systems, which have been discussed in some detail in this thesis. The following chapter 6 describes other material options that can increase the strength of the photorefractive response in such systems.

Chapter 6

New materials for liquid crystal light valves

This chapter describes experimental work developing and characterizing a series of LC light valves (LCLVs) that use new materials, either as replacements for PVK:C_{60} or in order to enhance the photorefractive effect due to PVK:C_{60}. Three materials have been investigated: a conductive polymer known as PEDOT which theoretically can reduce the charge injection barrier present between ITO and PVK:C_{60}; a photorefractive polymer known as JTDA16, which can replace a PVK:C_{60} layer; and PAAD, a photoaligning polymer which can be used to enhance the modulation depth of the induced index grating due to PVK:C_{60}. The chapter will start by outlining common characterization techniques performed on LCLVs, and describe which parameters can be measured. The background to the new materials is then discussed, along with the motivation for their use in LCLVs. Finally, the experimental work performed on these LCLVs will be described in detail, and the resulting characterization results analyzed.

6.1 Liquid crystal light valves

A liquid crystal light valve (LCLV) is a composite device where the alignment of an LC layer is a function of light intensity incident on a neighbouring material, or sometimes on the LC itself [133]. LCLVs that use a layer of PVK:C_{60} in order to optically modulate

the refractive index have been described in this thesis, in particular sections 2.6 and 2.7, where TBC and diffraction efficiency experiments are outlined, and chapter 4 where the VTF and AC TBC is applied to this type of LCLV. However, the discussion in this chapter focuses on enhancing or improving PI-PVK:C_{60} cells using different and more exotic materials and geometries that have been developed as part of this project.

Typically, the layer neighbouring the LC is a photoconducting semiconductor layer, such as amorphous silicon [134], $Bi_{12}SiO_{20}$ (BSO [49]), gallium arsenide [135] or organic alternatives such as the aforementioned PVK [78]. One can also use layers made from photorefractive crystals [136], layers that have a photoaligning effect on LCs [137], or layers containing a photothermic material such as gold nanoparticles [138]. The mechanism responsible for the photorefractive LCLV behaviour is somewhat different in these cases, and as always there are significant advantages and disadvantages to each.

When designing an LCLV, one must be mindful of the following considerations: time response, wavelength sensitivity, strength of photorefractive response (characterized by gain as described in chapter 4), maximum resolution, signal attenuation due to absorption and scattering, and optical nonlinearity. The time response and maximum resolution are mostly due to properties of the LC, namely rotational viscosity and elastic constants. Signal attenuation, gain and optical nonlinearity can be due to the photoactive element or the LC material (although the losses in an LC are generally low) or indeed a combination of the two, and the wavelength sensitivity tends to be entirely due to the photoactive layer.

When discussing TBC in this thesis, the mechanism by which conductivity is modulated in the photoactive layer has been ignored. When exploring new materials, it becomes important to think about this mechanism in more detail in order to determine how the parameters listed above are affected. This chapter will focus on characterizing the photorefractive gain in LCLVs using new materials, but future work can focus on measurements of the other parameters.

6.2 Measuring figures of merit in LCLVs

Figures-of-merit can be used to characterize the parameters of photorefractive systems, and to compare these parameters between different systems. In addition, certain systems may have functionality beyond a simple photorefractive effect, such as the voltage-tunability of LCLVs and photorefractive polymers [90]. The photorefractive gain is the only figure-of-merit measured for the LCLVs developed as part of this project, but other figures-of-merit shall be discussed briefly, as future work will focus on these measurements.

6.2.1 Spatial resolution of photorefractive systems

The most exciting potential applications for LCLVs are arguably dynamic hologram storage [139] and coherent image amplification [52]. Both of these processes are limited by the spatial resolution of the LCLV being used, and it is therefore important to determine a figure-of-merit for the resolution, as well as an accurate method of determining it.

Spatial resolution can be measured when imaging a series of dark lines, and is a measure of how many such lines can be seen in a given image length; the units are generally given as line pairs per millimetre (lp/mm). However, it is generally not sufficient to measure the spatial resolution, as the image of the line pairs can be extremely blurry, which would amount to a loss of spatial information when considering light valve applications. Therefore, it is more useful to plot the resolved spatial resolution against the optical modulation transfer function (OMTF), given by:

$$OMTF = \left\langle \frac{I_{\max} - I_{\min}}{I_{\max} + I_{\min}} \right\rangle, \tag{6.1}$$

where $I_{\min,\,\max}$ are the minimum and maximum intensity measured across a profile, which will generally include a series of lines in order to improve accuracy. As the spatial resolution of the imaged lines increases, the OMTF will generally decrease in any imaging system.

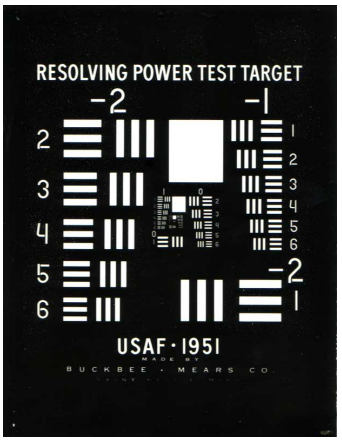

Figure 6.1: The 1951 US air force test target, still in use today as a test of spatial resolution. Reproduced under a creative commons license [140]

The spatial resolution of any imaging system is often measured using a chart such as that shown in figure 6.1, which uses transparent line pairs and a light source to be imaged by the device in question. The resolution of the smallest pattern that can still be resolved by eye in the resulting image is given as the maximum resolution of the device.

Bortolozzo *et al.* describe an alternative method in [141], where an optical feedback scheme is used to generate a hexagonal pattern (the origin of which is described for a Kerr medium by D'Alessandro and Firth in [142]). In this case, the spatial resolution itself can be controlled by varying the propagation length of the beam in the feedback loop, and the OMTF measured using a CCD camera.

6.2.2 Time response of photorefractive systems

The time response of a photorefractive system is important, as it can limit applications, in particular when the system is used for signal processing, e.g. coherent image amplification [143]. The timescales over which a modulation of the refractive index takes place are dependant on the photorefractive mechanism. For example, in photorefractive crystals, the time response is based on the time it takes charge carriers to be promoted to the conduction band, and move to a trapping site in a dark region - ~ 0.1 μs in lithium niobate crystals [144]. The charge carrier mobility is also responsible for the time response of photorefractive polymers, although in this case it is generally dominated by drift due to

an applied electric field. The charge carrier mobility in a common photorefractive polymer diethylaminobenzaldehyde-methylphenyl-hydrazone e.g. is 10^{-7}-10^{-6} $cm^2V^{-1}s^{-1}$ [145]. Measurements of these time responses are described in [144, 146].

The time response of a photoconductive-polymer based LCLV is dependent on the rotational viscosity, cell thickness and elastic constant of the LC, as well as the charge carrier mobility in the photoconductive polymer. The charge carrier mobility is highly dependent on temperature [80] and the space-charge field formation time can be comparable to the LC response time. Therefore the time response of the entire device has to be considered. The time evolution of the diffraction efficiency can be measured in order to obtain a figure-of-merit for the time response of these systems.

6.2.3 Photorefractive response

There are several figures-of-merit that can be used to characterize the strength of the photorefractive response in photorefractive systems. Two-beam coupling has already been described in great detail in chapter 4, and is a typical technique for characterizing the photorefractive effect of a light valve due to the ease with which control parameters such as the grating spacing can be varied, and the fact that beam coupling behaviour can only be achieved due to the photorefractive nature of a medium [147, 148]. Furthermore, optical beam amplification is a potential commercial application of these systems, in particular for optical circuitry and coherent image amplification [51, 52]. Therefore, TBC gain - generally defined as the ratio of the intensities of the two fundamental diffracted orders - can be used to characterize the photorefractive effect.

The other common technique is to measure the diffraction efficiency of an induced grating, which is described in section 2.7. The figure-of-merit in this case would be $\eta = I_1/I_0$, where $I_{0,1}$ are the intensities of the fundamental and first order diffracted beams respectively. The diffraction efficiency is also measured for non-photorefractive gratings, for example in accousto optic modulators [149].

The ratio of a change in the refractive index and the intensity necessary to induce that change; a parameter known as the Kerr non-linear coefficient, $n_2 = \Delta n/I$ [138], is another potential figure-of-merit. n_2 can be calculated from measurements of the phase

Material	Dark conductivity [Ω^{-1} cm^{-1}]	Light conductivity [Ω^{-1} cm^{-1}]
PVK:C_{60}	10^{-16} [88]	10^{-15} [88]
BSO	10^{-15} [49]	10^{-11} [49]
Amorphous silicon	10^{-8} [134], 10^{-9} [151]	10^{-4} [134], 10^{-5} [151]

Table 6.1: Values for the light and dark conductivity of PVK:C_{60}, BSO and amorphous silicon. The light conductivity was measured at saturation in each case.

shift in a CPI experiment under varying illumination [135]. n_2 must be recorded as a function of voltage for voltage-dependent systems, particularly LCLVs and photorefractive polymers. It can also be measured as part of a TBC experiment as described by Ouskova *et al* [150].

6.3 New materials for LCLVs

LCLVs that consist of a photoconductor in contact with an LC layer, such as those reported on in this thesis, originally used inorganic crystalline wafers as the photoconductor, most notably bismuth silicon oxide [49], amorphous silicon [134] and gallium arsenide [135]. These photoconductors typically exhibit a higher contrast between the dark and light state conductivity, which in turn increases the MTF (defined in appendix B) and hence the non-linear response of the device. PVK on the other hand has a much lower contrast between the two conductivities, and hence is a less efficient material for producing LCLVs according to the MTF. The dark and light conductivities for PVK:C_{60}, amorphous silicon and bismuth silicon oxide (BSO) from the literature are summarized in table 6.1.

Polymers such as PVK do offer many significant advantages in both cost and processing techniques. Semiconducting crystals require lengthy and expensive growth techniques, whereas extremely flat, thin and clean layers of polymer can be produced by spin coating directly on to an ITO electrode. In this way, large quantities of polymer films can be fabricated in a relatively short space of time, and changes in layer thickness or polymer make-up (e.g. the concentration of dopants) can be established without any significant difficulty.

The aim of this chapter is to explain alternative polymer materials and LCLV schemes that can achieve higher diffraction efficiencies than the PVK:C_{60} light valves that have been investigated thus far. Theoretical overviews will be given, as well as some results comparing the non-linear response to that of the PVK:C_{60} benchmark cells. Firstly however, the motivation for investigating alternatives to PVK:C_{60} as a photoconductor will be discussed.

6.4 Drawbacks to the use of PVK in LCLVs

While PVK has for some time been used in printers [152], it was not until 1997 that it was first used as a photoconducting layer for an LCLV [78]. In place of C_{60}, trinitrofluorenone (TNF) was used as a photosensitizer. The role TNF plays is to create a charge transfer complex with the PVK, which in turn modifies the energy required to excite the free charge carriers that contribute to the conductivity [153, 154]. This is a useful way of controlling the wavelength with which the polymer can be addressed, as well as altering the charge carrier mobility and the charge injection barrier with common electrode material (see section 6.5.1).

Attempts to create a more efficient charge transfer complex have concentrated on mixing PVK, a strong electron donor with strong electron acceptors [155]. C_{60}, is a particularly strong electron acceptor: up to six electrons can be accepted per molecule [156]. Therefore, composite films of PVK with C_{60} are extremely efficient photoconductors [157].

Despite this, there are three specific drawbacks with using PVK:C_{60} films in an LCLV. Firstly is the aforementioned low contrast in the dark and light conductivities when compared to inorganic photoconductors, as shown in table 6.1. Secondly, due to the deep HOMO (highest occupied molecular orbit) level in PVK:C_{60}, there is typically an injection barrier between the ITO electrode and the photoconductor [76]. Finally, PVK:C_{60} is a non-ohmic conductor, as was shown in chapter 4, which, despite the fact it does not directly affect the non-linear optical response, does makes it difficult to predict the behaviour under given field conditions.

The low contrast between dark and light conductivities and the non-ohmic behaviour of PVK:C_{60} films are intrinsic material properties, and as such can only be addressed by examining alternative materials. It is also worth investigating the nature of the injection barrier in a little more detail, as there are alternative materials to ITO that can be used as transparent electrodes. The next three sections describe materials which can be used in place of a single PVK:C_{60} layer in LCLVs, the potential improvements, and how the systems were incorporated into an LCLV system as part of this investigation.

6.5 The use of PEDOT as a transparent conductor

Injection barriers between electrodes and semiconductors limit the current that can flow across the boundary, thereby limiting the photocurrent in the case of PVK:C_{60}-based LCLVs. Poly(3,4-ethylenedioxythiophene) or PEDOT is a conducting polymer with a lower work function than ITO [158, 159], which will drastically reduce this barrier, thereby allowing more efficient charge transfer on to the PVK:C_{60} layer. This section begins with a description of these injection barriers, followed by a discussion on PEDOT, and how it can be used to enhance the photorefractive modulation in LCLVs.

6.5.1 ITO/PVK injection barriers

There is not currently a widely accepted theory that accounts for carrier injection barriers between metals and organic compounds, which may come as something of a surprise, given the fact that widely used technologies such as OLEDs [160] and organic photovoltaics [161] include photoconductive materials - commonly containing PVK - in contact with metal electrodes. Possible candidates for the physical mechanism that accounts for charge injection from metal to organic semiconductor include tunnelling of charge carriers a [162], space-charge limited current [163] or thermionic emission [164].

ITO has a work function - the energy required to remove a charge carrier from the conduction band to an infinite distance away from the ITO - of around 4.8 eV [165], although there may be some discrepancy depending on how the ITO films are fabricated and treated prior to being used in an LC cell. In order for a charge to move into the

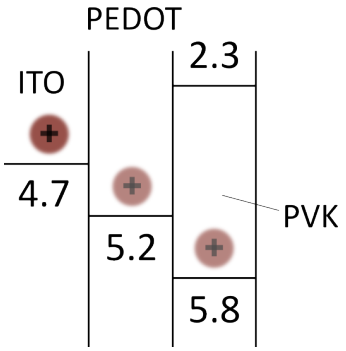

Figure 6.2: Work functions of ITO and PEDOT, and electron affinity and ionization energy for PVK. Values are taken from [159, 166], and have units of eV.

conduction band or HOMO of the contact semiconductor, this energy must be similar to the ionization energy or electron affinity of the semiconductor, depending on whether hole or electron transport are being considered, respectively. The larger the discrepancy between the two values, the higher the potential barrier that needs to be overcome in order to achieve charge injection.

An energy level diagram showing the work functions of ITO and PEDOT, as well as the electron affinity and ionization energy of PVK can be seen in figure 6.2.

6.5.2 PVK-PEDOT layers

PEDOT is a transparent conductive polymer that has found wide use in the field of photovoltaics [167] and LCDs [168]. When introduced by Jonas and Schrader in 1991 [169], it was the only conducting polymer that was stable thanks to low molecular strain. It has a high conductivity, similar to that of ITO, is optically transparent in the visible region of the EM spectrum, and can be processed in the same way as any other polymer [170].

PEDOT can be used as a charge injection layer between ITO and PVK, in order to significantly reduce the injection barrier. Experimental studies, e.g. by Khalifa *et al.* of such studies have shown that the barrier is reduced significantly when compared to injection from bare ITO onto PVK [171]. However, Khalifa *et al.* showed that it is difficult to model the barriers, as the relevant current-injection models describing the current in these structures (the Fowler-Nordheim model for tunnelling [164], and

thermionic emission [163]) cannot predict the I-V characteristics. Despite this, PEDOT electrodes have been shown to offer tremendous advantages in terms of efficient charge transfer when compared to bare ITO.

6.5.3 PVK-PEDOT for use in LCLVs

PEDOT was investigated as an alternative charge injection layer to ITO in LCLVs, in order to determine if the lower injection barrier would lead to a higher photoconductivity, and hence a larger photo-mediated modulation of the refractive index. The PEDOT was coated on ITO substrates, and then a layer of PVK:C_{60} was coated on top to create a ladder structure, which was then incorporated into a cell. The cells were then tested in a diffraction efficiency experiment, and compared directly with a cell that omitted the PEDOT layer. The fabrication and characterization of these cells is described in section 6.8.1.

6.6 Incorporating photorefractive polymers into LCLVs

Photorefractive crystalline windows can be used to fabricate LCLVs that do not require an applied voltage, and instead rely on the formation of space charge fields due to inhomogeneous illumination. Photorefractive polymers offer significant advantages over inorganic crystals in terms of cost and ease of development. Therefore, photorefractive polymers have been investigated as a potential replacement for PVK:C_{60} films in LCLVs. This section will first explain how photorefractive crystals have been used in other studies to create LCLVs. Then, photorefractive polymers will be discussed, and contrasted with crystalline materials. Finally, the incorporation of photorefractive polymers into LCLVs will be introduced.

6.6.1 The use of photorefractive crystals in LCLVs

LCLVs consisting of an LC layer sandwiched between two photorefractive crystalline windows are described by Cook *et al.*, and rely on an induced space-charge field to switch

the LC [172]. The mechanism of the formation of space-charge layers in photorefractive crystals is as follows.

Free charges are promoted to the conduction band of the crystal via absorption of light, in the same way as for photoconductive polymers. These charges are transported through the material via drift, diffusion, and/or a photovoltaic effect due to the incident light field [173], and at a later time will encounter a trapping centre [174]. If this trapping centre is located in an illuminated area of the material, then it will be re-promoted to the conduction band some time later, whereas if it is trapped in a dark area, it will remain trapped. Therefore, the mobility of the charge carriers is extremely important; some materials require huge voltages to induce a sufficiently high drift mobility in order to be trapped in a dark region [175]. The charge carrier mobility in the majority of photorefractive crystals is sufficiently high that diffusion is sufficient for space-charge fields to form, and therefore it is not necessary to apply an electric field [176].

Over time, an inhomogeneous distribution of charge carriers will form in the material, and the resulting space-charge field can cause a re-orientation of a neighbouring LC layer. In this way photorefractivity is achieved [172].

6.6.2 The use of photorefractive polymers as an alternative to photorefractive crystals in LCLVs

Photorefractive polymers are perhaps of more technological interest than their crystalline counterparts due to the extremely low cost, and the ease of film fabrication. Also, it has been shown more recently that one can obtain a stronger photorefractive response in polymers than in crystals [90]. They tend to be four-component mixtures, including: a photoconductor, a chromophore that exhibits electro-optic nonlinearities, a plasticizer, and a photosensitizer, the use of which is identical to photosensitizers used in PVK:C_{60} Ducharme *et al.* were the first to demonstrate photorefractivity in a polymer [177], and many others have since been studied, including PVK based composites doped with chromophores [178, 179] .

One drawback of photorefractive polymers is the low diffusion mobility of the free charge carriers [175], which makes it difficult for charge distributions to form. A solution is to use transverse electric fields to drive charge carrier drift by drastically increasing the trapping distance i.e. the average distance travelled by free charge carriers until they encounter and are confined by a trapping site [180]. These transverse electric fields typically take values of the order of 10 Vμm^{-1} [181, 178, 182].

LCLVs can be fabricated using photorefractive polymer films in place of the photorefractive crystalline windows used in the devices described above. Although it is extremely unlikely that a significant space-charge field could be promoted without the application of a high-magnitude transverse field, the photoconductive behaviour of the polymer should cause the cell to be photorefractive under application of a field, and the electro-optic component of the polymer could act to enhance the effect. The fabrication and characterization of such devices is described in section 6.8.2.

6.7 Photoaligning surfaces in LCLVs

The alignment of LCs at the interface with a polymer layer is generally achieved by rubbing the polymer with a rotating cloth prior to constructing the cell [30]. This process is effective, but has drawbacks when fabricating highly-homogenised alignment layers for use in the display industry, where small variations in surface charges, and the introduction of fine dust particles can adversely affect the optical quality of devices. Furthermore, it is impossible to use rubbing when investigating closed surfaces filled with LCs, such as LC assisted optical fibres [183].

Photoaligning polymers, developed by Ichimura *et al.* in 1988 [184], are an alternative option, where the alignment can be fixed by illuminating a sample with the appropriate wavelength and polarization. Generally, the chemical makeup of the polymers are based on azobenzene dyes: molecular structures that undergo an isomer change when excited with incident light. The simple azobenzene structure is shown in figure 6.3, and consists of two phenyls linked by a double-bonded nitrogen group.

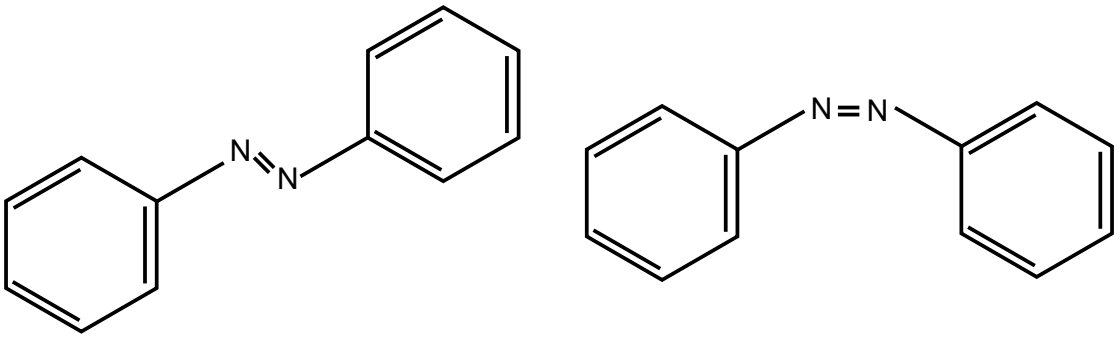

Figure 6.3: Two isomers of azobenzene, the trans and cis states, are shown on the left and right respectively. Absorption of light in the trans state will cause a transition to the less stable cis state, which will decay back to the trans state some time later due to thermal excitation.

Two possible isomeric states are shown in figure 6.3, known as the trans and cis state. The trans state is more energetically stable, and hence the group will always eventually decay into this ground state from the cis due to thermal excitation. The cis state is obtainable via absorption of light or heat energy, although it is only photonic excitation that is of interest here. Polymers containing azobenzene molecules can be engineered such that LC mesogens lie parallel with the polymer chain, in a very similar way to other aligning polymers such as PI.

The process by which light can affect the alignment of LCs is as follows. An initially unaligned film of azobenzene polymer is illuminated with linearly polarised light. Molecules with chains that lie perpendicular to the polarization vector cannot absorb any of the light, while all other alignments can. Molecules that absorb light will transition to the cis state, and some time later relax to a trans state with a random orientation. If this orientation is not perpendicular to the polarization then the process can repeat, whereas if the random relaxation has forced a perpendicular orientation, no more light can be absorbed and the alignment is fixed. In this way, a uniform alignment is formed over time which lies perpendicular to the polarization of the writing light [185].

There are important factors to consider when forming these photoaligning surfaces, chiefly the necessary writing wavelength and intensity of the incident light, the time it takes for the alignment layer to form and the reversibility of the reaction.

It was decided to use a hybrid cell consisting of a photoaligning polymer on one surface, and PVK:C_{60} on the other, in order to try to overcome one of the major drawbacks

of PVK:C_{60} and indeed most polymer photoconductor-based LCLVs, namely that the electric field and hence the phase grating does not extend very far into the cell [94]. If there is a layer on the other surface which is inducing a complementary phase grating, then this modulation depth could, theoretically, be increased. Not only would this lead to more effective light valves, but it could also lead to light valves where the gain scales with thickness, which is not the case with the current systems.

6.8 Fabrication and characterization of new LCLV systems

This section outlines the fabrication of LCLVs incorporating the materials described above. The fabrication process of the cells is explained, along with the resultant characterization of the strength of the photorefractive response.

6.8.1 LCLVs with lowered injection barriers

This section describes the fabrication of PEDOT layers for use as transparent electrodes in PVK:C_{60} based LCLVs, and the resultant characterization of the photorefractive response.

6.8.1.1 Fabrication of LCLVs with PEDOT/PVK:C_{60} structures

The PEDOT used for the construction of these cells was spin-coated from a solution obtained from Ossila (Ossila M121) . ITO slides were first cleaned with water and lab tissue, dried using compressed air, and then the process repeated with acetone. After a visual inspection to ensure no dust was on the ITO surface, the slide was fixed into a MODEL spin coating machine. 400 μl of PEDOT solution was dropped onto the surface, which covered the entire area. The spin-coating recipe was as follows: an initial spin at 1500 rpm for 5 s was followed by a 2 s ramp to a secondary spin at 4000 rpm for 30 s. The films were observed after spinning to check for visual defects, which could be evidence for a problem in the spin-coating method. The visual evidence for possible spin-coating issues are shown in figure 6.4, and if any of these patterns was observed,

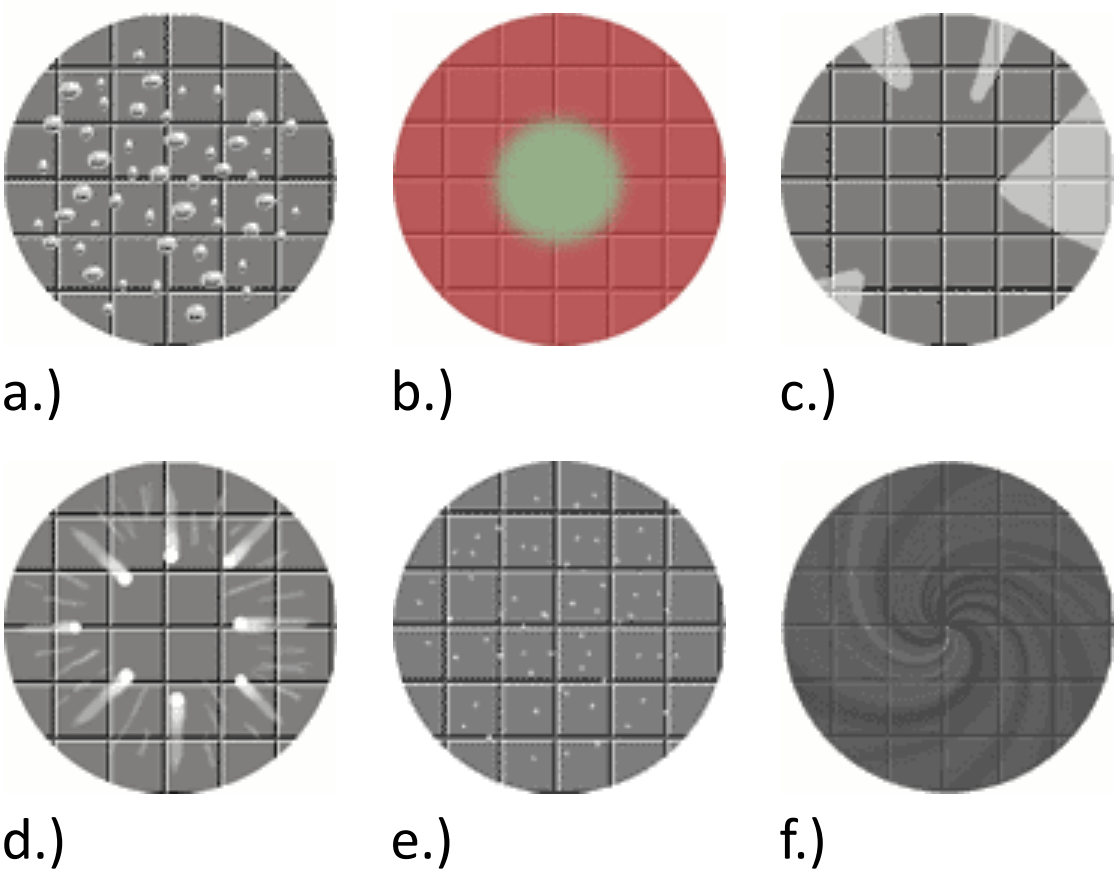

Figure 6.4: Observations of imperfect spin-coated films. a.) suggests air bubbles were left in the solution, b.) is due to a chuck mark, c.) is for an insufficient solution volume, d.) suggests that the spin speed is too high, or that the fluid was left on the sample too long before spin coating starts, e.) shows particles in the fluid or on the surface prior to spinning, and f.) either that the spin speed is too high, or that the spin time is too short. Taken from [187].

then the slide was cleaned with acetone and lab tissue, and re-coated. Once a uniform film was observed, the slides were placed on a hot plate held at 80°C for 60 mins in order to evaporate the solvent and anneal the polymer [186].

PVK:C_{60} solution dissolved in dichlorobenzene was spun on top of the resultant PEDOT layer after allowing the slide to come to room temperature. It was important not to leave the PVK solution in contact with the PEDOT layer for any significant length of time before starting the spin coater, as this could potentially dissolve some of the PEDOT layer, introducing non-uniformity in the polymer layer thickness; the time between applying the PVK solution and starting the spin-coating process was kept below 10 s. Dropping the PVK solution onto the PEDOT layer while spinning was also attempted, but subsequent tests showed no significant difference between the techniques. The spin

coating recipe was identical to that for PEDOT, and the slides were left to anneal at 100°C for 2 hours.

PI films were fabricated in the same way as described in section 3.6, and fixed together with the PEDOT/PVK:C_{60} slides to create the cells. These were then filled with E7 using capillary forces. Two cells were fabricated and observed between crossed polarizers to determine that uniform alignment had been achieved. For one of the cells, significant areas showed poor alignment, where almost no polarization rotation could be seen - this cell was discarded.

6.8.1.2 Characterization of LCLVs with PEDOT/PVK:C_{60} structures

The resultant diffraction efficiency as a function of applied DC voltage was measured using the experimental scheme shown in figure 6.5.

A 532 nm DPSS laser source was used to write the grating, as this wavelength can induce photoconductivity in PVK:C_{60} [72], and the intensity has been found to be sufficient to write a diffraction grating in the device. The power of the radiation output from the laser was 60 mW. A variable neutral density (ND) filter was used to reduce the power of one of the two beams output from the beamsplitter, in order to ensure that the power of the two beams was equal: 52.1 mW. The beam radius was measured using a scanning razor blade technique, which gave a value of 1.1 mm, assuming a Gaussian beam profile [188]. The bisector of the two beams was parallel to the normal to the cell, and the grating spacing calculated from the angle of interception using equation 2.26:

$$\Lambda = \frac{\lambda}{2\cos\beta}, \tag{6.2}$$

where β is the angle of the bisector.

The grating was probed using a 632 nm HeNe laser source, incident at an angle to the cell. The intensity of the diffracted order is dependent on the angle of the probe beam, as shown in section 2.7. This meant it was important to keep the experiment consistent in order to compare the diffraction efficiency different systems. The power of this beam was 4.5 mW.

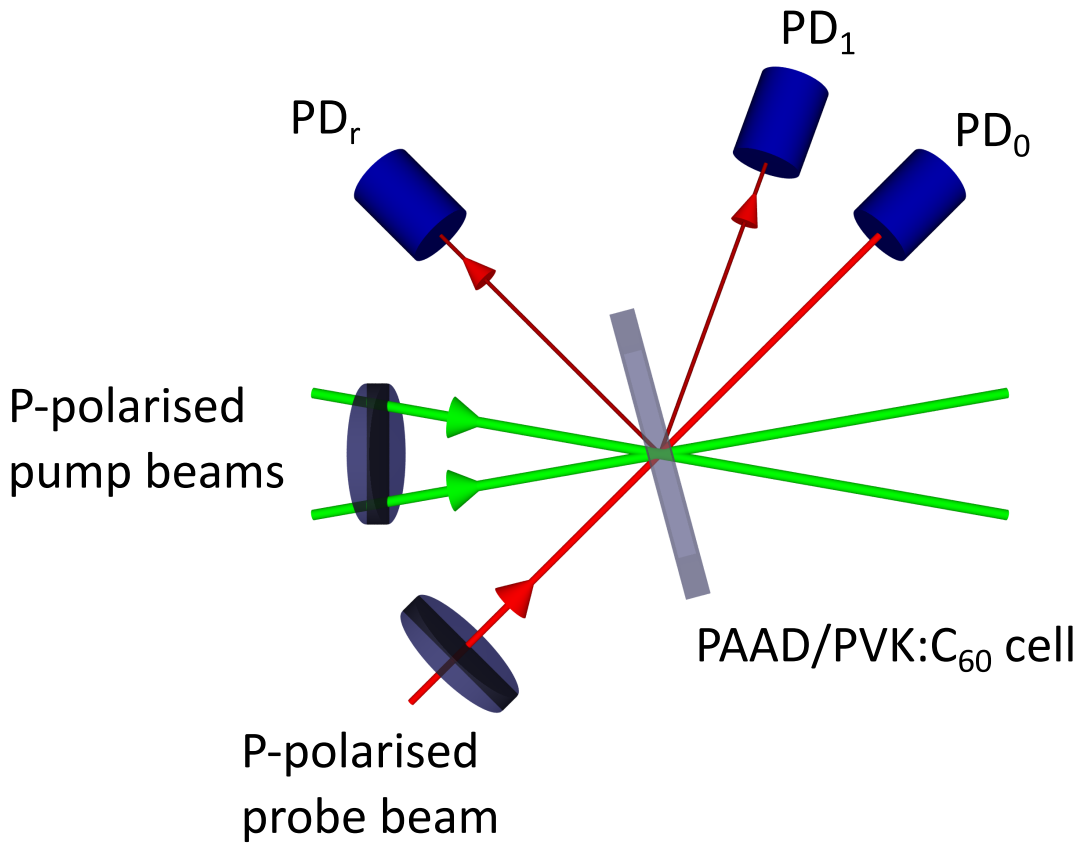

Figure 6.5: Experimental setup for measuring the diffraction efficiency of LCLVs. PD refers to the different photodiodes shown in the diagram. The grating spacing was set to 30 μm, and the DC voltage was swept in 0.2 V steps from 0-20 V.

The diffraction efficiency was measured as a function of applied DC voltage, output from a TTI PL303 power supply. The intensity of each beam shown in figure 6.5 was measured using a ThorLabs PDA25K photodiode, output to an NI6211 data acquisition card. The reflected beam was monitored to correct for any fluctuations in probe laser intensity. The voltage step was 0.2 V, and the cell was held at each voltage for 5 s, at which point the intensity was sampled at 25 kSs^{-1} for 2 s. The intensity of the incident beam was measured before the experiment started, and fluctuations were monitored using PD$_r$. The first diffracted order from the probe beam was measured by PD$_1$, and was used to calculate the diffraction efficiency. The results are shown in figure 6.6, and discussed in section 6.9.

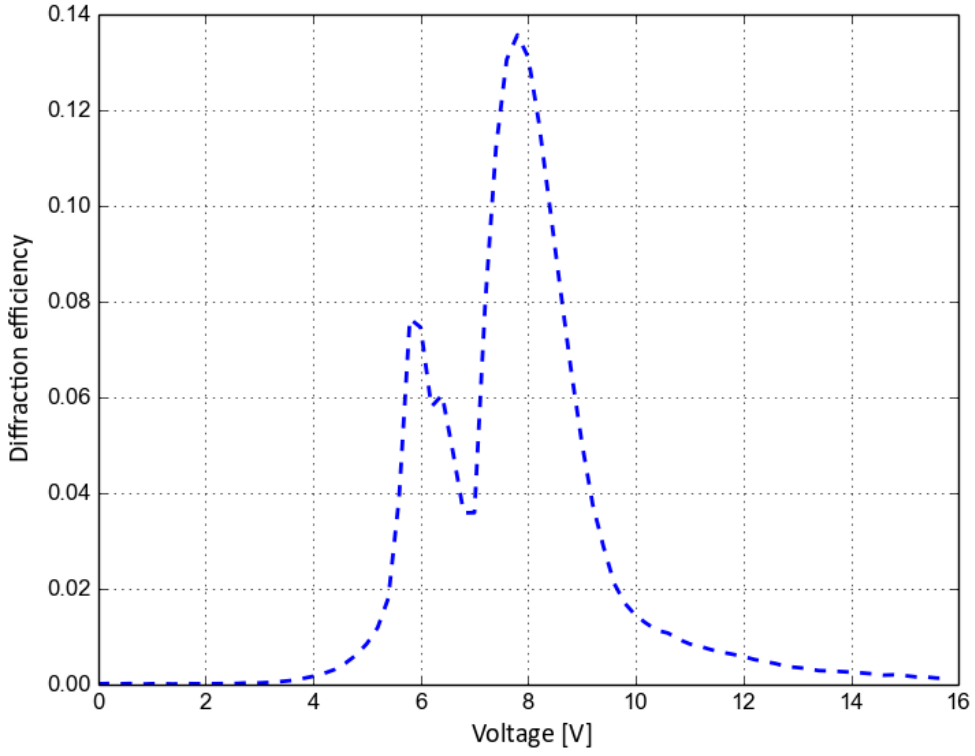

Figure 6.6: Resultant diffraction efficiency as a function of applied voltage for PI/PEDOT-PVK:C_{60} cell.

6.8.2 Photorefractive polymers used in LCLVs

The fabrication of LCLVs using a photorefractive polymer is described here, along with the characterization of the strength of the photorefractive response. These cells were made and tested at a different time to others described in this chapter, and there will have been some differences in the characterization which will affect the measured diffraction efficiency. These differences will be discussed in section 6.10.

6.8.2.1 Fabrication of LCLVs with photorefractive polymers

The photorefractive polymer used in this investigation, JTDA16, is an acetylane-based photorefractive polymer. The polymer was developed by Thomas *et al.* [181] as an alternative to PVK based composites, and was supplied by Pierre Blanche and Jayan Thomas from the University of Arizona. The photoconductive component of the polymer is based on triarylamine; such polymers have been shown to work very well as

photoconductors for use in organic light emitting diodes, where the hole mobility has been shown to be higher than PVK [189]. Thomas *et al.* also note that PVK-based polymers tend to have low lifetimes, which could potentially be improved by finding a suitable alternative.

JTDA16 has a polyacrylate backbone, with hole-conducting, photoconductive tetraphenyl-diaminobiphenyl (TPD) pendant groups with alkoxy linkers; the polymer is given the initialism PATPB. Two different nonlinear chromophores are present: 4-homopiperidino benzylidine-malonitrile (7-DCST), and 3-(N,N-di-*n*-butyl-aniline-4-yl)-1-dicyanomethylidene-2-cyclohexene (DBDC). 7-DCST is a fairly common chromophore [179], and DBDC was found by Thomas *et al.* to be more compatible with the main polymer structure, and both chromophores follow the same design strategy outlined by Marder *et al.* for developing effective chromophores for use in these organic systems [190]. The chemical structures of PATPD and those of the two chromophores are shown in figure 6.7. *N*-ethyl-carbazole (ECZ) was used as a plasticizer to ensure that the glass transition temperature is close to room temperature, and C_{60} was used as the photosensitizer to bring the operating wavelength band into the visible spectrum.

The polymer was supplied in bead form, and needed to be dissolved in a solvent in order to be spin-coated onto an ITO substrate. Acetone and isopropanol solvents were tried initially as they are widely available, but the polymer was insoluble in both. Dichlorobenzene, the solvent used to dissolve PVK, was the next candidate, and the solubility was found to be much higher. The result was a vivid yellow solution, suggesting that the absorption of the polymer is quite strong in the blue part of the EM spectrum. The next step was to investigate different concentrations of the polymer for use in the spin-coating process.

The initial concentration of the solution was 10 g/l. The spin-coating recipe used was identical to that used for PVK:C_{60}. The cleaned ITO substrate was placed on the spin-coater chuck, and covered over the entire area with the solution. The sample was initially spun at 1500 rpm for 8 s, followed by a 30 s run at 4000 rpm. The films were then observed visually in case there had been a problem with the recipe, the cleanliness of the ITO or the amount of material deposited before spinning as described above.

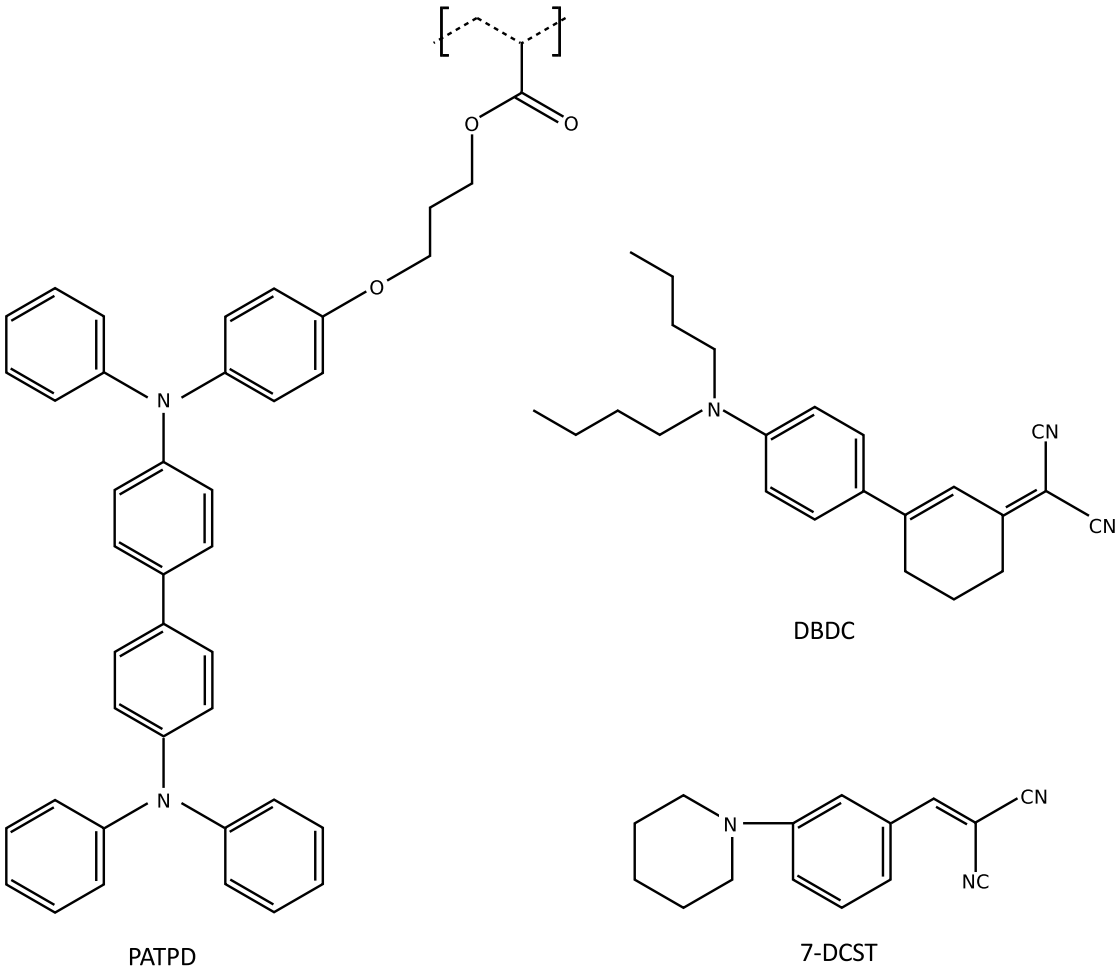

Figure 6.7: The chemical structures of the photoconductor PATPD, and the two chromophores 7-DCST and DBDC present in JTDA16

The resultant films were determined to have no defects due to the spinning process, and were subsequently rubbed and fixed together with UV-curable adhesive mixed with spacer beads to create 12 μm LC cells. The LCs were found to align parallel to the rubbing direction, as is the case with most polymers.

The set of cells fabricated in this way all consisted of one substrate coated with JTDA16, and one with PI, with a 12 $\pm 0.3\mu$m thickness, as well as one PI/PVK:C_{60} cell for benchmarking purposes. The JTDA16 solution was made progressively more concentrated in order to test the effect this would have on the photorefractive response of the devices (if any), as the thickness would increase as the viscosity increases. The concentrations were 2, 4 and 6 times the initial concentration of 10g/l.

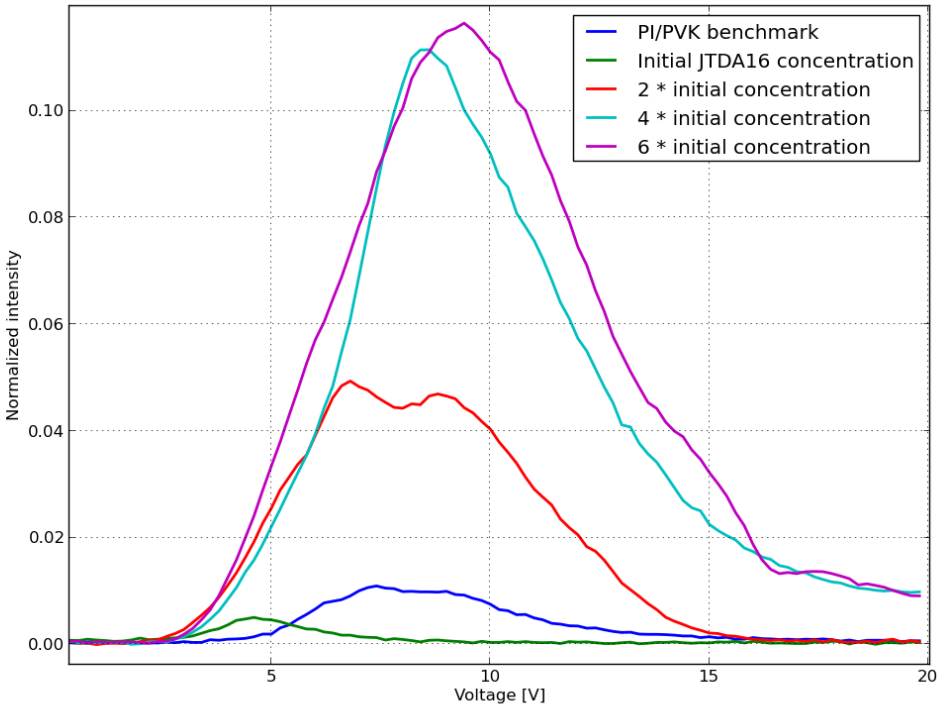

Figure 6.8: Resultant diffraction efficiency as a function of applied voltage for PI/JTDA16 cells, as well as a benchmark PI/PVK:C_{60} cell.

6.8.2.2 Characterization of LCLVs with photorefractive polymers

The diffraction efficiency of the cells was measured using the same experimental setup described in section 6.8.1.2. The cells were fabricated and characterized at different times to the PEDOT and PAAD cells, and the experimental set-up was slightly different, most significantly, the grating spacing in this case was 12 μm. The resultant data are shown in figure 6.8.

6.8.3 Characterization of LCLVs with PAAD polymers

PAAD is an azobenzene polymer with a large absorption band that extends into the visible, and the photoalignment of which is reversible [191]. This could make it an ideal photoactive layer for LCLVs; with careful geometry considerations, it should be possible to change the refractive index of the cell depending on the incident light intensity.

Cells with one PVK:C_{60} aligning layer, and one PAAD aligning layer were fabricated and donated by Beam Engineering, a US company that specializes in photoaligning materials. One cell contained E7, while the other contained TL205. Preliminary measurements of the diffraction efficiency showed that the photorefractive response in TL205 was significantly lower than in E7, a result which supports the theory of TBC outlined in chapter 4. It was important to set up the geometry of the experiment extremely carefully to account for the PAAD response.

PAAD aligns LCs perpendicular to the polarization angle of incident light, assuming that the light is sufficiently intense and has a wavelength that the PAAD polymer will absorb. In addition, it is important in experiments involving PAAD based cells to have the light incident on the PAAD layer, as any polarization modification caused by the light passing through the LC layer will lead to an undesired reorientation.

The PAAD was aligned prior to this experiment by exposing it for 10 minutes using a Fianium supercontinuum laser source, emitting 10 mW of white light polarized perpendicular to the alignment at the PVK:C_{60} surface due to rubbing. The resulting alignment should have been uniformly planar, but as figure 6.9 shows, there are two areas in the centre of the cell that appeared to be in a twisted geometry, even after exposure. This is presumably down to some long-term degradation in the PAAD polymer structure, but it can be accounted for by avoiding these areas when performing diffraction efficiency experiments.

The diffraction efficiency was measured as a function of applied voltage in the same experiment described in section 6.8.1.2. The initial director of the cell was positioned to be parallel to the horizontal polarization of the writing laser source, which meant that the illuminated PAAD would theoretically reorientate the LC - fortunately, this geometry has been found to give a higher diffraction efficiency for PI-PVK:C_{60} cells as well [94]. The experiment was repeated at 13 and 30 minutes, as the process by which re-alignment takes place at the PAAD polymer interface can take some time; gratings have been reported that take 10 minutes or more to form [185]. The results for all three experiments are shown in figure 6.10.

Figure 6.9: Photograph of the PAAD/PVK:C_{60} cell after exposure to linearly polarized blue light. The lighter areas towards the centre of the cell indicate that the LC is in a twisted geometry in those areas, and exposure has not caused the LC to completely re-align at the PAAD/LC interface. Therefore, those areas are avoided when performing the diffraction efficiency experiment.

Figure 6.11 shows diffraction efficiency results for a benchmark PI/PVK:C_{60} cell that was tested in the same set-up as the PEDOT and PAAD cells.

6.9 Discussion of the diffraction efficiency characterization for new LCLV devices

This section will highlight relevant behaviour seen in the characterization of the photorefractive effect in new LCLVs. Table 6.2 shows the peak diffraction efficiency, the alignment layer material at each surface, and cell thickness for each cell.

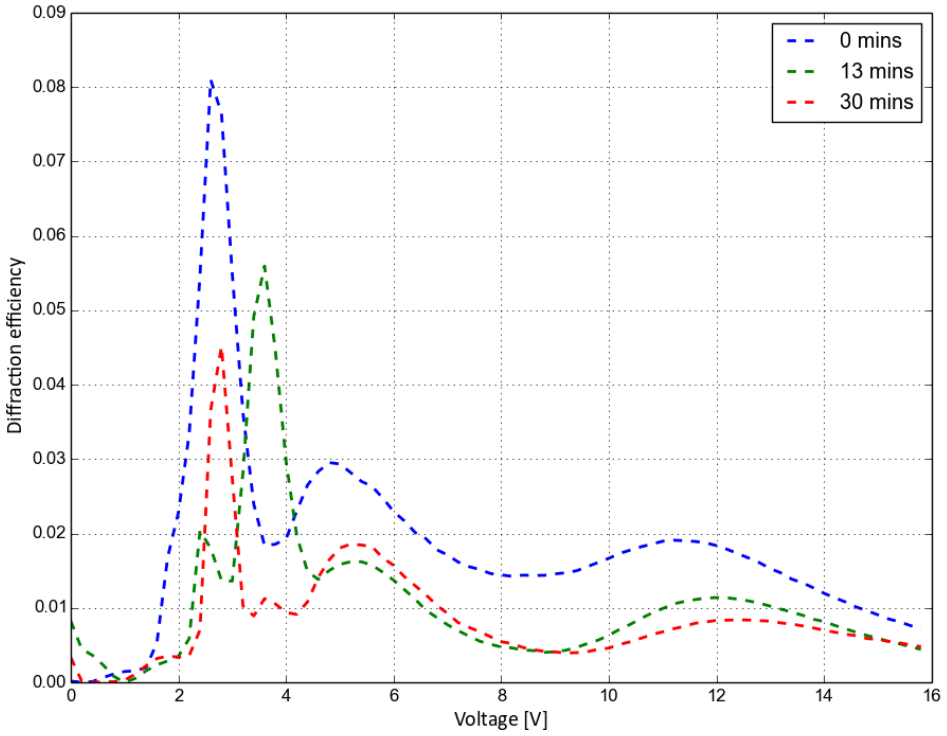

Figure 6.10: A graph showing the diffraction efficiency of a single 10 μm E7 PAAD/PVK:C_{60} cell at different times after the initial exposure with the grating writing beams.

Layer A	Layer B	Thickness [μm]	Peak diffraction efficiency
PEDOT/PVK:C_{60}	PI	12.4	13.8%
PAAD (0 mins)	PVK:C_{60}	10.0	8.1%
PAAD (13 mins)	PVK:C_{60}	10.0	5.7%
PAAD (30 mins)	PVK:C_{60}	10.0	4.5%
JTDA16 (10 g/l)	PI	12.3	0.6%
JTDA16 (20 g/l)	PI	12.1	4.9%
JTDA16 (40 g/l)	PI	12.7	11.1%
JTDA16 (60 g/l)	PI	12.0	11.7%
PVK:C_{60}	PI	11.3	1.0%
PVK:C_{60}	PI	12.9	4.5%

Table 6.2: Table showing the peak diffraction efficiency for each of the LCLVs discussed in this chapter. The final two lines are for benchmark cells tested in different setups. The first cell was tested in the same setup as JTDA16 based LCLVs, and the second was tested in the same setup as PAAD and PEDOT based LCLVs.

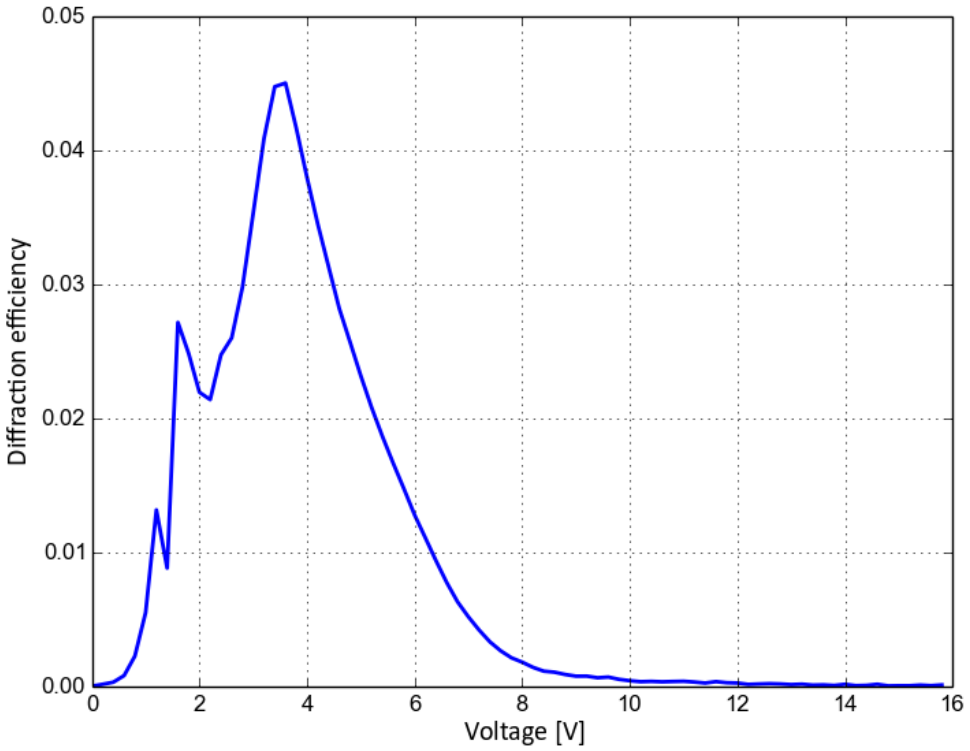

Figure 6.11: The diffraction efficiency as a function of applied voltage for a benchmark PI/PVK:C_{60} cell, for comparison with PAAD and PEDOT based devices.

The voltage at which the highest diffraction efficiency was achieved differed for each set of cells: the peak diffraction efficiency for the PEDOT cells occurred at $\sim$ 8 V; for PAAD, 2-4 V and for JTDA16, $\sim$ 9 V. The peak diffraction efficiency for the JTDA16 cells increased significantly as the concentration of the initial solution increased, until 40 g/l where higher concentrations did not change the peak value significantly. The diffraction efficiency in PAAD cells fell for subsequent measurements at 13 and 30 minutes. The highest diffraction efficiency achieved was 13.8% in the PEDOT/PVK:C_{60} cell. These observations shall be discussed in the following conclusions section, 6.10.

6.10 Conclusions of diffraction efficiency experimental results from new LCLVs

This section discusses the scientific conclusions that can be drawn from the results presented in this chapter. The systems will be discussed separately, and future work arising from the investigation will be described in chapter 7.

6.10.1 Conclusions from PEDOT results.

The PEDOT results should verify whether or not the injection barrier that is undoubtedly present between ITO and PVK:C_{60} [76] has a significant effect on the photorefractive response of an LCLV. Theoretically, the easier it is to inject charge onto the PVK layer to replace photogenerated charges, the higher the photoconductivity can be. A comparison between figures 6.6 and 6.11 shows conclusively that the PEDOT layer does seem to increase the diffraction efficiency, by a factor of 3.

One interesting feature of the PEDOT cell is the very obvious two-peak behaviour, where the diffraction efficiency falls at 7 V, before rising to it's maximum value of 13.9% at 7.8 V. This could be due to the non-ohmic behaviour of PVK, as discussed in section 4.7.4.2; it should be noted that this is an intrinsic material property of PVK, and as such is distinct from the contact between PVK and the electrode material. The behaviour of two beam coupling in PI/PVK:C_{60} cells is evidence for the fact that the conductivity of PVK is voltage dependant, and the two peaks may indicate a switch between the two conductivity states in the PVK:C_{60} layer.

Our collaborators (Thomas Regrettier and Thomas Heiser from the Université de Strasbourg [192]) have confirmed that it is very difficult to measure whether or not one has an ohmic contact between an electrode and PVK, thanks to the very deep HOMO level of PVK. Nevertheless, it should be possible to select suitable electrode structures by taking inspiration from literature studies investigating organic photodiodes and phototransistors, where PVK still plays a prominent role. Although one may never be completely sure about the nature of the contact between the electrode and the PVK layer,

various materials can be used in LCLV devices to find the optimal structure for use in photorefractive devices.

6.10.2 Conclusions from JTDA16 results.

Firstly, it should be noted that there is no observable photorefractive effect at 0 V in the JTDA16 based system, meaning any space-charge field set up by diffusion of photogenerated charges is too small to affect the LC director. This is unsurprising - as noted, a high transverse field is generally required to set up such a grating in photorefractive polymers - but it is important to realise that these systems are not equivalent to the photorefractive crystalline window cells used by Cook *et al.* [172].

The diffraction efficiency of the devices increases with the concentration of the solution used to process the films, until reaching a maximum value at a concentration of 60 g/l of 11.8%. Increasing the concentration did not change the diffraction efficiency at this point, implying that 60 g/l gives a film of the optimal thickness for a photorefractive cell. Furthermore, this diffraction efficiency is far higher than that of the reference PI-PVK:C_{60} cell, suggesting that JTDA16 offers huge advantages over PVK as a photoconductor in these hybrid cells.

The electro-optic chromophores 7-DCST and DBDC are unlikely to have had a non-negligible effect on the refractive index of the system due to the extremely low diffusion mobilities of charges in JTDA16 [181]. However, it would be necessary to check a cell constructed using PATPD without the chromophores in order to verify this. It is possible that the field conditions in this system contribute in some unknown way to the formation of a space-charge distribution, but this would need to be confirmed experimentally before modelling the effect.

6.10.3 Conclusions from PAAD results

The diffraction efficiency as a function of voltage in PAAD cells is distinct from that observed in PVK based systems, and in JTDA16 cells. It does not decay to 0 at high voltages, but rather undergoes secondary oscillations at $\sim$ 5 V and $\sim$ 11 V for the

0 minute scan shown in figure 6.10. This behaviour is reminiscent of the Bessel functions shown in figure 6.12 which was first introduced in section 2.6.1.1.

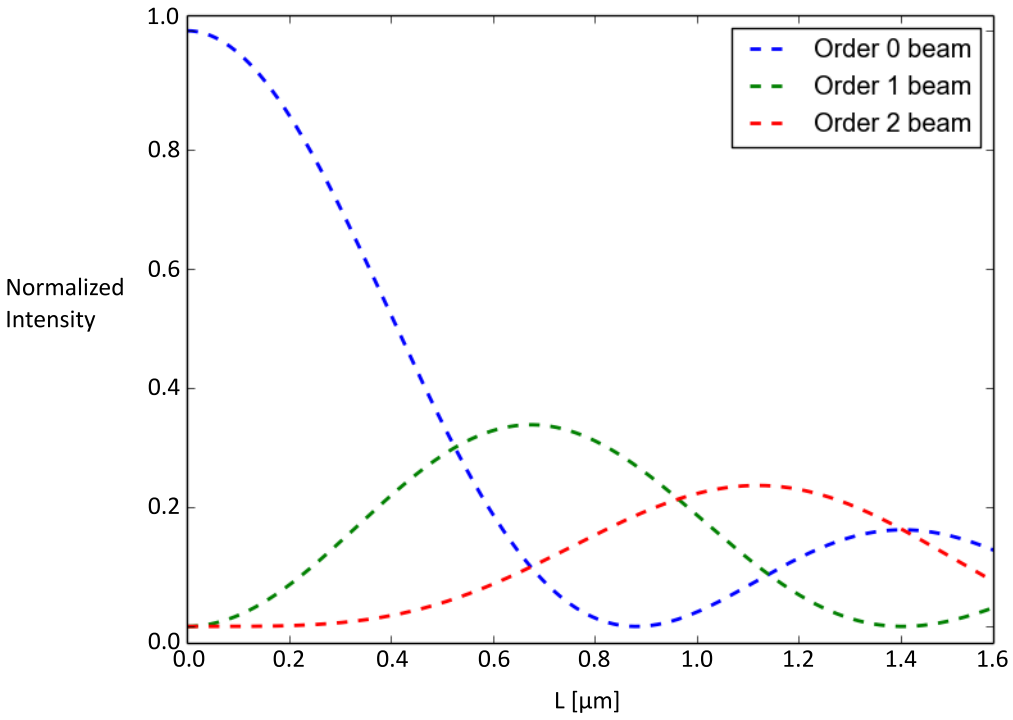

Figure 6.12: Theoretical plots of the intensity of diffracted orders in the Raman-Nath regime.

This may be evidence for the hypothesis that PAAD on the opposite side of the cell to PVK:C_{60} increases the modulation depth of the grating. However, this is an effect that one would also expect to see in the results for PVK and JTDA16 based cells, as the modulation depth is going to be affected by voltage. Instead the diffraction efficiency in these cases decays to 0, a behaviour predicted by Daly *et al* [94]. Clearly, there is currently insufficient data to explain this behaviour fully.

It can be concluded that PAAD has some significant effect, not only on the peak diffraction efficiency, which increases by a factor of 1.8, but also on the voltage dependence of the diffraction efficiency. This is clear evidence that the PAAD is acting to increase the diffraction efficiency due to the PVK:C_{60} layer, and also that the PVK:C_{60} layer is acting to induce photorefractivity in the cell, as the diffraction efficiency would decrease as a function of voltage for a PAAD-PI cell.

The second conclusion relates to the seeming degradation of the photorefractive effect as the experiment goes on. The diffraction efficiency drops significantly between the experiments. This effect is either due to continued exposure to light, continued exposure to an E-field (the cells were shorted between the experiment), or to some other unwanted effect such as cell heating.

The main problem with exposing PAAD with a 30 μm spaced interference pattern for a 30 minute period is the possibility that the pattern will wander due to minute variations in the cell positioning. This may be due to small vibrations in the lab equipment or table. The optics were well secured to a heavy-duty optical bench, but nevertheless, micron-scale movements are possible. It would be interesting to repeat the experiments with a vibration-damped optical bench in order to reduce the vibrations further, and prevent any smearing of the diffraction grating, moving it away from the ideal sinusoidal grating discussed in chapter 2.

The prolonged E-field exposure has long been a problem in polymer-based LCLVs due to the presence of ionic layers at the boundaries of the cell, which potentially become chemically absorbed onto the surfaces. The effect this has on PAAD is unknown, although it should be noted that in the case of PVK, the effect tends to manifest over the course of months, rather than during the first three experiments, and therefore it is not likely to account for the drop in diffraction efficiency over time. However, it would be prudent to set up an experiment where a high field is applied for an extended period, and the cell exposed periodically to check the diffraction efficiency as time goes on.

Finally, the Frederiks transition is much lower in this case, particularly given that the cell is being driven by a DC field. It is known that the Frederiks transition is a material property, and therefore there have to be some assumptions that are incorrectly applied to the PAAD systems.

The change in refractive index in this geometry for PI-PVK cells is due to an in-plane rotation rather than the usual planar-to-homeotropic scheme in non-photoactive cells. Similarly, the PAAD will change the orientation in-plane depending on illumination conditions. Therefore, it is entirely possible that what is being seen in this case is extremely different from a normal Frederiks transition, suggesting that the reorientation

due to the PAAD is a.) occurring at very low fields, and is due mainly to the light illumination, and b.) is propagating through the cell towards the PVK layer (the PVK layer must be playing a role, as there is some transition due to the voltage). This is the clearest evidence possible that PAAD offers some interesting and exceptionally useful effects when combined with PVK, opening the door to highly efficient, scalable, voltage controlled LCLVs. PAAD based polymers in conjunction with JTDA16, or PEDOT/PVK:C_{60} will be the next systems investigated, and may well result in a new range of LCLVs with a heretofore unimagined photorefractive response.

One aspect of all of these devices, which has not been discussed here, is how well the photorefractive behaviour lasts over time. In PI/PVK:C_{60} systems, it has been observed that TBC efficiency goes down if measured 6 months or 1 year after the cells were fabricated. Repeat experiments need to be performed on each of these cells in order to asertain the long-term quality of the devices.

This chapter has outlined the fabrication process and preliminary characterization work for novel LCLV systems. In each case, it has been shown that the systems exhibit a significantly stronger photorefractive response than existing PVK:C_{60} based LCLVs. Future work for this, and other work discussed in this thesis will be outlined in the following chapter 7.

Chapter 7

Conclusions and future work

This thesis has described the development of novel LC characterization techniques and new hybrid nematic systems. The aim of this chapter is to summarize the conclusions from each chapter, and the possible future direction for each piece of work.

7.1 Conclusions from the development of a new, all-optical time response measurement

Chapter 3 described the development of an optical measurement of nematic viscosities and elastic constants. The resultant parameters can be used to calculate the time response of any LC material, which is an essential parameter when designing LC devices. In addition, this is the first experimental and theoretical study of fast oscillations observed when an AC field is applied to an LC device.

The measured values for the rotational viscosity γ_1 were found to be in good agreement, especially given the highly temperature dependent nature of this parameter. For ZLI4792 where the theoretical fit matched most closely with the experimental data, the deviation was only 14.6 mPa s from a literature value of 95.0 mPa s. The deviation from the literature values in E7 and TL205 were somewhat higher (77.2 and 64.0 mPa s respectively), which indicates that there is some difference between measuring the time constant in this way, and measuring it using a mechanical method. This difference

could be down to differences between the batches of LC used, or be due to differences in ambient temperatures. In any case, the extremely good agreement between theory and experiment implies strongly that this technique is a reliable measure of the time response.

7.1.1 Future work for time response measurement

One clear deviation between experimental and theoretical data is seen when modelling the average of the intensity signal as a function of applied voltage amplitude - the CPI experiment. In the case of E7, the data started to deviate significantly for voltages > 10 V, and similar trends have been seen for TL205 cells. While this fit is not used to directly measure γ_1, errors in the obtained values for cell thickness, $K_{1,3}$ and pre-tilt could propogate to indirectly affect the measurements. So far, there has been no theoretical candidate proposed to explain this deviation, and future work must focus on solving this problem.

The time response measurement can be automated and performed in addition to a standard CPI experiment. The eventual aim is to incorporate this technique into a multi-parameter-measurement system, that can provide values for the elastic constants, Frederiks transition, pre-tilt and time response, as well as values for $\alpha_4 + \alpha_5$ for any nematic material. The analysis can also be extended to measuring different LC geometries such as twisted, homeotropic and hybrid aligned systems, which should allow measurements of new linear combinations of the Leslie coefficients.

7.2 Conclusions from the measurements of VTF and AC TBC

Chapter 4 describes two new multi-spectrum techniques for the characterization of LC systems. The first, the so-called VTF, is designed to measure the share of the voltage that is dropped across the LC layer with respect to the other layers. While it was shown that a model of the response was accurate enough to correctly predict the relative electrical conductivities of two LC materials, as well as the relative response time, the technique

is most useful for determining how the electro-optic response of the cell changes under varying ambient conditions. In this thesis, photorefractive cells were measured under differing light conditions, and the results proved that E7 would be a more effective host for transferring a modulation of the conductivity in PVK into the voltage modulation in the LC layer, and hence proved that photorefractive E7 cells would have a higher photorefractive gain than equivalent TL205 cells - a result that was confirmed later in the chapter. Furthermore, the technique could be applied to any LC system where the electrical characteristics of the substituent layers were dependent on some external stimulus, e.g. electrically commanded, or thermoelectric aligning layers.

The multi-spectrum analysis of two-beam coupling in photorefractive LC systems was a continuation of work that showed an increase in beam coupling efficiency when using AC fields to address the cells [72]. The aim was to investigate the cause of this increase in beam coupling efficiency, and also to find out the optimal conditions for high beam coupling gain.

It was discovered that the beam coupling behaviour is affected by the non-ohmic behaviour of PVK:C_{60}, where the condcutivity is in some way dependent on the magnitude of the electric field applied to it [97]. Furthermore, the magnitude of the beam coupling effect was shown to depend highly on the relative conductivity between the photoconducting and LC layers. The voltage frequency and amplitude at which the highest beam coupling takes place was found for TL205 and E7 cells.

7.2.1 Future work for VTF and AC TBC

The VTF is a very powerful technique for assessing how the electro-optic response of an LC cell changes with changing ambient conditions. Therefore, future work will focus on increasing the reliability of the measurment by identifying and eliminating noise and transient effects. After that, the technique can be incorporated into studies of a wide range of novel LC systems where the aligning layers are addressed by some other variable. It would make sense to incorporate the technique along with the time response measurement as discussed in section 7.1.1. A more accurate model should

also be developed that accounts for the build up of screening charge layers at lower frequencies.

The two-beam coupling measurement can verify that a photoconductor is conducting ohmically, and will be used to measure this behaviour when chosing photoconductors that are not PVK-based. Furthermore, it can be used to find the optimum addressing field for TBC response, which is extremely important when developing LCLVs for use in industrial applications.

7.3 Conclusions on LC/multiferroic nanoparticle colloids

There were two main conclusions from the study of multiferroic nanoparticles in LC systems in chapter 5. Firstly, it was shown conclusively that stable suspensions of core-shell multiferroic nanoparticles could be achieved in E7 and ZLI4792 by using ~ 40 nm particles coated with OBPh. The resulting suspensions exhibit low-field magneto-optic switching at fields of ~ 500 G. Secondly, it was also shown that the nanoparticles used did not exhibit a ferroelectric response, which was verified by attempting to harvest the nanoparticles in solution. This is further confirmation that ferroelectricity in nanoparticles below 40 nm in diameter cannot be ferroelectric without some surface stressing due to the milling process.

7.3.1 Future work on LC/multiferroic nanoparticle colloids

The prospect of remote magnetic switching of LC devices is still extremely exciting, and nanoparticle colloids are a good candidate for achieveing this. In this project, stable suspensions of up to 0.2% concentration by mass were achieved, and the reslting magneto-optic behaviour shows that these nanoparticles can strongly affect magnetic switching in LCs. Therefore, future work would concentrate on achieveing still higher concentrations by tuning the size of the nanoparticles as well as the makeup of the surfactant coating.

The fact that ferroelectricity was not observed in these colloids is not especially concerning. The origin of the lack of ferroelectricity was almost certainly the sol-gel growing technique. Future work investigating these colloids must focus on new batches of nanoparticles of the same structure, but including a milling step to try to stress the surface of the nanoparticles, inducing ferroelectric behaviour. For future projects, the ferroelectric effect of the nanoparticles would be confirmed using a harvesting technique prior to dissolving the nanoparticles in LCs.

7.4 Conclusions from the characterization of new LCLV systems

Three new systems were investigated in chapter 6, all of which were designed to improve the photorefractive response in LCLVs that used PVK:C_{60} as a photoconductor. The first such system used a layer of PEDOT, a transparent, polymeric conductor, too reduce the injection barrier that limits photoconductivity in ITO-PVK structures. The attempt was successful - a factor of 3 increase in diffraction efficiency from a benchmark PVK cell was observed. The second system used a photorefractive polymer, JTDA16, in place of PVK:C_{60}, and the spin-coating process was optimised for diffraction efficiency by testing different concentrations of solution. Again, a significantly higher diffraction efficiency was observed in this system when compared to PVK:C_{60} systems - the diffraction efficincy was ~ 11 times higher for the optimised JTDA16 layer. The third system aimed to use a layer of photoaligning PAAD to increase the modulation depth of the grating induced by a PVK:C_{60} layer. The diffraction efficiency was twice as high as for PI-PVK:C_{60} cells, and the behaviour of the diffraction efficiency as a function of voltage was observed to be similar to that of the theoretical response of the diffraction efficiency as a function of modulation depth in the Raman-Nath regime.

7.4.1 Future work for new LCLV systems

The work in chapter 6 is all very promising, and seems to offer significant advantages over existing systems in LCLVs. Future work will focus on a more complete characterization

on these LCLVs, in particular, measurements of the wavelength sensitivity and resolution will be performed. PATPD would need to be tested to compare to JTDA16, to determine the effect (if any) of the non-linear chromophores included in JTDA16, and different layer thicknesses of PVK coated on PEDOT could be investigated, as Khalifa *et al.* showed that the I-V characteristics of this kind of system change significantly with PVK layer thickness [171]. Further tests using PAAD based systems, such as an investigation of PAAD-PI cells would be necessary to work out how to model these systems, and what effect the seperate layers have on the photorefractive response.

7.5 Final conclusions

This thesis has described the development of several new, powerful characterization techniques for use on a wide variety of LC devices. In addition, novel materials have been studied in hybrid nematic devices, which have exhibited massive improvements from existing systems, and should pave the way to numerous industrial applications. There is a lot more work that needs to be done developing and measuring these devices, but I have shown that this work is worthwhile and necessary in order to establish a new, interesting and useful range of LC technologies.

Appendices

Appendix A

Error analysis techniques

This appendix aims to describe the origin of the errors quoted in the main thesis. The sections will appear in the order that they are referenced in the main text.

A.1 Propogation of errors

One concept that needs to be introduced before proceeding is how errors can be calculated for parameters which are dependent on other measured values with their own unique error values. The full treatment of how these errors propogate into an error value for the final measured value is discussed by Ku [193], but the simplified result is given here:

$$s_f = \sqrt{\left(\frac{\partial f}{\partial x}\right)^2 s_x^2 + \left(\frac{\partial f}{\partial y}\right)^2 s_y^2 + \left(\frac{\partial f}{\partial z}\right)^2 s_z^2 + \ldots .} \tag{A.1}$$

This equation is used to calculated the error s_f in a variable given by a function f. f is a function of $(x, y, z, \ldots)$, which are independent variables, each with a corresponding error value s_i. In this way, it is possible to calculate the error in a value that is calculated using multiple independent experimental values, each with its own error value.

A.2 Errors when measuring the thickness of LC cells

Using an etalon effect to measure the thickness of an empty LC cell using a spectrometer is a common technique, described in section 2.1. The possible sources of error include random errors in the measurement itself, errors in resolution when recording the position of the ten peaks, and systematic errors due to the structure of the cell.

The random errors in the measurement are extremely low. This is confirmed by taking 100 shots of the spectrum of the light leaving the cell, and calculating the standard deviation of a series of measurements of the frequency seperation between ten peaks in the spectra. The standard deviation can be used as a standard error, and is given by:

$$\sigma = \sqrt{\frac{\Sigma(x_i - \bar{x})^2}{N-1}} \tag{A.2}$$

where x_i is any single measurement of a parameter (frequency seperation of ten peaks in this case), $\bar{x}$ is the average of this parameter, and N is the number of readings used to calculate $\bar{x}$. For an average seperation of 1.22×10^{14} Hz (which corresponds to a cell of thickness 12 μm), σ was calculated to be 10^10 Hz, a percentage error of 0.01%.

It is valid to assume that this standard deviation is constant, and due to noise errors in the spectrometer. Therefore, the percentage error will be higher as the thickness of the cell increases. However, even for a 50 μm cell, the thickest cell used in this thesis, the error in the frequency seperation is still small (0.3%). This propogates through to an error in the thickness of 2 nm for a 12 μm cell, an error calculated using formulae outlined by Ku [193] as discussed in section A.1.

There is a much higher error contribution based on where across the cell any subsequent measurements take place. This is because the cell thickness is not uniform, and can vary with position. This variability can affect the thickness of the cell when it is used as a parameter in other measurements, e.g. the thickness of the cell is used to calculate the birefringence Δn as described in section 2.4.

To measure the non-uniformity of the thickness, a CPI experiment was performed for a typical cell filled with E7. The cell was then translated, and another CPI experiment

performed. In this way, a CPI plot could be generated at different points across the cell. Given that the birefringence of E7 is well known (Demus *et al.* give it as 0.1917 [194]), the thickness at each of these points can be calculated by measuring the phase shift of the light at zero volts using the method described in section 2.4.1. The resultant thickness profile is shown in figure A.1.

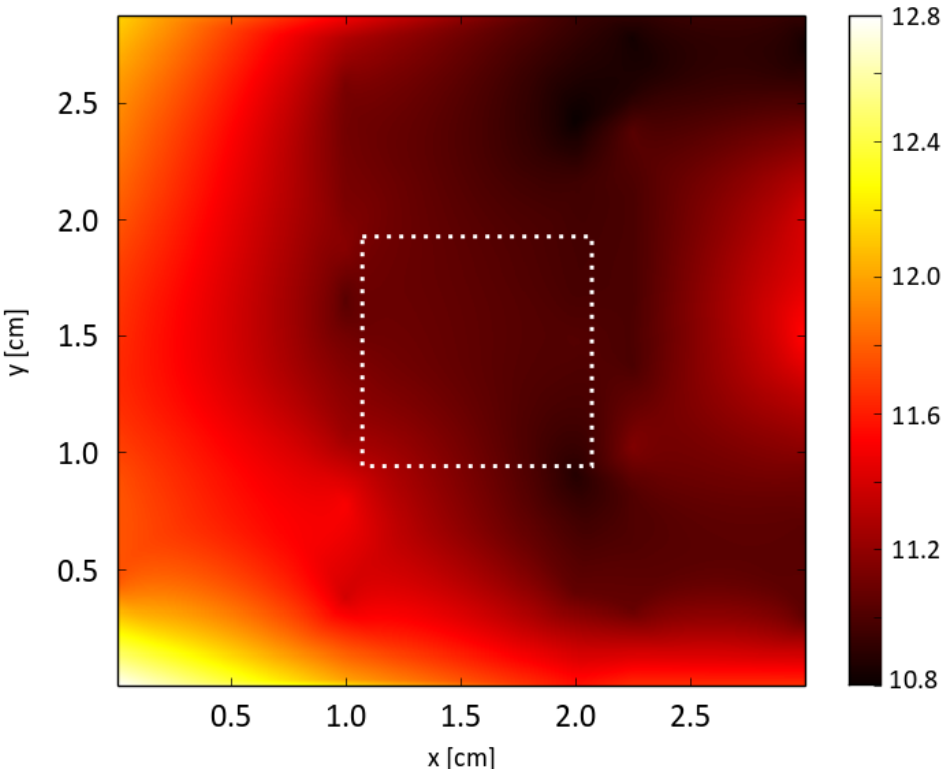

Figure A.1: A color map, which shows the thickness of an LC cell at different positions in the cell. x and y refer to the two length scales of the cell, and the colorbar shows the cell thickness in microns. A 1 cm box is drawn to indicate the estimated variations in the thickness of the cell due to laser beam placement.

The non-uniformity of the cell thickness will contribute to the error when using the thickness as a parameter for calculating Δn e.g. This error can be quantified by estimating how far the laser beam can resonably be expected to deviate from the position where the thickness was first measured. In practice, the laser beam could be as far as 1 cm away from the postition where the thickness was measured, which would result in a thickness variation of 0.4 μm for the cell shown in figure A.1. This error is much larger than the error in the measurement itself, and therefore 0.4 μm is the error in the thickness used in the text.

A.3 Errors in the measurement of the clearing temperature in nematic LCs

The measurement of the transition temperature between the nematic and liquid states is described in section 2.2. However, the only technique used in this thesis (to measure the clearing temperature of colloidal systems described in chapter 5) was heating a sample while observing it under a polarizing microscope. Therefore, this is the only experiment that requires a measurement of the error.

There is a precision error associated with the measurement of the temperature, which is 0.05°C: half of the smallest division. However, this is small when compared to the error in determining the transition temperature itself. When observing an LC as it is heated, a dark area will correspond to an isotropic liquid, while a light-colored area will indicate a nematic liquid crystal. The problem is that there is no defined temperature at which a material is observed to switch between a light and a dark state; one tends to observe small areas or bubbles which are dark, while the majority of the material remains light.

Section 5.4.4 describes how I have approached this problem when measuring the transition temperature of multiferroic nanoparticle colloids. The transition temperature was measured by recording the temperature at which 80% of the observed sample had turned dark, indicating an isotropic liquid phase.

The error in this measurement can be taken as the error in estimating the point at which 80% of the sample had changed to black. The experiment was repeated five times for a single sample, and the temperature at which 80% of the sample had turned dark was recorded in each case. The range of these measurements was found to be 0.5°C either side of the mean value, and this was taken as the error value for each subsequent measurement.

A.4 Errors when measuring the dielectric anisotropy

The errors inherent in the measurement of the capacitance of empty and filled LC cells will propogate through to an error in the calculated value of the dielectric constants.

Therefore, it is the error in the capacitance measurement which will be considered here, and then the effect this has on the measurement of the dielectric constant will be calculated.

A.4.1 Frequency dependence of dielectric constants

One source of error that can effect the dielectric constants of any material directly is the frequency of the field applied to the material. The dielectric constant of a material is a consequence of the electric-field-induced seperation of bound charges (polarization) within the material [101]. Under an AC field, this polarization will flip depending on the sign of the field. However, it takes a finite amount of time for the polarization of the molecules to fully respond to the field, and the polarizability (and hence the dielectric constants of the material) can therefore decrease at higher frequencies, where the charges in the material cannot fully respond to the magnitude of the field.

In the case of LCs, the frequency at which the polarization begins to fall is significantly higher than the AC frequencies used in this thesis. As an example of this, Tomylko *et al.* observe no change in the real dielectric constant of E7 until a voltage with frequency 10^5 Hz is applied to the cell [82]. Therefore, it is valid to assume that the dielectric constants, and hence the capacitances, of the measured cells is independent of the frequency of the field used to probe them.

A.4.2 Experimental errors when measuring the capacitance

The random experimental errors in the measurement of the capacitance can be taken as half of the smallest division of the measurement instrument. This gives an error of ± 0.05 pC. The dielectric constant is given by:

$$\epsilon = \frac{C_{\text{filled}}}{C_{\text{empty}}} \tag{A.3}$$

where the subscripts empty and filled refer to the capacitance of the empty and filled cell respectively. There is an error of ± 0.05 pF in each value for the capacitance, and the propgation of these errors can be found using equation A.1. Using $f(C_{\text{filled}}, C_{\text{empty}}) = \epsilon$

gives an error in the dielectric constant (s_f) of:

$$s_f = \sqrt{\frac{s_x^2}{C_{\text{empty}}} + \frac{C_{\text{filled}}^2}{C_{\text{empty}}^4} s_y^2} \tag{A.4}$$

where $s_{x,y}$ are the errors in the filled capacitance and the empty capacitance respectively (0.05 pF in each case). This equation can be used to calculate the error in the measurements of the dielectric constants.

A.4.3 Experimental errors when fitting to the crossed polarised intensity

Crossed polarised intensity measurements feature heavily in this thesis, and are used to measure Frederiks transition, K_1 and K_3, Δn or thickness. Fitting to the crossed polarised intensity can be done by comparing the experimental data (intensity as a function of applied voltage) to the theoretical data, which can be found by solving equation 1.16 found in the first chapter of this thesis for a given electric field profile (which is calculated from the applied voltage). The director field can then be used to calculate the resultant intensity using equations 1.22, 1.23 and 2.10, and the intensity value is then compared to the experimental value, and the values for the elastic constants can be modified to find the best agreement between theory and experiment.

The theoretical fits and error analysis were perfermoed by Tom Bennett, from the Mathematics department at the University of Southampton. A brief overview of how the errors are calculated is given here, but it should be noted that this work was not performed by the author.

A.4.3.1 The Fisher information

The Fisher information is a method used to determine the amount of information that a measured constant can give you about an unknown parameter, taken from a distribution that is used to model the measured constant [195]. It can be applied to the CPI data by first defining a square distance function that gives the total of how much the theoretical values of the intensity differ from the measured values. The problem becomes finding

values for K_1 and K_3 which minimise this function. The function is rewritten as a normal probability distribution, where it is assumed that the random error on the measurement follows a normal distribution. The Fisher information can then be used to calculate error bars based on the width of this distribution.

This procedure gives an error value based on the goodness of the fit and how well constrained the fitted values are. However, generally it will underestimate the errors if applied to a single data set (this accounts for the particularly low value for the error of γ_1 in the E7 cell, as shown in table 3.1). Future measurements will require multiple repeats in order to more reliably measure the error.

A.5 Errors in measurements of the apparent Fredericks transition

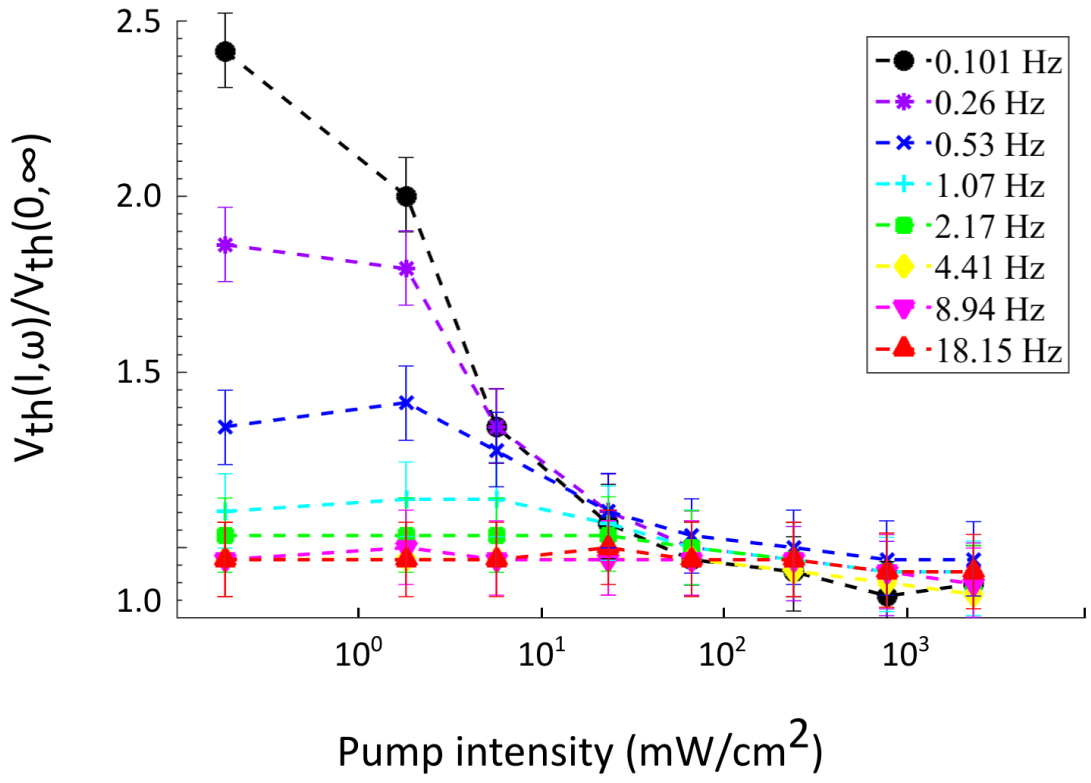

Figure A.2: A reproduction of figure 4.7 for reference.

The apparent Frederiks transition is described in section 4.4 as being an approximate measure of the applied voltage at which the cell undergoes a Frederiks transtion. It

can be determined by finding the point at which the intensity measured in the VTF experiment reaches a value of at least 5% of the maximum intensity signal obtained in the experiment. Figure 4.7 (added as figure A.2 for reference) plots values for the apparent transition (scaled by the same value at high frequency) as a function of light intensity for different applied voltage frequencies.

In order to find an error for these data, it is possible to look at the high-intensity values of the apparent Frederiks transition. When high intensity light is incident on a PVK layer, it should be possible to treat the layer as conductive, and hence low impedance, regardless of the frequency of the voltage applied to the cell. Theoretically, all of the apparent transitions at the high intensity end of figure 4.7 should therefore be identical. This is not the case, and therefore the spread of the values for effective Frederiks transition can be used as an error value for each point.

Appendix B

Modelling the TBC response

This appendix outlines a model used to predict the behaviour of two-beam coupling in a photorefractive cell under application of an AC voltage. The model was developed by Dr Giampaolo D'Alessandro of the School of Mathematics at the University of Southampton.

A modulation transfer function (MTF) is defined in order to characterize the modulated voltage transferred from the PVK:C_{60} layer to the LC layer. A higher value for the MTF will lead to a larger refractive index modulation, and hence a higher value for TBC gain. The mathematical form of the MTF is:

$$\Phi = \frac{\sigma_{\mathrm{PVK}}}{\Delta\sigma_{\mathrm{PVK}}}\frac{\Delta V_{\mathrm{LC}}}{V_0}, \tag{B.1}$$

where $\sigma_{\mathrm{PVK}}/\Delta\sigma_{\mathrm{PVK}}$ is the percentage modulation of the PVK:C_{60} conductivity, V_0 is the voltage applied to the cell, and ΔV_{LC} is the modulated voltage at the PVK:C_{60}/LC interface. Φ can be thought of as how efficiently a modulation of the PVK:C_{60} conductivity can induce a voltage modulation at the interface. The MTF could in theory be obtained from the VTF were it accurate enough to measure the conductivity of the layers under different illuminations, but as the technique is not currently accurate enough to determine the conductivities, it can instead be estimated from an electrical model of the cell.

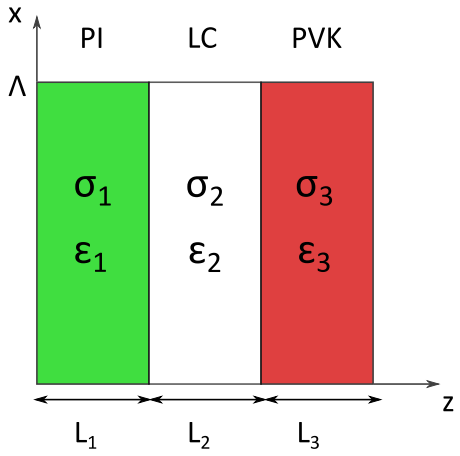

Figure B.1: The system under consideration when modelling the response of photorefractive LC cells.

As stated, it is assumed that a cell is made up of the three layers shown in figure B.1 with conductivity $\tilde{\sigma}_k$ and dielectric permittivity $\tilde{\epsilon}_k$, where $k = 1, 2, 3$ are the indices labelling the PVK:C_{60}, LC and PI layers respectively (this convention is used throughout the following analysis). The $\tilde{.}$ indicates that the quantity in question is dimensional, which is necessary as we will go on to non-dimensionalize the parameters.

These quantities are all constant, except for $\tilde{\sigma}_1$, which is spatially modulated along z with the period Λ, corresponding to the grating spacing of the incident interference pattern. The amplitude of this modulation, $\tilde{\sigma}_{1,1}$ is considered to be a small perturbation. This is valid due to the relatively small beam coupling strengths seen in the TBC experiment, and in any case will give us an understanding of the TBC strength without relying on a complete quantitative description of the system.

In order to find the voltage in the LC layer, we need to solve the following equation:

$$\nabla \cdot \left[(\tilde{\sigma} + i\tilde{\omega}\tilde{\epsilon}) \nabla \tilde{\psi} \right] = 0, \tag{B.2}$$

which is obtained by taking the divergence of Ampère's law, where ψ is the electric potential with a time dependent factor of $e^{i\tilde{\omega}\tilde{t}}$. $\tilde{\omega}$ is the (dimensional) frequency of the applied field.

The non-dimensionalization of equation (B.2) proceeds as follows, with the non-dimensionalized quantities using the same symbols as defined in equation (B.2) but without the superscript $\tilde{.}$. The voltage is scaled to some reference voltage, $\tilde{\psi}_0$. We assume that the dielectric constant of the LC layer is constant, and use that value ($\tilde{\epsilon}_2$) to scale the values for ϵ_k. The layer thicknesses will appear later, and are given by $\tilde{L}_k$: scaled by the thickness $\tilde{L}$ of the entire cell. $\tilde{L}$ is also used to scale the spatial dimensions z and x as defined in figure B.1.

An expression for the modulated and non-dimensional conductivity of PVK:C_{60} is given below:

$$\sigma_1 = \sigma_{1,0}[1 + \eta\sigma_{1,1}\cos(K_g x)], \tag{B.3}$$

where the conductivities have been scaled by the conductivity of the LC ($\tilde{\sigma}_2$), and $\eta << 1$ is a smallness parameter that can be used to constrain the modulation of the conductivity such that it can be treated as a perturbation. The non-dimensionalization of $\tilde{\sigma}_j$ and $\tilde{\epsilon}_j$ gives a non-dimensional frequency of $\omega = \tilde{\epsilon}_2\tilde{\omega}/\tilde{\sigma}_2$.

The following power series solution is assumed:

$$\psi_j = \psi_{j,0}(z) + \eta\psi_{j,1}(z)\cos(K_g x) + O(\eta^2). \tag{B.4}$$

To the leading order in η, the problem reduces to solving $\psi''_{j,0}$, using the boundary conditions imposed by the voltage having to be continuous at the boundaries [2]. The solutions are:

$$\begin{aligned}
\psi_{1,0} &= V\frac{Z_1(L_1 - z)/L_1 + Z_2 + Z_3}{Z_T}, && 0 \le z \le L_1, \\
\psi_{2,0} &= V\frac{Z_2(L_1 - z)/L_2 + Z_2 + Z_3}{Z_T}, && L_1 \le z \le 1 - L_3, \\
\psi_{3,0} &= V\frac{1 - z}{L_3}\frac{Z_3}{Z_T}, && 1 - L_3 \le z \le 1,
\end{aligned} \tag{B.5}$$

where the impedance $Z_j = L_j(\sigma_j + i\omega\epsilon_j)^{-1}$, and the total impedance is given by $Z_T = Z_1 + Z_2 + Z_3$. Expanding these to the first order in η yields:

$$\frac{d^2}{dz^2}\psi_{j,1} - K_g^2\psi_{j,1} = 0, j = 1, 2, 3. \tag{B.6}$$

Meanwhile, the order one solution of equation (B.4) is:

$$\begin{aligned}
\psi_{1,1} &= A_1 e^{-K_g L_1} \sinh(K_g) z, && 0 \le z \le L_1, \\
\psi_{2,1} &= A_2 e^{-K_g L_2} \sinh[K_g(1 - L_3 - z)] + \\
&\quad B_2 e^{-K_g L_2} \sinh[K_g(z - L_1)], && L_1 \le z \le 1 - L_3, \\
\psi_{3,1} &= A_3 e^{-K_g L_3} \sinh[K_g(1 - z)], && 1 - L_3 \le z \le 1,
\end{aligned} \tag{B.7}$$

where the constants A_j and B_2 can be found by substituting equations (B.7) into the boundary conditions for equation (B.6) which are not reproduced here for brevity (see [2]). The result gives the following form of the modulation transfer function that characterizes this model:

$$\Psi = \frac{A_2}{\sigma_{1,1}} e^{-K_g L_2 \sinh(K_g L_2)}, \tag{B.8}$$

where η has been set equal to 1. A_2 can depend on the voltage applied to the device in order to model the non-Ohmic behaviour of PVK:C_{60}.

Bibliography

[1] J. Bateman, M. Proctor, O. Buchnev, N. Podoliak, G. DAlessandro, and M. Kaczmarek, "Voltage transfer function as an optical method to characterize electrical properties of liquid crystal devices," *Optics letters*, vol. 39, no. 13, pp. 3756–3759, 2014.

[2] M. Proctor, J. Bateman, K. Daly, M. Herrington, O. Buchnev, N. Podoliak, G. D'Alessandro, and M. Kaczmarek, "Light-activated modulation and coupling in integrated polymer-liquid crystal systems," *J. Opt. Soc. Am. B*, vol. 31, pp. 3144–3152, Dec 2014.

[3] R. Larsen, "Flat panels hd," May 2014. Available from: http://www.flatpanelshd.com/news.php?subaction=showfull&id=1400759196.

[4] S. Sato, "Liquid crystal lens cells with variable focal length," *Japanese journal of applied physics*, vol. 18, no. 9, pp. 1679–1684, 1979.

[5] H. Milton, M. Nagaraj, S. Kaur, J. Jones, P. Morgan, and H. Gleeson, "Field-induced refractive index variation in the dark conglomerate phase for polarization-independent switchable liquid crystal lenses," *Applied optics*, vol. 53, no. 31, pp. 7278–7284, 2014.

[6] C. Schuller, F. Klopf, J. P. Reithmaier, M. Kamp, and A. Forchel, "Tunable photonic crystals fabricated in iii-v semiconductor slab waveguides using infiltrated liquid crystals," *Applied Physics Letters*, vol. 82, no. 17, pp. 2767–2769, 2003.

[7] D. Press, "Dstl press release: Now you see it, now you don't," February 2014. Available from: http://www.pressat.co.uk/releases/now-you-see-it-now-you-dont-qioptiq-licenses-dazzle-defeating-technology-from-mod-270156a54eaaff40f5ab18a2d02da426/.

[8] N. Konforti, S.-T. Wu, and E. Marom, "Phase-only modulation with twisted nematic liquid-crystal spatial light modulators," *Opt. Lett.*, vol. 13, pp. 251–253, Mar 1988.

[9] M. Peccianti, A. De Rossi, G. Assanto, A. De Luca, C. Umeton, and I. Khoo, "Electrically assisted self-confinement and waveguiding in planar nematic liquid crystal cells," *Applied physics letters*, vol. 77, pp. 7–9, JUL 3 2000.

[10] E. Priestly, *Introduction to Liquid Crystals*. Springer, 1975.

[11] D. Dunmar and T. Sluckin, *Soap, Science and Flat-Screen TVs: A History of Liquid Crystals*. Oxford University Press, 2010.

[12] F. Reinitzer, "Contributions to the understanding of cholesterol," *Monat. fur Chemie*, vol. 9, pp. 421–441, 1888.

[13] S. Chandrasekhar, "Discotic liquid crystals. a brief review," *Liquid Crystals*, vol. 14, no. 1, pp. 3–14, 1993.

[14] V. Gold, *Compendium of Chemical Terminology*. IUPAC, 1997.

[15] P. Collings and M. Hird, *Introduction to Liquid Crystals Chemistry and Physics*. Taylor and Francis, 1997.

[16] G. Gray, "Synthetic chemistry related to liquid crystals," *Molecular Crystals and Liquid Crystals*, vol. 21, no. 1-2, pp. 161–186, 1973.

[17] G. W. Gray, K. J. Harrison, and J. Nash, "New family of nematic liquid crystals for displays," *Electronics Letters*, vol. 9, no. 6, pp. 130–131, 1973.

[18] M. Abramowitz and I. A. Stegun, *Handbook of mathematical functions: with formulas, graphs, and mathematical tables*. No. 55, Courier Corporation, 1964.

[19] I. Haller, "Thermodynamic and static properties of liquid crystals," *Progress in solid state chemistry*, vol. 10, pp. 103–118, 1975.

[20] H. Wang, T. X. Wu, S. Gauza, J. R. Wu, and S.-T. Wu, "A method to estimate the leslie coefficients of liquid crystals based on MBBA data," *Liquid crystals*, vol. 33, no. 1, pp. 91–98, 2006.

[21] F. C. Frank, "I. Liquid crystals. on the theory of liquid crystals," *Discuss. Faraday Soc.*, vol. 25, pp. 19–28, 1958.

[22] J. Katriel, G. F. Kventsel, G. R. Luckhurst, and T. J. Sluckin, "Free energies in the landau and molecular field approaches," *Liquid Crystals*, vol. 1, no. 4, pp. 337–355, 1986.

[23] R. A. Adams and C. Essex, *Calculus: a complete course*, vol. 4. Addison-Wesley, 1999.

[24] I. Stewart, *The Static and Dynamic Continuum Theory of Liquid Crystals: A Mathematical Introduction*. Liquid Crystals Book Series, CRC Press, 2004.

[25] W. M. Gibbons, P. J. Shannon, S.-T. Sun, and B. J. Swetlin, "Surface-mediated alignment of nematic liquid crystals with polarized laser light," 1991.

[26] D. Flanders, D. Shaver, and H. I. Smith, "Alignment of liquid crystals using sub-micrometer periodicity gratings," *Applied Physics Letters*, vol. 32, no. 10, pp. 597–598, 1978.

[27] J. L. Janning, "Thin film surface orientation for liquid crystals," *Applied Physics Letters*, vol. 21, no. 4, pp. 173–174, 1972.

[28] H. Ikeno, H. Maeda, S. Kuniyasu, D. S. Seo, and S. Kobayashi, "Orientation of liquid crystals on polyimide lb films: Application to nematic and ferroelectric EO devices," *Science & Technology*, p. 43, 1989.

[29] Y. Ouchi, I. Mori, M. Sei, E. Ito, T. Araki, H. Ishii, K. Seki, and K. Kondo, "Polarized XANES studies on the rubbed polyimide for liquid crystal alignment; new applicability to the tribology of the polymer systems," *Physica B: Condensed*

Matter, vol. 208209, no. 0, pp. 407 – 408, 1995. Proceedings of the 8th International Conference on X-ray Absorption Fine Structure.

[30] J. Stöhr and M. Samant, "Liquid crystal alignment by rubbed polymer surfaces: a microscopic bond orientation model," *Journal of Electron Spectroscopy and Related Phenomena*, pp. 189–207, DEC 26 1997.

[31] P. de Gennes and J. Prost, *The Physics of Liquid Crystals*. Clarendon Press, 1993.

[32] G. Barbero, G. Cipparrone, O. G. Martins, P. Pagliusi, and A. M. Figueiredo Neto, "Electrical response of a liquid crystal cell: The role of Debyes layer," *Applied Physics Letters*, vol. 89, no. 13, pp. –, 2006.

[33] H. Yokoyama, "Surface anchoring of nematic liquid crystals," *Molecular crystals and liquid crystals*, vol. 165, no. 1, pp. 265–316, 1988.

[34] M. Born and E. Wolf, *Principles of Optics*. Cambridge University Press, 7th ed., 1999.

[35] I. Khoo, H. Li, and Y. Liang, "Observation of orientational photorefractive effects in nematic liquid crystals," *Optics Letters*, vol. 19, no. 21, pp. 1723–1725, 1994.

[36] A. Buka and W. De Jeu, "Diamagnetism and orientational order of nematic liquid crystals," *Journal de Physique*, vol. 43, no. 2, pp. 361–367, 1982.

[37] N. Podoliak, O. Buchnev, O. Buluy, G. D'Allesandro, M. Kaczmarek, Y. Reznikov, and T. Sluckin, "Macroscopic optical effects in low concentration ferronematics," *Soft Matter*, vol. 7, pp. 4742–4749, 2011.

[38] D. W. Berreman, "Optics in smoothly varying anisotropic planar structures: application to liquid-crystal twist cells," *JOSA*, vol. 63, no. 11, pp. 1374–1380, 1973.

[39] D. V. Schroeder, *An introduction to thermal physics*, vol. 60. Addison Wesley New York, 2000.

[40] X. Lu and J. Hay, "Isothermal crystallization kinetics and melting behaviour of poly(ethylene terephthalate)," *Polymer*, vol. 42, no. 23, pp. 9423 – 9431, 2001.

[41] J. Nehring and A. Saupe, "On the schlieren texture in nematic and smectic liquid crystals," *J. Chem. Soc., Faraday Trans. 2*, vol. 68, pp. 1–15, 1972.

[42] C. T. Imrie, Z. Lu, S. J. Picken, and Z. Yildirim, "Oligomeric rod-disc nematic liquid crystals," *Chem. Commun.*, pp. 1245–1247, 2007.

[43] E. Ouskova, O. Buchnev, V. Reshetnyak, Y. Reznikov, and H. Kresse, "Dielectric relaxation spectroscopy of a nematic liquid crystal doped with ferroelectric sn2p2s6 nanoparticles," *Liquid Crystals*, vol. 30, no. 10, pp. 1235–1239, 2003.

[44] "Loctite technical data sheet," June 2007. Available from: http://www.loctite.co.uk/sea/content_data/93806_NEWCA401EN.pdf.

[45] D. W. Alderman and D. M. Grant, "An efficient decoupler coil design which reduces heating in conductive samples in superconducting spectrometers," *Journal of Magnetic Resonance (1969)*, vol. 36, no. 3, pp. 447–451, 1979.

[46] M. Scalerandi, P. Pagliusi, G. Cipparrone, and G. Barbero, "Influence of the ions on the dynamical response of a nematic cell submitted to a dc voltage," *Phys. Rev. E*, vol. 69, p. 051708, May 2004.

[47] S. Wu, U. Efron, and L. Hess, "Birefringence measurements of liquid crystals," *Appl. Opt.*, vol. 23, pp. 3911 – 3915, 1984.

[48] L. Komitov, B. Helgee, J. Felix, and A. Matharu, "Electrically commanded surfaces for nematic liquid crystal displays," *Appl. Phys. Lett.*, 2005.

[49] P. Aubourg, J. Hugnard, M. Hareng, and R. Mullen, "Liquid crystal light valve using bulk monocrystalline bisio as the photoconductive material," *Appl. Opt.*, vol. 21, no. 20, pp. 3706–3712, 1982.

[50] P. R. Ashley, J. H. Davis, and T. K. Oh, "Liquid crystal spatial light modulator with a transmissive amorphous silicon photoconductor," *Appl. Opt.*, vol. 27, pp. 1797–1802, May 1988.

[51] M. Petrović and M. Belić, "Photorefractive ring resonators with vectorial two-beam coupling: Theory and applications," *Physical Review A*, vol. 52, no. 1, p. 671, 1995.

[52] P. Günter, "Holography, coherent light amplification and optical phase conjugation with photorefractive materials," *Physics Reports*, vol. 93, no. 4, pp. 199–299, 1982.

[53] H. Kogelnik, "Coupled wave theory for thick hologram gratings," *The Bell Sys. Tech. J.*, vol. 48, pp. 2910–2946, 1969.

[54] T. K. Gaylord and M. Moharam, "Thin and thick gratings: terminology clarification," *Applied optics*, vol. 20, no. 19, pp. 3271–3273, 1981.

[55] K. Daly, G. D'Alessandro, and M. Kaczmarek, "Regime independent coupled-wave equations in anisotropic phorotefractive media," *Applied Physics B*, vol. 95, pp. 589–596, 1009.

[56] C. Raman and N. Nagendra Nathe, "The diffraction of light by high frequency sound waves: Part I.," *Proceedings of the Indian Academy of Sciences - Section A*, vol. 2, no. 4, pp. 406–412, 1935.

[57] T. Gaylord and M. Moharam, "Analysis and applications of optical diffraction by gratings," *Proceedings of the IEEE*, vol. 73, no. 5, pp. 894–937, 1985.

[58] K. DALY, *Light matter interactions in liquid crystal cells.* PhD thesis, School of Mathematical Sciences, University of Southampton, 2011.

[59] P. Yeh, *Introduction to photorefractive nonlinear optics*, vol. 14. Wiley-Interscience, 1993.

[60] W. Klein and B. D. Cook, "Unified approach to ultrasonic light diffraction," *Sonics and Ultrasonics, IEEE Transactions on*, vol. 14, no. 3, pp. 123–134, 1967.

[61] N. Mukohzaka, N. Yoshida, H. Toyoda, Y. Kobayashi, and T. Hara, "Diffraction efficiency analysis of a parallel-aligned nematic-liquid-crystal spatial light modulator," *Applied optics*, vol. 33, no. 14, pp. 2804–2811, 1994.

[62] F. Leslie, "Continuum theory of cholesteric liquid crystals," *Molecular Crystals and Liquid Crystals*, vol. 7, no. 1, pp. 407–431, 1969.

[63] M. Miesowicz, "The three coefficients of viscosity of anisotropic liquids," *Nature*, p. 27, July 1946.

[64] T. J. Sluckin, D. A. Dunmur, and H. Stegemeyer, *Crystals that flow: classic papers from the history of liquid crystals*. Taylor and Francis, 2004.

[65] O. Parodi, "Stress tensor for a nematic liquid crystal," *J. Phys. France*, vol. 31, no. 7, pp. 581–584, 1970.

[66] P. Martinoty and S. Candau, "Determination of viscosity coefficients of a nematic liquid crystal using a shear waves reflectance technique," *Mol. Crys. and Liq. Crys.*, vol. 14, pp. 243–271, 1971.

[67] J. Kelly, S. Jamal, and M. Cui, "Simulation of the dynamics of twisted nematic devices including flow," *J. Appl. Phys.*, vol. 86, p. 4091, October 1999.

[68] O. M.A., "Molecular theory of flexoelectric effect in nematic liquid crystals," *Sov. Phys. JET*, vol. 58, pp. 1167 – 1171, 12 1983.

[69] B. I. Outram and S. J. Elston, "Determination of flexoelectric coefficients in nematic liquid crystals using the crystal rotation method," *Liquid Crystals*, vol. 39, no. 2, pp. 149–156, 2012.

[70] A. Buka and N. Éber, *Flexoelectricity in Liquid Crystals: Theory, Experiments and Applications*. World Scientific, 2012.

[71] H. Imura and K. Okano, "Temperature dependence of the viscosity coefficients of liquid crystals," *Japanese journal of applied physics*, vol. 11, no. 10, p. 1440, 1972.

[72] M. Herrington, K. Daly, O. Buchnev, G. D'Alessandro, and M. Kaczmarek, "AC-field-enhanced beam coupling in photorefractive, hybrid liquid crystals," *EPL*, vol. 95, JUL 2011.

[73] L. Song, W.-K. Lee, and X. Wang, "AC electric field assisted photo-induced high efficiency orientational diffractive grating in nematic liquid crystals," *Opt. Express*, vol. 14, pp. 2197–2202, Mar 2006.

[74] I. Khoo, "Optical-DC-field induced space charge fields and photorefractive-like holographic grating formation in nematic liquid crystals," *Molecular Crystals and Liquid Crystals*, vol. 282, no. 1, pp. 53–66, 1996.

[75] I. C. Khoo, "Nonlinear optics of liquid crystalline materials," *Physics Reports*, vol. 471, no. 5, pp. 221–267, 2009.

[76] P. D'Angelo, M. Barra, A. CassineSe, M. G. Maglione, P. Vacca, C. Minarini, and A. Rubino, "Electrical transport properties characterization of PVK (poly N-vinyl carbazole) for electrolumine scent devices applications," *Solid-state Electronics*, vol. 51, pp. 123–129, JAN 2007.

[77] J. Tang, C. Lee, and S. Lee, "Carrier injection barrier at metal-organic contacts: role of electronegativity," in *Proc. Int. Symp. on Super-Functionality Organic Devices, Japan*, pp. 6–10, 2005.

[78] H. Ono and N. Kawatsuki, "Orientational holographic grating observed in liquid crystals sandwiched with photoconductive polymer films," *Applied Physics Letters*, vol. 71, no. 9, 1997.

[79] A. Co., "Arduino," April 2015.

[80] "Charge transport in TNF: PVK and TNF: Polyester films and in liquid, amorphous and crystalline TNF, author=Gill, WD, booktitle=Energy and charge transfer in organic semiconductors, pages=137–141, year=1974, publisher=Springer,"

[81] A. Diefenderfer and B. Holton, *Principles of electronic instrumentation*. Saunders College Publishing, 1994.

[82] S. Tomylko, O. Yaroshchuk, O. Kovalchuk, U. Maschke, and R. Yamaguchi, "Dielectric properties of nematic liquid crystal modified with diamond nanoparticles," *Ukr. J. Phys*, vol. 57, pp. 239–243, 2012.

[83] G. Cook, A. V. Glushchenko, V. Reshetnyak, A. T. Griffith, M. A. Saleh, and D. R. Evans, "Nanoparticle doped organic-inorganic hybridphotorefractives," *Opt. Express*, vol. 16, pp. 4015–4022, Mar 2008.

[84] H. Park, E. P. J. Parrott, F. Fan, M. Lim, H. Han, V. G. Chigrinov, and E. Pickwell-MacPherson, "Evaluating liquid crystal properties for use in terahertz devices," *Opt. Express*, vol. 20, pp. 11899–11905, May 2012.

[85] Merck KGaA, "Technical data sheet for nematic liquid crystals," 2005.

[86] C.-S. Yang, T.-T. Tang, P.-H. Chen, R.-P. Pan, P. Yu, and C.-L. Pan, "Voltage-controlled liquid-crystal terahertz phase shifter with indium-tin-oxide nanowhiskers as transparent electrodes," *Optics letters*, vol. 39, no. 8, pp. 2511–2513, 2014.

[87] L. E. Lyons and F. Gutmann, "Organic semiconductors," tech. rep., DTIC Document, 1967.

[88] Y. Wang, "Photoconductivity of fullerene-doped polymers," *Nature*, vol. 356, pp. 585–587, 1992.

[89] F. Li, Y. Li, Z. Guo, C. Long, F. Bai, and D. Zhu, "Photoconductivity of 1,2-(1',1',2',2'-Tetracyanomethanoxymethano)[60]fullerene-Doped PVK," *J. Appl. Polymer. Science*, vol. 72, pp. 209–213, 1999.

[90] T. K. Däubler, L. Kulikovsky, D. Neher, V. Cimrová, J. C. Hummelen, E. Mecher, R. Bittner, and K. Meerholz, "Photoconductivity and charge-carrier photogeneration in photorefractive polymers," in *Nonlinear Optical Transmission Processes and Organic Photorefractive Materials* (C. M. Lawson and K. Meerholz, eds.), vol. 4462 of *Proc SPIE*, pp. 206–216, 2002.

[91] J. H. Ham, J. H. Jung, H. J. Kim, D. U. Lee, and T. W. Kim, "Electrical properties and operating mechanisms of nonvolatile organic memory devices fabricated utilizing hybrid poly(*N*-vinylcarbazole) and C_{60} composites," *Jap. J. Appl. Phys.*, vol. 47, no. 6, pp. 4988–4991, 2008.

[92] F. C. M. Freire, A. L. Alexe-Ionescu, M. Scalerandi, and G. Barbero, "Voltage decay time of a liquid crystal cell submitted to a large difference of potential," *Appl. Phys. Lett.*, vol. 89, no. 21, p. 214101(3), 2006.

[93] A. L. Alexe-Ionescu, G. Barbero, F. Ciuchi, A. Mazzulla, and N. Scaramuzza, "Surface treatment and bulk density of ions in nematic liquid crystals," *J. Appl. Phys.*, vol. 106, no. 4, p. 044508(5), 2009.

[94] K. Daly, N. Podoliak, O. Buchnev, M. Kaczmarek, and G. D'Alessandro, "Optimal liquid crystal modulation controlled by surface alignment and anchoring strength," *J. Opt. Soc. Am. B*, vol. 29, no. 8, pp. 2166 – 2175, 2012.

[95] V. O. Kubytskyi, V. Y. Reshetnyak, T. J. Sluckin, and S. J. Cox, "Theory of surface-potential-mediated photorefractivelike effects in liquid crystals," *Phys. Rev. E*, vol. 79, no. 1, p. 011703(15), 2009.

[96] R. Sutherland, G. Cook, and D. Evans, "Determination of large nematic pre-tilt in liquid crystal cells with mechanically rubbed photorefractive Ce:SBN windows," vol. 95, pp. 589–596, 1009.

[97] Y.-S. Lai, C.-H. Tu, D.-L. Kwong, and J. Chen, "Charge-transport characteristics in bistable resistive Poly(N-vinylcarbazole) films," *Electron Device Letters, IEEE*, vol. 27, pp. 451–453, June 2006.

[98] F. Brochard and P. de Gennes, "Theory of magnetic suspensions in liquid crystals," *J. de Physique*, vol. 13, pp. 691–708, 1970.

[99] Y. Reznikov, O. Buchnev, O. Tereshchenko, V. Reshetnyak, A. Glushchenko, and J. West, "Ferroelectric nematic suspension," *App. phy. letters*, vol. 82, no. 12, pp. 1917–1919, 2003.

[100] C. Mauguin, "Orientation of liquid crystals by a magnetic field," *Comptes Rendus de l'Academie des Sciences*, vol. 152, pp. 1680–1683, 1911.

[101] R. P. Feynman, *The Feynman Lectures on Physics, Volume 2*, vol. 2. Basic Books, 2013.

[102] S. V. Burylov and Y. L. Raikher, "Macroscopic properties of ferronematics caused by orientational interactions on the particle surfaces. I. extended continuum model," *Molecular Crystals and Liquid Crystals Science and Technology. Section A. Molecular Crystals and Liquid Crystals*, vol. 258, no. 1, pp. 107–122, 1995.

[103] S. V. Burylov and Y. L. Raikher, "Macroscopic properties of ferronematics caused by orientational interactions on the particle surfaces. II. behavior of real ferronematics in external fields," *Molecular Crystals and Liquid Crystals Science and Technology. Section A. Molecular Crystals and Liquid Crystals*, vol. 258, no. 1, pp. 123–141, 1995.

[104] S.-H. Chen and N. M. Amer, "Observation of macroscopic collective behavior and new texture in magnetically doped liquid crystals," *Phys. Rev. Lett.*, vol. 51, pp. 2298–2301, Dec 1983.

[105] M. Kaczmarek, O. Buchnev, and I. Nandhakumar, "Ferroelectric nanoparticles in low refractive index liquid crsytals for strong electro-optic response," *Appl. Phys. Let.*, vol. 92, 2008.

[106] O. Buchnev, A. Dyadyusha, M. Kaczmarek, V. Reshetnyak, and Y. Reznikov, "Enhanced two-beam coupling in colloids of ferroelectric nanoparticles in liquid crystals," *J. Opt. Soc. Am.*, vol. 24, no. 7, pp. 1512–1516, 2007.

[107] J. Croat, "Current status and future outlook for bonded neodymium permanent magnets," *Journal of applied physics*, vol. 81, no. 8, pp. 4804–4809, 1997.

[108] G. Catalan, "Magnetocapacitance without magnetoelectric coupling," *Applied Physics Letters*, vol. 88, no. 10, p. 102902, 2006.

[109] G. Catalan and J. F. Scott, "Physics and applications of bismuth ferrite," *Advanced Materials*, vol. 21, no. 24, pp. 2463–2485, 2009.

[110] U. Shivakumar, J. Mirzaei, X. Feng, A. Sharma, P. Moreira, and T. Hegmann, "Nanoparticles: complex and multifaceted additives for liquid crystals," *Liquid Crystals*, vol. 38, no. 11-12, pp. 1495–1514, 2011.

[111] E. R. Soule, J. Milette, L. Reven, and A. D. Rey, "Phase equilibrium and structure formation in gold nanoparticles-nematic liquid crystal composites: experiments and theory," *Soft Matter*, vol. 8, pp. 2860–2866, 2012.

[112] P. J. Flory, "Thermodynamics of high polymer solutions," *The Journal of chemical physics*, vol. 10, no. 1, pp. 51–61, 1942.

[113] N. F. Carnahan and K. E. Starling, "Equation of state for nonattracting rigid spheres," *The Journal of Chemical Physics*, vol. 51, no. 2, pp. 635–636, 1969.

[114] E. R. Soulé, C. E. Hoppe, J. Borrajo, and R. J. Williams, "Thermodynamic model of liquid- liquid phase equilibrium in solutions of alkanethiol-coated nanoparticles," *Industrial & Engineering Chemistry Research*, vol. 49, no. 15, pp. 7008–7016, 2010.

[115] M. Draper, I. M. Saez, S. J. Cowling, P. Gai, B. Heinrich, B. Donnio, D. Guillon, and J. W. Goodby, "Self-assembly and shape morphology of liquid crystalline gold metamaterials," *Advanced Functional Materials*, vol. 21, no. 7, pp. 1260–1278, 2011.

[116] J. W. Goodby, I. M. Saez, S. J. Cowling, V. Grtz, M. Draper, A. W. Hall, S. Sia, G. Cosquer, S.-E. Lee, and E. P. Raynes, "Transmission and amplification of information and properties in nanostructured liquid crystals," *Angewandte Chemie International Edition*, vol. 47, no. 15, pp. 2754–2787, 2008.

[117] J. Mirzaei, M. Urbanski, H.-S. Kitzerow, and T. Hegmann, "Hydrophobic gold nanoparticles via silane conjugation: chemically and thermally robust nanoparticles as dopants for nematic liquid crystals," *Philosophical Transactions of the Royal Society A: Mathematical,Physical and Engineering Sciences*, vol. 371, no. 1988, 2013.

[118] M. Brust, M. Walker, D. Bethell, D. J. Schiffrin, and R. Whyman, "Synthesis of thiol-derivatised gold nanoparticles in a two-phase liquid-liquid system," *J. Chem. Soc., Chem. Commun.*, pp. 801–802, 1994.

[119] R. Krishnamoorti, "Strategies for dispersing nanoparticles in polymers," *MRS Bulletin*, vol. 32, pp. 341–347, 4 2007.

[120] S. Khatua, P. Manna, W.-S. Chang, A. Tcherniak, E. Friedlander, E. R. Zubarev, and S. Link, "Plasmonic nanoparticles-liquid crystal composites," *The Journal of Physical Chemistry C*, vol. 114, no. 16, pp. 7251–7257, 2009.

[121] V. Corral-Flores, D. Bueno-Baqus, and R. Ziolo, "Synthesis and characterization of novel CoFe2O4BaTiO3 multiferroic coreshell-type nanostructures," *Acta Materialia*, vol. 58, no. 3, pp. 764 – 769, 2010.

[122] I. Kolthoff, "Theory of coprecipitation. the formation and properties of crystalline precipitates," *The Journal of Physical Chemistry*, vol. 36, no. 3, pp. 860–881, 1932.

[123] L. L. Hench and J. K. West, "The sol-gel process," *Chemical Reviews*, vol. 90, no. 1, pp. 33–72, 1990.

[124] N. Podoliak, *Magneto-optic effects in colloids of ferromagnetic nanoparticles in nematic liquid crystals.* PhD thesis, School of Physics and Astronomy, University of Southampton, 2012.

[125] S. V. Burylov and Y. L. Raikher, "Ferronematics: enhanced magneto-optical response of a liquid crystalline system," *Materials Science and Engineering: C*, vol. 2, no. 4, pp. 235 – 241, 1995.

[126] N. Podoliak, O. Buchnev, G. D'Alessandro, M. Kaczmarek, and T. J. Sluckin, "Large effect of a small bias field in liquid-crystal magnetic transitions," *Phys. Rev. E*, vol. 82, p. 030701, Sep 2010.

[127] M. S. Zakerhamidi, S. Shoarinejad, and S. Mohammadpour, "Fe3o4 nanoparticle effect on dielectric and ordering behavior of nematic liquid crystal host," *Journal of Molecular Liquids*, vol. 191, pp. 16–19, 2014.

[128] F. Li, O. Buchnev, C. Cheon, A. Glushchenko, V. Reshetnyak, Y. Reznikov, T. Sluckin, and J. West, "Orientational coupling amplification in ferroelectric nematic colloids," *Phys. Rev. Let.*, vol. 97, 2006.

[129] M. Herrington, *Electrical and optical effects in hybrid liquid crystal cells.* PhD thesis, School of Physics and Astronomy, University of Southampton, 2011.

[130] G. Cook, J. Barnes, S. Basun, D. Evans, R. Ziolo, A. Ponce, V. Y. Reshetnyak, A. Glushchenko, and P. Banerjee, "Harvesting single ferroelectric domain stressed nanoparticles for optical and ferroic applications," *Journal of Applied Physics*, vol. 108, no. 6, pp. 064309–064309, 2010.

[131] G. Arlt, "Twinning in ferroelectric and ferroelastic ceramics: stress relief," *J. Mat. Sci.*, vol. 25, pp. 2655 – 2666, 1990.

[132] A. Rudzki, D. R. Evans, G. Cook, and W. Haase, "Size dependence of harvested batio3 nanoparticles on the electro-optic and dielectric properties of ferroelectric liquid crystal nanocolloids," *Applied optics*, vol. 52, no. 22, pp. E6–E14, 2013.

[133] D. Wei, U. Bortolozzo, J. Huignard, and S. Residori, "Slow and stored light by photo-isomerization induced transparency in dye doped chiral nematics," *Optics express*, vol. 21, no. 17, pp. 19544–19554, 2013.

[134] P. R. Ashley and J. H. Davis, "Amorphous silicon photoconductor in a liquid crystal spatial light modulator," *Appl. Opt.*, vol. 26, pp. 241–246, Jan 1987.

[135] U. Bortolozzo, S. Residori, and J.-P. Huignard, "Transmissive liquid crystal light-valve for near-infrared applications," *Appl. Opt.*, vol. 52, pp. E73–E77, Aug 2013.

[136] G. Cook, C. Finnan, and D. Jones, "High optical gain using counterpropagating beams in iron and terbium-doped photorefractive lithium niobate," *Applied Physics B*, vol. 68, no. 5, pp. 911–916, 1999.

[137] K. Ichimura, "Photoalignment of liquid-crystal systems," *Chem. Rev.*, vol. 100, pp. 1847–1874, April 2000.

[138] A. Acreman, M. Kaczmarek, and G. D'Alessandro, "Gold nanoparticle liquid crystal composites as a tunable nonlinear medium," *Physical Review E*, vol. 90, no. 1, p. 012504, 2014.

[139] H. J. Coufal, G. T. Sincerbox, and D. Psaltis, *Holographic data storage*. Springer-Verlag New York, Inc., 2000.

[140] "1951 usaf test target," Dec 2010. Available from: http://commons.wikimedia.org/wiki/File:1951usaf_test_target.jpg.

[141] U. Bortolozzo, S. Residori, A. Petrosyan, and J. Huignard, "Pattern formation and direct measurement of the spatial resolution in a photorefractive liquid crystal light valve," *Optics Communications*, vol. 263, no. 2, pp. 317 – 321, 2006.

[142] G. dAlessandro and W. Firth, "Hexagonal spatial patterns for a Kerr slice with a feedback mirror," *Physical Review A*, vol. 46, no. 1, p. 537, 1992.

[143] Y. Fainman, E. Klancnik, and S. H. Lee, "Optimal coherent image amplification by two-wave coupling in photorefractive BaTiO3," *Optical Engineering*, vol. 25, no. 2, pp. 252228–252228, 1986.

[144] "Photoconductivity and electron mobility in LiNbO3 co-doped with Cr3+ and MgO, author=Ionita, I and Jaque, F, journal=Optical Materials, volume=10, number=2, pages=171–173, year=1998, publisher=Elsevier,"

[145] J. Scott, L. T. Pautmeier, and L. Schein, "Mean mobilities of charge carriers in disordered media," *Physical Review B*, vol. 46, no. 13, p. 8603, 1992.

[146] J. Mort and D. Pai, *Photoconductivity and related phenomena*. Elsevier Scientific Pub. Co., 1976.

[147] V. Y. Reshetnyak, I. P. Pinkevych, G. Cook, D. R. Evans, and T. J. Sluckin, "Two-beam energy exchange in a hybrid photorefractive inorganic-cholesteric cell," *Molecular Crystals and Liquid Crystals*, vol. 560, no. 1, pp. 8–22, 2012.

[148] U. Bortolozzo, S. Residori, and J. P. Huignard, "Beam coupling in photorefractive liquid crystal light valves," *J. Phys. D: Appl. Phys.*, vol. 41, pp. 1–11, 1008.

[149] E. H. Young Jr and S.-K. Yao, "Design considerations for acousto-optic devices," *Proceedings of the IEEE, volume=69, number=1, pages=54–64, year=1981, publisher=IEEE*.

[150] E. Ouskova, D. Lysenko, S. Ksondzyk, L. Cseh, G. H. Mehl, V. Reshetnyak, and Y. Reznikov, "Strong cubic optical nonlinearity of gold nanoparticles suspension in nematic liquid crystal," *Molecular Crystals and Liquid Crystals*, vol. 545, no. 1, pp. 123/[1347]–132/[1356], 2011.

[151] A. Werner and M. Kunst, "Transient photoconductivity in amorphous silicon," *Phys. Rev. B*, vol. 36, pp. 7567–7571, Nov 1987.

[152] H. Helmut and N. Wilhelm, "Electrophotographic reproduction material," June 1962. US Patent 3,037,861.

[153] W. D. Gill, "Drift mobilities in amorphous charge-transfer complexes of trinitrofluorenone and poly-n-vinylcarbazole," *Journal of Applied Physics*, vol. 43, no. 12, pp. 5033–5040, 1972.

[154] G. Weiser, "Densities of complexed and uncomplexed molecules in amorphous films of trinitrofluorenone and poly-n-vinylcarbazole," *Journal of Applied Physics*, vol. 43, no. 12, pp. 5028–5033, 1972.

[155] M. Yokoyama, S. Shimokihara, A. Matsubara, and H. Mikawa, "Extrinsic carrier photogeneration in poly-N-vinylcarbazole. III. CT fluorescence quenching by an electric field," *The Journal of Chemical Physics*, vol. 76, no. 1, pp. 724–728, 1982.

[156] F. Zhou, C. Jehoulet, and A. J. Bard, "Reduction and electrochemistry of fullerene c60 in liquid ammonia," *Journal of the American Chemical Society*, vol. 114, no. 27, pp. 11004–11006, 1992.

[157] G. Wang, S. Qian, J. Xu, W. Wang, X. Liu, X. Lu, and F. Li, "Enhanced photovoltaic response of PVK/C60 composite films," *Physica B: Condensed Matter*, vol. 279, no. 13, pp. 116 – 119, 2000.

[158] R. Lessmann and I. A. Hümmelgen, "Thin copolymer-cased light-emitting display made with fluorine-foped tin oxide substrates," *Materials Research*, vol. 7, no. 3, pp. 467–471, 2004.

[159] Y. Zhou, J. W. Shim, C. Fuentes-Hernandez, A. Sharma, K. A. Knauer, A. J. Giordano, S. R. Marder, and B. Kippelen, "Direct correlation between work function of indium-tin-oxide electrodes and solar cell performance influenced by ultraviolet irradiation and air exposure," *Physical Chemistry Chemical Physics*, vol. 14, no. 34, pp. 12014–12021, 2012.

[160] L. Berthelot, J. Tardy, M. Garrigues, P. Cremillieu, J. Joseph, and B. Masenelli, "ITO/PVK/Alq/metal LEDs: influence of PVK doping with DCM and of passivation with sputtered si3n4," *Optical Materials*, vol. 12, no. 23, pp. 261 – 266, 1999.

[161] J. C. Bernede, "Organic photovoltaic cells: history, principle and techniques," *Journal of the Chilean Chemical Society*, vol. 53, pp. 1549 – 1564, 09 2008.

[162] I. D. Parker, "Carrier tunneling and device characteristics in polymer light-emitting diodes," *Journal of Applied Physics*, vol. 75, no. 3, pp. 1656–1666, 1994.

[163] W. Brtting, S. Berleb, and A. Mckl, "Space-charge limited conduction with a field and temperature dependent mobility in Alq light-emitting devices," *Synthetic Metals*, vol. 122, no. 1, pp. 99 – 104, 2001. Proceedings of the E-MRS 2000 Spring Meeting, Symposium I.

[164] P. Le Rendu, T. Nguyen, O. Gaudin, and V. Tran, "Electrical properties of phenylene vinylene oligomer thin films," *Synthetic metals*, vol. 76, no. 1, pp. 187–190, 1996.

[165] R. Schlaf, H. Murata, and Z. Kafafi, "Work function measurements on indium tin oxide films," *Journal of Electron Spectroscopy and Related Phenomena*, vol. 120, no. 13, pp. 149 – 154, 2001.

[166] C. Huang, H. Meng, G. Ho, C. Chen, C.-S. Hsu, J. Huang, S. Horng, B. Chen, and L. Chen, "Color-tunable multilayer light-emitting diodes based on conjugated polymers," *Applied physics letters*, vol. 84, no. 7, pp. 1195–1197, 2004.

[167] X. Wang, C. Yu, and J. Wu, "Enhanced photovoltaic properties of solar cell based on ITO/PEDOT:PSS/ZnO:P3HT/Ag by an annealing treatment," *Microelectronics International*, vol. 30, no. 1, pp. 10–13, 2013.

[168] A. Elschner, *PEDOT: principles and applications of an intrinsically conductive polymer*. CRC Press, 2011.

[169] F. Jonas and L. Schrader, "Conductive modifications of polymers with polypyrroles and polythiophenes," *Synthetic Metals*, vol. 41, no. 3, pp. 831–836, 1991.

[170] A. Elschner, S. Kirchmeyer, W. Lovenich, U. Merker, and K. Reuter, *PEDOT: principles and applications of an intrinsically conductive polymer*. CRC Press, 2010.

[171] M. B. Khalifa, D. Vaufrey, A. Bouazizi, J. Tardy, and H. Maaref, "Hole injection and transport in ITO/PEDOT/PVK/Al diodes," *Materials Science and Engineering: C*, vol. 21, no. 12, pp. 277 – 282, 2002. Proceedings of the 3rd Maghreb-Europe Meeting on Materials and their Applications for Devices and Physical, Chemical and Biological Sensors, {MADICA} 2001, Hammamet, Tunisia, 29-30 October 2001.

[172] G. Cook, C. Wyres, M. Deer, and D. Jones, "Hybrid organic-inorganic photorefractives," *Proc. of the SPIE*, vol. 5213, pp. 67–81, December 2003.

[173] K. Buse, "Light-induced charge transport processes in photorefractive crystals I: Models and experimental methods," *Applied Physics B*, vol. 64, no. 3, pp. 273–291, 1997.

[174] R. Bube, *Photoconductivity of solids*. John Wiley & sons, inc., 1960.

[175] P. Gunter and J.-P. Huignard, *Photorefractive materials and their applications 1*. Springer, 2006.

[176] S. Stepanov, "Applications of photorefractive crystals," *Reports on progress in physics*, vol. 57, no. 1, p. 39, 1994.

[177] S. Ducharme, J. C. Scott, R. J. Twieg, and W. E. Moerner, "Observation of the photorefractive effect in a polymer," *Phys. Rev. Lett.*, vol. 66, pp. 1846–1849, 1991.

[178] Y. Zhang, R. Burzynski, S. Ghosal, and M. K. Casstevens, "Photorefractive polymers and composites," *Advanced Materials*, vol. 8, no. 2, pp. 111–125, 1996.

[179] K. Ferrio, J. Herlocker, N. Armstrong, E. Mash, A. Persoons, *et al.*, "Photoconductive properties of pvk-based photorefractive polymer composites doped with fluorinated styrene chromophores," *Journal of Materials Chemistry*, vol. 9, no. 9, pp. 2251–2258, 1999.

[180] W. E. Moerner and S. M. Silence, "Polymeric photorefractive materials," *Chemical Reviews*, vol. 94, no. 1, pp. 127–155, 1994.

[181] J. Thomas, C. Fuentes-Hernandez, M. Yanamoto, K. Cammack, K. Matsumoto, G. Walker, S. Barlow, B. Kippelen, G. Meredith, S. Marder, and N. Peyghambarian, "Bistriarylamine polymer-based composites for photorefractive applications," *Adv. Mater.*, vol. 16, no. 22, pp. 2032–2036, 2004.

[182] L. Yu, W. K. Chan, Z. Peng, and A. Gharavi, "Multifunctional polymers exhibiting photorefractive effects," *Accounts of chemical research*, vol. 29, no. 1, pp. 13–21, 1996.

[183] M. Wahle and H.-S. Kitzerow, "Liquid crystal assisted optical fibres," *Opt. Express*, vol. 22, pp. 262–273, Jan 2014.

[184] K. Ichimura, Y. Suzuki, T. Seki, A. Hosoki, and K. Aoki, "Reversible change in alignment mode of nematic liquid crystals regulated photochemically by command surfaces modified with an azobenzene monolayer," *Langmuir*, vol. 4, no. 5, pp. 1214–1216, 1988.

[185] O. Yaroshchuk and Y. Reznikov, "Photoalignment of liquid crystals: basics and current trends," *Journal of Materials Chemistry*, vol. 22, no. 2, pp. 286–300, 2012.

[186] E. Fischer, "Effect of annealing and temperature on the morphological structure of polymers," *Pure and applied chemistry*, vol. 31, no. 1-2, pp. 113–132, 1972.

[187] Brewerscience, "Spin coating theory," January 1997. Available at: http://www.brewerscience.com/spin-coating-theory.

[188] A. Siegman, *Lasers*. University Science Books, 1986.

[189] A. Yamamori, C. Adachi, T. Koyama, and Y. Taniguchi, "Electroluminescence of organic light emitting diodes with a thick hole transport layer composed of a triphenylamine based polymer doped with an antimonium compound," *Journal of Applied Physics*, vol. 86, no. 8, pp. 4369–4376, 1999.

[190] S. R. Marder, B. Kippelen, A. K.-Y. Jen, and N. Peyghambarian, "Design and synthesis of chromophores and polymers for electro-optic and photorefractive applications," *Nature*, vol. 388, no. 6645, pp. 845–851, 1997.

[191] B. Engineering, "Beam engineering for advanced measurements co. catalog," May 2015. Available from: http://www.beamco.com/uploaded_images/catalog.pdf?t=1303263172.49.

[192] U. of Strasbourg, "Rhin solar," May 2015. Available from: http://www.rhinsolar.eu/.

[193] H. Ku, "Notes on the use of propagation of error formulas," *Journal of Research of the National Bureau of Standards*, vol. 70, no. 4, 1966.

[194] D. Demus, J. Goodby, G. Gray, H. Spiess, and V. Vill, *Physical properties of liquid crystals*. Wiley-Vch Weinheim, Germany, 1999.

[195] B. R. Frieden, *Science from Fisher information: a unification.* Cambridge University Press, 2004.